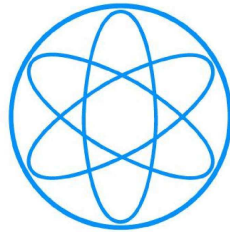


PHYSIK - DEPARTMENT



Dynamics of Water Bearing Silicate Melts as
seen by Quasielastic Neutron Scattering
at High Temperature and Pressure

Dissertation

von

Fan Yang



TECHNISCHE UNIVERSITÄT
MÜNCHEN

Physik-Department der
Technischen Universität München
Lehrstuhl für Experimentalphysik IV

**Dynamics of Water Bearing Silicate Melts as
seen by Quasielastic Neutron Scattering
at High Temperature and Pressure**

Fan Yang

Vollständiger Abdruck der von der Fakultät für Physik der Technischen
Universität München zur Erlangung des akademischen Grades eines
Doktors der Naturwissenschaften (Dr. rer. nat.)
genehmigten Dissertation

Vorsitzender: Univ.-Prof. Dr. R. Metzler

Prüfer der Dissertation:

1. Univ.-Prof. Dr. A. Meyer
2. Univ.-Prof. Chr. Pfeleiderer, Ph. D.

Die Dissertation wurde am 29.01.2009 bei der Technischen Universität
München eingereicht und durch die Fakultät für Physik am 03.04.2009
angenommen.

Dedicated to Qi

Contents

Summary	v
Zusammenfassung	vii
1 Introduction and motivation	1
1.1 Geological importance	1
1.2 The glass transition	2
1.3 Interplay of structure and dynamics in silicate melts	4
1.4 The hydrous silicate system	7
1.5 Present work	9
2 Sample synthesis	11
2.1 Preparation of the dry silicates	11
2.2 Dissolution of water	13
2.2.1 Sample capsules	13
2.2.2 High temperature and pressure process	15
2.3 Sample characterization	19
2.3.1 Calorimetry	19
2.3.2 Dilatometry	20
3 Theoretical background	24
3.1 Neutron scattering	24
3.1.1 Basic theory	24
3.1.2 Coherent/incoherent scattering and correlation functions	27
3.1.3 Neutron scattering on liquids and glasses	29
3.2 Diffusion	33
3.2.1 Diffusion in simple liquid	33
3.2.2 Hopping model and anomalous diffusion	34
3.3 Mode coupling theory and the glass transition	37
3.3.1 Basic approach	37
3.3.2 Structural relaxation processes and scaling laws	38
3.3.3 Schematic models of glass transition in MCT	40

4	Sample environment	42
4.1	Basic concepts	42
4.1.1	High pressure high temperature vessel	42
4.1.2	Materials	45
4.2	Construction and operation of the autoclave	46
4.2.1	High pressure components	47
4.2.2	High temperature furnace	49
4.2.3	Other components and adaption to TOFTOF	51
4.3	Neutron scattering characteristics	55
5	Neutron scattering experiment	59
5.1	Time-of-flight spectroscopy	59
5.2	Experimental setup	63
5.3	Reduction of neutron data	64
5.4	Neutron backscattering spectroscopy	70
6	Dynamics in hydrous silicate melts	73
6.1	Dry sodium trisilicates	73
6.2	Hydrous sodium trisilicate melt	74
6.2.1	Energy domain analysis	75
6.2.2	Time domain analysis	79
6.3	Deuterated sodium trisilicate melt	83
6.4	Backscattering measurement	84
6.5	Other silicate systems	86
7	Outlook	89
7.1	Neutron scattering experiments	89
7.2	Diffusion couple measurements	90
7.2.1	Ex-situ experiments	90
7.2.2	Neutron radiography	91
	Appendix	93
A	Neutron scattering cross sections	93
B	List of neutron scattering experiments	94
	List of figures	97
	List of tables	99
	Acknowledgement	101
	Bibliography	103
	Declaration of authorship	109

Summary

The aims of current thesis are to construct a high temperature high pressure sample environment for neutron time-of-flight experiments and to study water dynamics in hydrous silicate melts under high temperature and high pressure conditions with quasielastic neutron scattering techniques.

The understanding of the relaxation behaviour of silicate melts is very important for many geological processes, especially active volcanism. The addition of water to silicates causes a drastic, non-linear drop of the melt viscosity by 5-10 orders of magnitude. Water is known to partially react with silicates upon its dissolution, which results in two different species to be present in the silicates: OH-groups and molecular water. The knowledge of the water dynamics represents an essential key to understand the melt properties. However, the dissolution and transport mechanisms of water species in silicate melts is still not understood.

Neutron scattering techniques give access to investigate dynamics on microscopic timescales in the order of picoseconds to nanoseconds and on interatomic distances in the Å range. The intrinsic q resolution of the quasielastic neutron scattering allows to study diffusion mechanisms in great detail by analyzing the q dependence of the scattering amplitude and line shape of the quasielastic signal.

Hydrous silicate samples are prepared by fusion of dry silicates with water at high temperature under high pressure with a total water content of 10 mol%. The characterization of sample glass transition temperatures using calorimetric and dilatometric methods show that water is homogeneously dissolved in the silicate glasses.

To study the hydrous silicates at temperatures higher than their glass transition temperatures, high pressure in the order of 1-2 kbars is simultaneously required to suppress water evaporation. Therefore, a high temperature high pressure sample environment was built which is optimized for the neutron time-of-flight spectrometer TOFTOF at FRM II. Nb₁Zr alloy is chosen as the cell material. Nb is a refractory class metal which provides sufficient mechanical strength at elevated temperatures. Nb has also an extremely small incoherent neutron scattering cross section. Hence, an acceptable signal-to-background ratio of about 10:1 can be achieved within the elastic and quasielastic region even with such a massive pressure cell with a 35 mm outer diameter and 12 mm wall thickness. An internal heating setup is used to heat up the samples. This is favorable for high pressure apparatus operated at high temperatures. With such setup the sample environment provides a temperature range from ambient temperature up to 1500 K at pressures up to 2 kbar at the sample position. Samples with a volume of around 1 cm³ can be measured, which meets the intensity requirements for the neutron time-of-flight experiments.

The realization of the high temperature high pressure sample environment opens a new possibility of using quasielastic neutron scattering techniques to study hydrous silicates. This enables direct observations of water dynamics in silicate melts under magma chamber conditions on an absolute scale. Neutron scattering also provides the possibility to perform a contrast variation via $\text{H}_2\text{O}/\text{D}_2\text{O}$ substitution. As a result pure proton signals can be extracted.

In the hydrous $\text{NaAlSi}_3\text{O}_8$ and SiO_2 system, The proton dynamics is not so fast as expected, although the macroscopic glass transition temperature of the samples has already dropped almost by a factor of 2 compared to that of the dry silicates. No resolvable quasielastic broadening or decay of the intermediate scattering function has been observed with the instrumental energy resolutions available on TOFTOF at the highest measured temperature. The lower boundary value of the diffusion coefficients is on the order of $10^{-10} \text{ m}^2\text{s}^{-1}$ in the investigated temperature range.

An unusual relaxation behaviour of the proton in hydrous sodium trisilicate melt has been observed. In the energy domain analysis, the scattering function $S(q, \omega)$ of the pure proton signal shows a clear elastic contribution which cannot be described by a simple Lorentzian or Kohlrausch-Williams-Watts (KWW, Fourier transformed stretched exponential) function. The analysis of the high frequency wing of the spectra indicates an anomalous diffusive behaviour.

In the time domain analysis, the intermediate scattering function $S(q, t)$ exhibits an extreme stretching. Instead of using an unphysical stretching exponent value, the signal is best fitted with a logarithmic like decay to an intermediate non-zero constant value $f^2(q)$ at large time around 20~25 ps. The further decay of this constant value towards zero is out of the accessible time window at TOFTOF. Through a careful analysis of the q and temperature dependence of $f^2(q)$, an attribution of the fast/slow relaxations to different proton environments cannot be satisfied. Within the neutron experiment results no evidence of different dynamics induced by different proton environments due to different water species has been identified.

Logarithmic like decay is a signature of the dynamics in systems which have different competitive arrest mechanisms as expected by mode coupling theory. This has been confirmed to be present in binary hard spheres mixtures with a sufficient large size disparity like sodium trisilicate melt under certain conditions. The observations on hydrous sodium silicate melts have shown qualitatively agreements with such theoretical predictions. The proton dynamics can be understood under a glass-glass transition scenario, where the proton is still able to diffuse in the immobile, glassy Si-O matrix before the complete system is frozen. To verify such interpretation it is necessary to further study the final decay of the intermediate plateau value $f^2(q)$ to zero, which is expected by the mode coupling theory to be a stretched exponential decay.

Zusammenfassung

Ziel der vorliegenden Arbeit war die Entwicklung einer Hochtemperatur Druckzelle, für den Einsatz bei der Neutronen Flugzeitspektrometrie, um die Wasserdynamik in wasserhaltigen Silikatschmelzen unter hohen Temperaturen und Drücken mit quasi-elastischer Neutronenstreuung zu untersuchen. Das Verständniss des Relaxationsverhaltens von Silikatschmelzen spielt bei vielen geologischen Prozessen eine wichtige Rolle, zum Beispiel bei aktiven Vulkanismus. Das Hinzuführen von Wasser zu Silikat verursacht eine dramatische nicht-lineare Verringerung der Viskosität um etwa 5-10 Größenordnungen. Durch Lösung des Wassers in der Silikatschmelze entsteht OH Gruppen und H_2O . Die Untersuchung der Wasserdynamik spielt eine Schlüsselrolle um die Eigenschaften der Schmelze zu verstehen. Der Lösungs- und Transportmechanismus des Wassers in der Silikatschmelze ist noch unverstanden. Mit Neutronenstreuexperimenten ist es möglich mikroskopische Dynamik auf Zeitskalen von Pico- bis Nanosekunden, sowie auf interatomaren Abständen zu untersuchen. Dank der intrinsischen q Auflösung können Diffusionsmechanismen durch Analyse der q Abhängigkeit der Streuamplitude und Linienform untersucht werden.

Wasserhaltige Silikatproben wurden durch Verschmelzen der trockenen Silikate mit Wasser, bei hohen Temperaturen und Drücken mit einem totalen Wassergehalt von 10% mol, hergestellt. Durch Einordnen der entsprechenden Glassüergangstemperatur mittels Kalor- und Dilatometrischen Methoden konnte eine homogene Verteilung des Wassers in der Silikatschmelze nachgewiesen werden.

Um wasserhaltige Silikatschmelzen bei Temperaturen weit über deren Glasübergangstemperatur zu untersuchen, werden Drücke um 1-2 kbar benötigt, um die Wasserverdunstung zu unterdrücken. Um dies zu gewährleisten wurde eine Hochtemperatur Druckzelle konstruiert, die für das Flugzeitspektrometer TOFTOF am FRM II ausgelegt war. Nb ist ein Hochtemperaturwerkstoff der im relevanten Temperaturbereich stabil ist. Der inkohärente Neutronenstreuquerschnitt ist aussergewöhnlich klein. Im elastischen und quasielastischen Bereich kann damit ein Signal zu Untergrundverhältniss von 10:1 erzielt werden, trotz der mit einem Durchmesser von 35mm und 12mm starken Wänden versehenen massiven Druckzelle. Die Proben werden durch eine Innenbeheizung auf Temperatur gebracht, die optimal für einen Hochtemperatur und Druckapparat ist. Mit dieser Hochtemperatur Druckzelle sind Temperaturen bis zu 1500 K und Drücke bis zu 2kbar an der Probenposition möglich. In der Flugzeitspektrometrie können aus Intensitätsgründen Proben bis zu einem Volumen von 1 cm^3 untersucht werden.

Die Umsetzung der Hochtemperatur Druckzelle eröffnet neue Möglichkeiten um wasserhaltige Silikatschmelzen durch quasielastische Neutronenstreuung zu unter-

suchen. Die mikroskopische Wasserdynamik kann unter Bedingungen untersucht werden wie sie in Magmakammern vorherrschen. Durch Kontrastvariation mit D₂O/H₂O kann das Protonsignal erschlossen werden. In wasserhaltigen Albit- und SiO₂-systemen ist die Protonendynamik langsamer als erwartet, obwohl die makroskopische Glasübergangstemperatur der Proben, durch Wasserzugabe um einen Faktor 2 verringert wurde. Keine auflösbare quasielastische Verbreiterung oder ein Zerfall der intermediären Streufunktion wurde bei der höchsten gemessenen Temperatur mit der Energieauflösung des TOFTOF beobachtet. Die untere Grenze des Diffusionskoeffizienten liegt im untersuchten Temperaturbereich in der Größenordnung von $10^{-10} \text{ m}^2\text{s}^{-1}$.

Ein nichttriviales Relaxationsverhalten des Protons in der wasserhaltigen Natriumtrisilikatschmelze wurde beobachtet. Im Energieraum zeigt die Streufunktion $S(q, \omega)$ des Protonsignals einen rein elastischen Beitrag, der nicht mit einer einfachen Lorentz- oder Kohlrausch-Williams-Watt- Funktion beschrieben werden kann.

Im Zeitraum zeigt die intermediäre Streufunktion $S(q, t)$ einen langsameren Abfall. Am besten lässt sich das Signal mit einem logarithmischen Zerfall vergleichen, der bei langen Zeiten um die 20-25 ps auf einen konstanten Wert $f^2(q)$ abfällt. Der weitere Verlauf dieses Plateaus liegt außerhalb des experimentell zugänglichen Zeitskalen. Durch Analyse der q - und Temperaturabhängigkeit kann keine Aussage über die langsame oder schnelle Dynamik in unterschiedlichen Wasserspecies getroffen werden. Durch die Neutronenstreuexperimente konnte kein Beweis für unterschiedliche Dynamik aufgrund unterschiedlicher Protonumgebungen erbracht werden.

Ein logarithmischer Zerfall ist ein Anzeichen für mikroskopische Dynamik die durch gegensätzliche "Cageing"-Mechanismen bestimmt ist, wie man im Rahmen der Modenkopplungstheorie erwarten würde. Dies wurde unter anderem für binäre harte Kugel Systeme mit stark abweichenden Durchmessern bestätigt, wie die Natriumtrisilikatschmelze unter gewissen Bedingungen. Die Beobachtungen an der wasserhaltigen Natriumsilikatschmelze stimmen qualitativ mit diesen theoretischen Vorhersagen überein. Die Protonendynamik kann als ein Glas-Glas-Übergangs Szenario verstanden werden, indem das Proton noch durch die eingefrorene Si-O Matrix diffundiert, bevor auch dieses seine Beweglichkeit verliert. Um diese Interpretation nachzuweisen ist es notwendig den Abfall des Plateaus $f^2(q)$ auf 0 zu untersuchen, der im Rahmen der Modenkopplungstheorie einer gestreckten Exponentialfunktion folgen sollte.

Chapter 1

Introduction and motivation

1.1 Geological importance

Silicon and oxygen are the two most abundant elements which are present in the earth crust and mantle [MA80]. Silicate based minerals are the largest and most important class of rock forming materials. Consequently, their physical and chemical properties, either in the solid or molten state, are highly relevant for geological processes and have drawn enormous research interests.

Explosive volcanism is one example in which the knowledge of the melt properties of the silicates is essential. Explosive volcanic eruption is one of the most spectacular and dangerous geological events. However, not all of the volcanic eruptions are explosive. Effusive eruptions can also occur in which the magma can just flow out from its chamber. Those two different styles can even occur within a single volcanic center. The understanding of the mechanisms, which determine the eruption style, is important for the estimation of the danger in such events [Din96].

It has already been discovered that volatiles in magma are highly relevant to the explosive volcanic eruption. Water is the major component of those volatiles (Others are: CO_2 , H_2S , etc.). In nature, several weight percent of water can be stably dissolved in silicate melts in the magma chamber at a temperature up to 1500 K under a pressure of several kbars. In volcanic eruptions, decompression of such silicate melts during the ascending to the earth surface causes the dissolved water to diffuse from the over-saturated melt into the growing bubbles. This leads to the acceleration of the melt in the magma chamber due to the expansion of the bubbles.

Whether the melt shows a viscous liquid or a glass (solid) like response to such strain rate of deformation determines the eruption style [DW89]. The (structure) relaxation timescale can be estimated according to the simple Maxwell relation of linear

visco-elasticity of shear which links the relaxation time τ_0 with the melt viscosity by

$$\tau_s = \frac{\eta_s}{G_\infty}. \quad (1.1)$$

η_s is the shear viscosity and G_∞ is the shear modulus at infinite frequency. The shear modulus of silicates is in the order of 10 GPa. It can be regarded as fairly constant for different compositions, while the viscosity of their melts varies considerably as a function of composition and temperature by many orders of magnitude. The dissolution of the water into the silicate also leads to a drastic, non-linear drop of the melt viscosity. Thus, being dehydrated during the ascending, the magma viscosity increases significantly. If the strain rate is much higher than the relaxation rate defined by τ_s , the melt cannot relax as a viscous liquid which will result a brittle failure of the mixture: a process called fragmentation. For reviews on this topic see [SMD95]. Therefore, the knowledge of the melt viscosity and dehydration kinetics represent two keys to understand such processes.

It is generally known that water is chemically dissolved and the reaction between water and silicates is connected with the melt properties. Also the transport properties and mechanisms of waters are very important to understand the dehydration kinetics. Many investigations have been performed in the glassy state or using a quenching method to address those questions. However, due to the complex reaction of the water with the silicates upon dissolution, many corrections must be taken into account. Therefore, the dissolution and transport mechanisms of the water species in the melt is still not understood yet.

Direct investigation of the water dynamics in the melt will be a large step further towards the understanding of the system. In order to study hydrous silicate in the melt high pressure in the order of 1-2 kbars is required besides high temperature to prevent water evaporation. Till now only very few investigations have been conducted since to perform experiments under high temperature and high pressure conditions with optical spectroscopy methods and NMR is still quite challenging due to technical reasons.

1.2 The glass transition

When cooling down a liquid below its melting point the thermodynamic equilibrium state is the crystalline phase. However, for kinetic reasons this phase transition can be hindered since nucleation is necessary. The supercooled liquid must cross this energy barrier in order to crystallize. If the cooling rate is fast enough, the molecules or atoms do not have enough mobility to overcome this nucleation barrier and the supercooled

liquid can be frozen in an amorphous state.

For glass forming materials, the critical cooling rate which can prevent crystallization, is in the experimental accessible range. There are a large numbers of different kinds of materials, which belong to the class. This includes small molecules like glycerol, inorganic network formers like silicates and complex macromolecules like polymers.

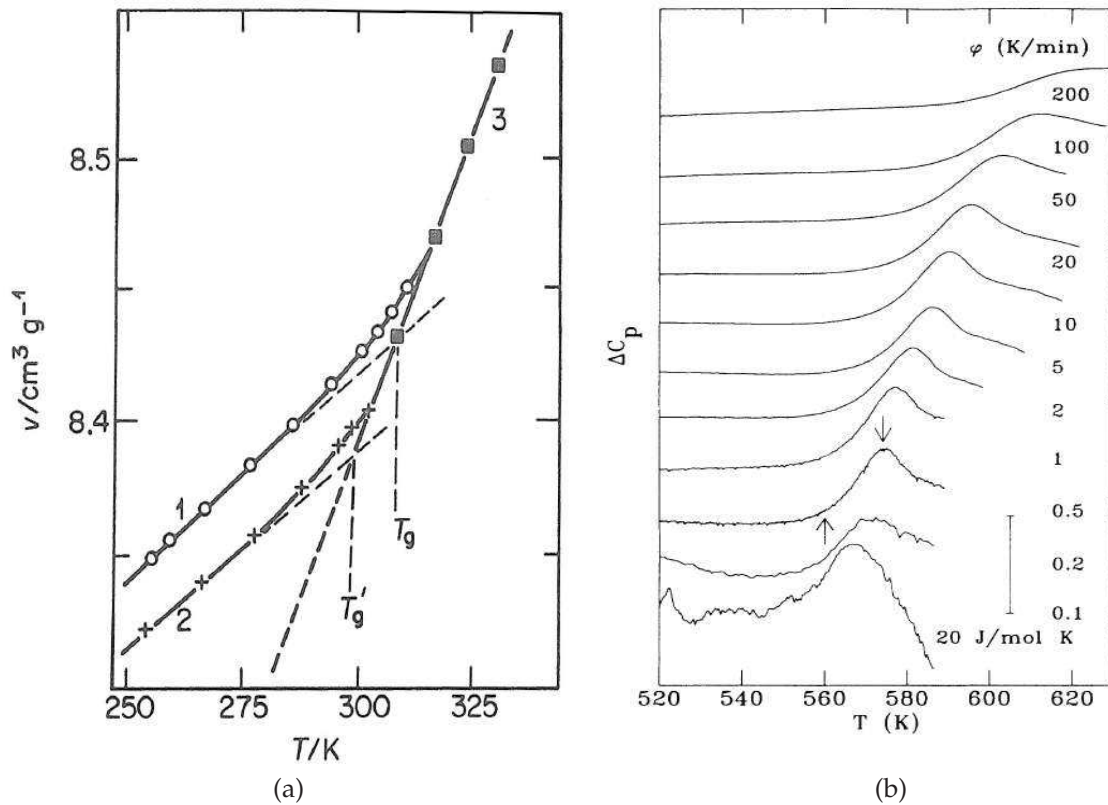


Figure 1.1: Temperature dependence of physical properties of glass forming materials, measured with different observation methods. a) Temperature dependence of molar volume of a polymer. After [Cow01]. b) Temperature dependence of heat capacities of a bulk metallic glass former PdNiPSi [BS92], the arrows indicate where the glass transition temperature can be defined, either at the onset or the peak position of the excess heat capacity. In both cases the defined glass transition temperature varies as a function of heating (cooling) rate.

Glass forming materials are characterized by the glass transition temperature where a transition from the supercooled liquid to the glass happens. Generally it marks the transition from liquid-like behaviour to solid-like behaviour, which is therefore very important as it has been already shown in the last section. The corresponding viscosity at this temperature of the samples is around $10^{12} \text{ Pa}\cdot\text{s}$. Many physical properties of the melt change around this temperature. For example, the temperature dependence of the partial molar volume or heat capacity change their behaviour (Fig.1.1). The viscosity

around the glass transition temperature also increases strongly. Instead of following an Arrhenius law, the temperature dependence is frequently described by the empirical Vogel-Fulcher formula

$$\eta(T) = A \exp(B/(T - T_0)) \quad (1.2)$$

or some other equations, which have stronger temperature dependence than that of the Arrhenius law (for a overview see e.g.: [CLH⁺97]).

However, this transition temperature from a supercooled liquid to a glass is somehow arbitrary defined because it only corresponds to a macroscopic relaxation time in the orders of seconds to minutes (cf. Eqn.1.1): a timescale which is normally accessible in the laboratory. As it has already been shown in Fig.1.1 the measured glass transition temperature depends on the experimental techniques as well as timescales of observation. The T_0 defined in the Vogel-Fulcher equation is not a well defined physical quantity.

Many experiment techniques, particularly dielectric spectroscopy, have shown already that there are different relaxation processes in glass forming materials. In many systems so called α - and β -relaxation processes can be identified. The α -relaxation is well known to be connected with the glass transition since in glasses the atoms or molecules have negligible long range mobility and α -relaxation or structural relaxation is frozen. Thus the temperature at the onset of the α relaxations gives a microscopic definition of the glass transition. Such microscopic approach is described in the framework of mode coupling theory (MCT), which will be introduced in chapter 3 with a critical temperature T_c as the mark between the supercooled liquid and the glasses.

1.3 Interplay of structure and dynamics in silicate melts

In sodium silicate melts the dynamics of sodium ions and the Si-O matrix have been studied with inelastic neutron scattering combining neutron time-of-flight and backscattering methods [MSD02]. Structural relaxations of these different species, despite the large difference in their timescales, have all shown a stretched exponential decay, as predicted by mode coupling theory. This indicates that they are not simple activated processes. Dry sodium (tri)silicates are known as fast ion conductors for very long time. The transport coefficient of the sodium ions is decoupled from that of the Si-O network by several orders of magnitude which has been studied in detail with the tracer diffusion measurements [JBB51], with measurements of the viscosity [KDSW96] and also recently with the inelastic neutron scattering experiments [KMKS06] (Fig.1.2).

In silicates there are generally two classes of constituents: network former and net-

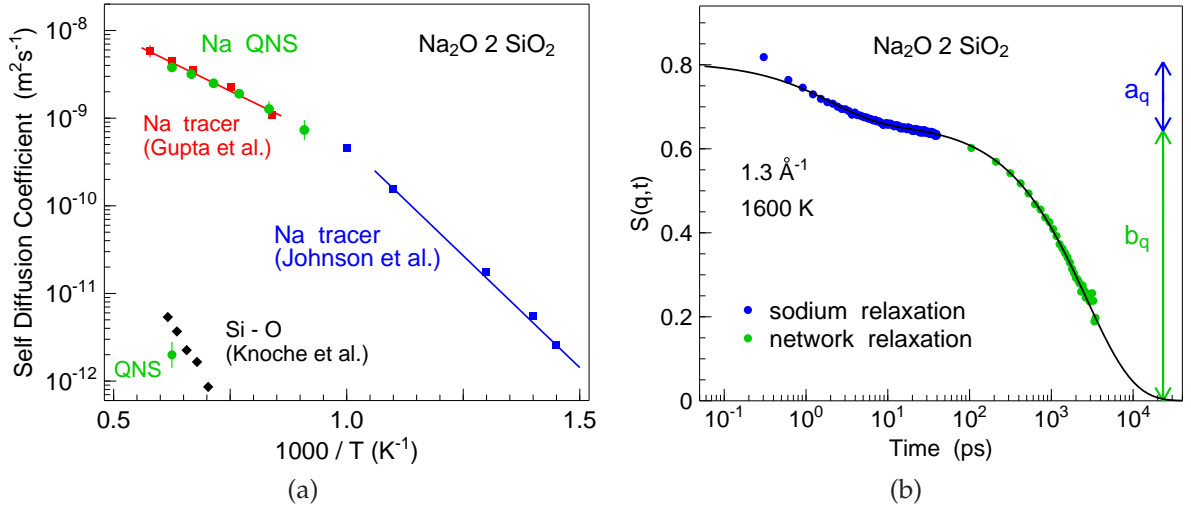


Figure 1.2: Decoupled structural relaxation timescales and transport coefficients in sodium silicates. a) Transport coefficients of different species in sodium disilicate. Sodium ions are of orders of magnitude faster than the Si-O matrix. Data are from tracer diffusion measurements, inelastic neutron scattering, and calculated based on viscosity measurements. b) Measured intermediate scattering function on IN5 and HFBS show both stretched exponential decays, however differs in relaxation timescales: the structural relaxation of sodium ions is on a ps timescale while the one of the Si-O network is on a ns timescale [KMKS06].

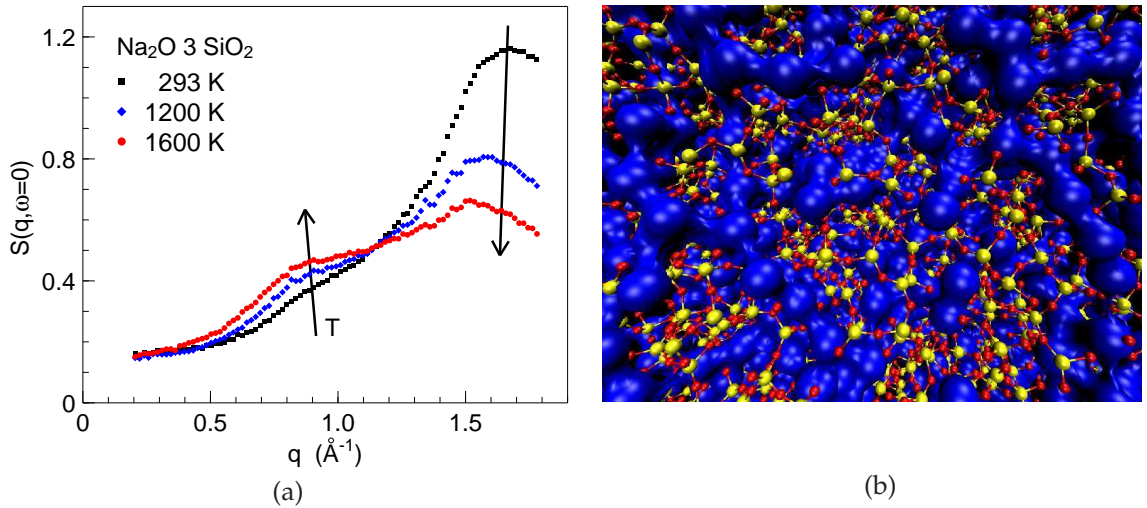


Figure 1.3: Formation of diffusion channels of sodium ions in sodium trisilicate melts studied by inelastic neutron scattering and molecular dynamic simulation [MHK⁺04]. a) Quasielastic structure factor of sodium trisilicate at different temperatures. Note the emerging of a prepeak with increasing temperature at 0.9 \AA^{-1} below the structure factor maximum which is located around 1.6 \AA^{-1} . b) Snapshot of the molecular dynamics simulation of sodium trisilicate melt at 2100 K showing the sodium (blue) rich channels. Silicon (yellow) and Oxygen (red) atoms are shown with a smaller size for clarity.

work modifier, distinguished by their different roles in the formation of silicates. Network formers build up the silicate matrix, for example SiO_2 and Al_2O_3 . Network modifiers disrupted the silicate matrix, like alkali oxides or water. The addition of alkali oxides to silicates causes a non-linear viscosity decrease [HDW95]. Together with the observation of the transport properties of the sodium ions, there is a strong indication of a non-homogeneous distribution of the alkali ions in the silicate matrix. The existence of preferential diffusion pathways of the sodium ions has been recently confirmed by neutron scattering experiments in combination with molecular dynamics computer simulations [MHK⁺04] (Fig.1.3). The prepeak around 0.9 \AA^{-1} in the quasielastic structure factor which emerges at elevated temperatures, corresponds to the distance between the sodium rich channels around $6\text{-}8 \text{ \AA}$. These channels allow fast sodium ion diffusion to be decoupled from the relaxation of the Si-O network. The existence of the channel structure provides as well an explanation for the non-linear drop of the melt viscosity. The Si-O network is only disrupted to certain extent by the addition of sodium oxide. A further increase in its concentration will only fill the channels instead of breaking the Si-O bonds.

The prepeak position depends on the alkali ion size. By increasing the alkali ion size the prepeak position shifts towards lower q numbers (see Fig.1.4a). This indicates that the interchannel distance increases. This can be understood by the fact that larger

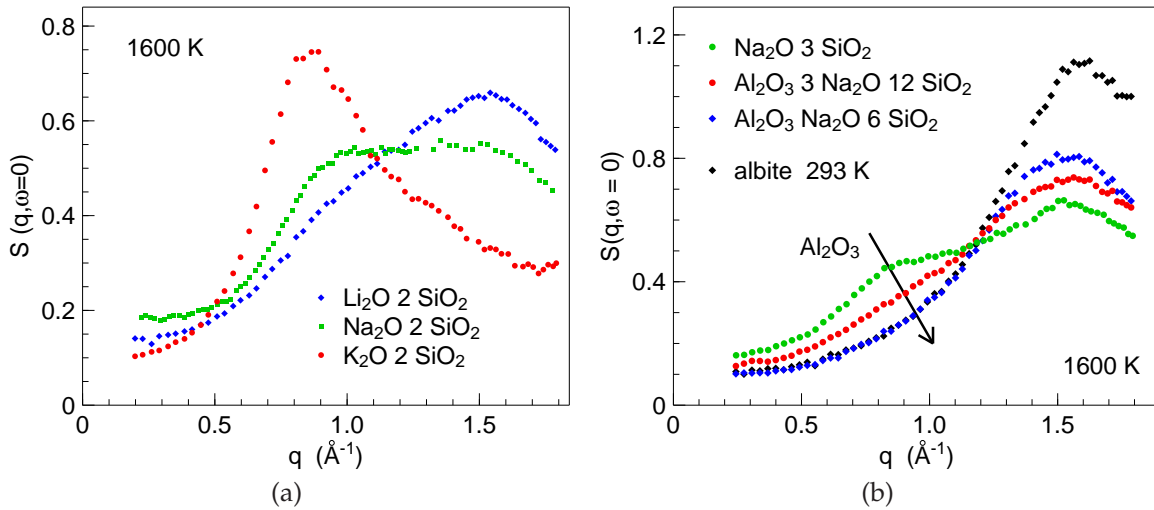


Figure 1.4: Quasielastic structure factor of different alkali silicate and sodium aluminosilicate melts. a) The prepeak position shifts towards smaller q numbers with increasing alkali ion sizes, representing an increase of interchannel distances. b) Vanishing of the prepeak by the addition of network former Al_2O_3 , which is a sign of the channel structure in the alkali silicate melts being disrupted.

alkali ions occupy more space. Vice versa in lithium silicate melts the prepeak nearly merges to the structure factor maximum. In sodium aluminosilicates, by addition of

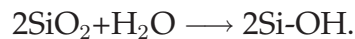
another network former Al_2O_3 the diffusion channels are disrupted. Consequently, the prepeak vanishes and the sodium relaxation in the melt becomes slower [KM04]. The melt viscosity also increases considerably as compared to that of the alkali silicates.

The observation on these silicate melts by means of inelastic neutron scattering shows a clear interplay between microscopic structure and dynamics in the systems. Due to the stoichiometric similarity between the alkali oxides and water, such behaviours could also exist in hydrous silicate melts.

1.4 The hydrous silicate system

Water has a very similar effect on the silicate melt viscosity as that of the alkali oxides. On the addition of only very small amount of less than 1 wt% of water to silicates the melt viscosity drops already by several orders of magnitude, whereas further increasing the water content only changes slightly the viscosity [DRH96] (Fig.1.5a).

It is generally accepted that upon its dissolution, water reacts with the Si-O matrix via the following reaction:



Systematic studies show that water is dissolved into silicate in two fundamental forms: hydroxyl group and molecular water. This chemical equilibrium, which can be driven by external conditions, puts a major challenge in the study of hydrous silicate systems. The ratio between the concentration of these two species depends on pressure, temperature, total water content and composition of silicates. The water speciation has been studied with different spectroscopy methods, for instance infra-red and near infra-red experiments [Sto82, MPSR93] or NMR spectroscopy [KDS89] in the glassy state as well as in the melt [BN03], in order to understand its dependence on different silicate systems and conditions.

The motivation behind these studies is to be able to predict the melt viscosity using the knowledge of the water speciation. It is believed that the hydroxyl group is responsible for the huge viscosity drop since it is the resulting product from the water-silicate reaction which breaks the Si-O bonds. The dependence of the hydroxyl group concentration on the total water content seems also to be correlated with the non-linear viscosity change. At low total water content hydroxyl group is the dominant species. With increasing total water content its concentration levels off and at high water content the concentration of the molecular water increases correspondingly (see Fig.1.5b).

The majority of these studies are performed in the glassy state or employed a quenching techniques to reveal the melt properties, thus high pressure condition is not required for measurements. However, the results measured in the glassy state

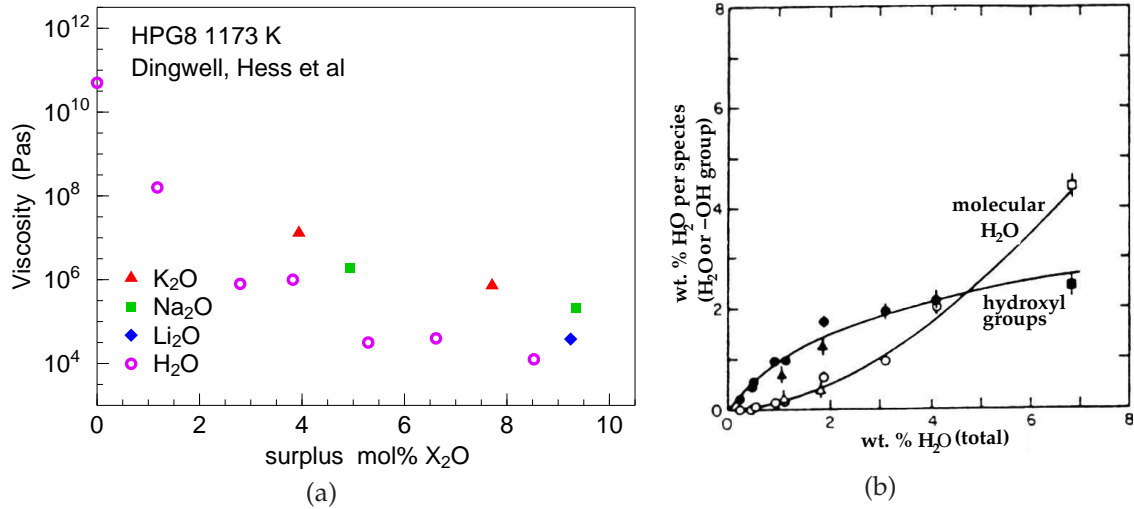


Figure 1.5: Viscosity of hydrous silicate melts and the water speciation. a) Viscosity of the HPG8 (haplogranitic silicate, a synthetic rock analog, consisting of Na_2O , K_2O , SiO_2 and Al_2O_3) melt as a function of the concentration of different network modifiers. After [DRH96]. b) Concentration of different water species in various silicate glasses as a function of total water content, from [Sto82].

do not directly represent the melt properties. It has been shown that in the glassy state the water species are tightly bonded to the silicate network and therefore the vibrational density of states of the hydrogen depends strongly on the silicate composition but only shows very weak dependence on the total water content. Structure studies employing X-ray and neutron diffraction on hydrous silicate glasses show although the viscosity of the melt has been decreased by orders of magnitude, the static structure factor of the Si-O network in the glassy state remains nearly unaffected. [ZVEK92, ZKHS96, PMM⁺].

The observation in the glassy state with quenching techniques cannot be easily extrapolated to the molten state. Corrections must be taken into account since it has been already shown that the assumption that the water speciation does not change upon quenching is not strictly true, especially at high temperatures since the OH/ H_2O conversion is relative fast [ZSI95]. Besides the technical challenge of high temperature high pressure measurements, the direct investigation on melt with optical spectroscopy subjects to another correction due the optical absorption coefficients depending on temperature and silicate composition [GM98]. Chemical diffusion coefficient hence also depends considerably on the composition. An overview of the discussion on these topics can be found in e.g.: [Zha99, BN03].

Therefore, It is still an open question what the basic mechanisms of water dissolution are [McM94] and how the macroscopic properties like viscosity are related to the

microscopic structure and dynamics. For transport properties, the chemical diffusion coefficient of water varies considerably as function of silicate composition. However, the basic diffusion mechanism of water is not known.

1.5 Present work

Quasielastic neutron scattering allows model free investigations of dynamics on a microscopic time and length scales. In these experiments usually neutrons with long wavelengths are used and the accessible momentum transfers are limited compared to neutron diffraction experiments. Hence, the measurements are not optimized for structural investigations. However, the intrinsic q resolution of the quasielastic neutron scattering allows to study the diffusion mechanisms by analyzing the q dependence of the scattering amplitude and its line shape in great detail. Such technique has been already demonstrated to be a powerful tool for the study of water species dynamics in hydrous silicate glasses. A temperature range up to the glass transition temperature of the system has been investigated [IHB⁺05] under ambient pressure conditions.

Dynamics in the temperature range well above the glass transition in the molten state has not yet been studied with neutron scattering techniques. However, since neutron beams exhibit large penetration depths in metals, studies with massive high pressure apparatus is possible. Therefore, neutron scattering techniques at high temperature high pressure conditions open up new possibilities to directly investigate dynamics in hydrous silicate melts under magma chamber conditions on an absolute scale. Owing to the huge difference between the scattering cross sections of H and D, a contrast variation via $\text{H}_2\text{O}/\text{D}_2\text{O}$ substitution gives access to the pure proton signal.

Pure silica, sodium trisilicate and sodium aluminosilicate with $\text{Na}_2\text{O}/\text{Al}_2\text{O}_3$ ratio equal to unity are chosen as the dry silicate compositions for current work. Their composition varies from a single component system (SiO_2) to a three components system (Na_2O , Al_2O_3 , SiO_2). Hydrous silica is the most simple hydrous silicate system. Car-Parrinello computer simulation has been performed on the $\text{SiO}_2\text{-H}_2\text{O}$ system at very high temperature (3000 K) in the liquid state [PBK04]. On the other hand, only a few experimental studies have been conducted till now above the glass transition temperature.

The sodium aluminosilicate $\text{NaAlSi}_3\text{O}_8$ is known as the albite composition. It is the most simple nature volcanic rock composition and was thus largely interested in the geoscience. Lots of data exist on the concentration of water species and melt viscosities at different pressure, temperature and water content conditions. Therefore, neutron scattering is a complimentary method which can provide additional informations of the system and the results can be easily compared with the results from other

investigations.

The melt viscosity of these three systems spans over many orders of magnitudes. In the hydrous silica glass with 10 mol% total water content, water is known to be exclusive dissolved as OH groups [Pöh05]. In the hydrous albite glass with the same water content both OH and H₂O groups exist. In dry SiO₂ and albite the silicate network is fully polymerized, whereas in sodium trisilicate open structure of diffusion channels is known to be present. With the comparison of the neutron scattering experiments on different compositions, current work tries to address the question whether and how the microscopic water dynamics depends on the water speciation, melt viscosity, silicate composition as well as the melt structure in order to understand the dissolution and transport mechanisms of water in the hydrous silicate melts.

It will be shown later that interestingly the water dynamics in pure silica and albite systems is not so fast as expected, if one considers the fact that the glass transition temperature of the samples with 10 mol% water content has dropped almost by a factor of two compared to that of the dry samples. Unfortunately the slow dynamics cannot be studied with the neutron time-of-flight experiment since it is out of the measurable timescales. Further investigations with larger timescales should give access to these diffusive dynamics. In hydrous sodium trisilicates a diffusion mechanism has been proposed, which is not correlated with the water speciation according to the observation with neutron time-of-flight spectroscopy.

Chapter 2

Sample synthesis

The procedure of synthesis and characterization of water bearing silicate glasses are described in the following sections. Sodium trisilicate ($\text{Na}_2\text{O} \cdot 3\text{SiO}_2$, NS3), sodium aluminosilicate ($\text{Na}_2\text{O} \cdot \text{Al}_2\text{O}_3 \cdot 6\text{SiO}_2$) and pure silica (SiO_2) samples with different $\text{H}_2\text{O}/\text{D}_2\text{O}$ contents are prepared. Characterization methods including calorimetry and dilatometry measurements.

2.1 Preparation of the dry silicates

Dry silicates are synthesized by high temperature fusion of ultrapure powder of corresponding oxides and carbonates. Synthesis temperatures are 1250 °C for sodium trisilicate and 1450 °C for sodium aluminosilicate samples, respectively. Typical synthesis times are 12 - 24 hours. Even longer preparation time is not preferred due to the increasing amount of the sodium evaporation, which will lead to alternation of the sample composition. This issue is more important for the sodium aluminosilicate composition since the samples are prepared at higher temperatures and the macroscopic properties depend strongly on the exact Al_2O_3 / Na_2O ratio when it is close to unity.

Typically 25-40 g of silicate glasses were synthesized to reduce the uncertainties of the composition. The deviation of the sample masses from the theoretical calculation is typically below 10 mg. The uncertainty of the composition is therefore in the per mille range. Such small uncertainties will not lead to changes in the microscopic dynamics.

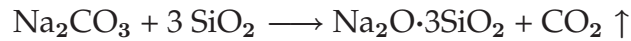
Sodium trisilicate samples are synthesized from Na_2CO_3 (Merck 99.999% metal basis) and SiO_2 (Alfa Aesar 99.995% metal basis, Suprasil¹). Sodium aluminosilicate samples are prepared with additional Al_2O_3 (Alfa Aesar 99.995% metal basis).

All powders were kept in a dry oven at 114 °C for at least 24 hours prior to the synthesis. Al_2O_3 and SiO_2 powders were dried separately again at 1000 °C for 1 hour

¹Suprasil® is the trademark of W. C. Heraeus-Schott Company, Germany. It represents silica glasses produced by hydrolyzation of SiCl_4 . This material is practically free of metallic impurities [Brü70].

at the beginning of the preparation. Oxides and sodium carbonate were then mixed up with a proper amount of each component for the desired silicate composition.

To prepare sodium trisilicate the well mixed powder was then transferred into a Pt-0.5% Au crucible. At elevated temperature sodium carbonate is decomposed and sodium trisilicate is obtained via following reaction:



The mixture was stepwisely transferred into the crucible. In each step 8-10 g powder were filled. Between each step the crucible was heated to 1250 °C and kept for about 1 hour. Therefore the amount of gasses which is evaporated during each filling step is relatively small and sample material losses due to foaming out of the crucible can be avoided. After all of the raw materials were transferred into the crucible the melt was annealed at 1250 °C for 12-15 hours. Due to the relatively low viscosity of sodium trisilicate at this temperature (around $10^{1.37} \text{Pa} \cdot \text{s}$ [KDSW96]) such annealing time is sufficient to obtain a homogeneous, transparent melt (Fig.2.1).

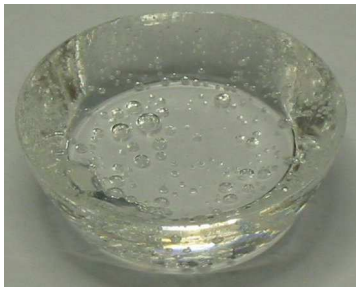
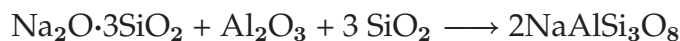


Figure 2.1: Dry sodium trisilicate block sample after preparation, removed from the Pt-0.5% Au crucible. The sample is homogeneous and transparent after the high temperature fusion. Small cylinders can be then drilled out of the block for later sample preparation.

Sodium aluminosilicate samples were prepared using sodium trisilicate as a starting material. The sodium trisilicate precursor was milled into fine powder and mixed together with proper amount of Al_2O_3 and SiO_2 powder. Al_2O_3 and SiO_2 are dissolved at high temperature by the sodium trisilicate melt:



The dissolution of aluminum oxide was slow even at the maximum synthesis temperature of 1450 °C. In order to speed up the homogenization, the melt was stirred using a Pt spindle for 24 hours. After the inspection of a transparent melt the crucible was removed from the furnace and quenched.

For all the samples synthesized in this work a quenching rate achieved by removing the crucible from the high temperature furnace and leaving it at the ambient temperature is sufficient to obtain a glassy sample.

Dry SiO_2 was directly taken from the reagent available from Alfa Aesar with the specification listed above. The powder was ground and dried at 1000 °C prior to further processing.

2.2 Dissolution of water

To prepare the hydrous samples two different sample geometries, either small cylinders or fine powder, of the dry silicates were used. Cylindrical geometry could reduce the amount of air in the sample capsules. Therefore after preparation the samples have nearly no air bubble and for neutron experiments the geometry of the samples in the beam is well defined. However, the reaction rate of water with the samples will be slow. Consequently for higher viscosity samples like albite and silica a complete dissolution of the water can not be achieved within a feasible preparation time. Powder samples have the advantage that the reaction between the sample and water is faster than the cylindrical block samples. However, the prepared samples may contain more air bubbles.

To drill cylindrical sample pieces the sample block (with a thickness of 15-20 mm) was first annealed at a temperature slightly below its glass transition temperature for 5 hours and then cooled down slowly with a cooling rate of 1 K/min to remove the thermal stresses induced by the fast quenching during the preparation stage. Then the block was glued to a glass substrate by epoxy resin for fixation during drilling. Ethanol (ROTIPURAN® > 99.8% from Carl Roth) was used as a coolant during drilling. Typically cylinders with 4 mm diameter and 15-20 mm in length were obtained. After the drilling the cylinders were first dried at 114 °C for 24 hours and then heated up to 450 °C and kept for 10 hours. Then the samples were additionally polished with sand papers to make sure that all organic residuals were removed.

The prepared dry silicate samples are regarded as having nominal "0" mol% water content, although they might contain a minor amount of water for following reason: such minor amounts of water are typically in the ppm range whereas the added water content is about 10 mol% (or 3 wt%). Thus, this is a minor contribution to the total water content and will not alter the properties of the sample, since in this concentration range they are not sensitive to the total water content (See e.g.: [DRH96]).

2.2.1 Sample capsules

Sample capsules are prepared from Pt tube with 5 mm outer diameter and 0.2 mm wall thickness. The Pt tubes were delivered with a length of 1000 mm. For the sample preparation they were cut into 40 mm long pieces. After cutting the tubes were first

cleaned using ultrasonic bath with acetone and de-ionized water to remove organic residuals. They were then put into a hydrofluoric acid bath for at least 24 hours to remove metal and oxide impurities. After taken out from the acid bath and cleaned again with de-ionized water, the tubes were annealed at 1000 °C for 12 hours followed by cooling down slowly (~ 5 °C/min) to ambient temperature. This cleaning procedure makes the Pt tubes relative soft and ready to load the sample. The tubes are stored in a desiccator to avoid moisture exposure.



Figure 2.2: Glass cylinders drilled out of sample blocks and a Pt tube after cutting and cleaning to load them. Cylinders have typically a length around 15 mm and two of them can be loaded in one capsule. The rest of the capsule around 10 mm in length are used for plasma welding.

To prepare the capsules the tubes were first closed on one end using a micro-plasma welding machine. After sealing the capsule was loaded with dry silicate samples and $\text{H}_2\text{O}/\text{D}_2\text{O}^2$ for the desired water concentration. Samples with 10 mol% water content for each dry silicate composition were prepared for the neutron scattering experiments. In addition samples with 5 wt% and 5 mol% water content were prepared as well. The conversion from mole fraction to weight fraction for each silicate composition with 10 mol% water is shown in Tab.2.1. It should be pointed out here that

silicate composition	wt% of H_2O	wt% of D_2O
$\text{Na}_2\text{Si}_3\text{O}_7$	3.20	3.54
$\text{NaAlSi}_3\text{O}_8$	2.96	3.28
SiO_2	3.33	3.57

Table 2.1: Conversion of 10 mol% water content to weight % for different sample compositions

there exist various definitions of water mole fraction in the silicate system [Zha99] due to different definitions of the silicate "molar unit". From the chemistry point of view this is rather a philosophic task than having any particular physical or chemical reason since there is no single molecule in the real silicate system. The entire sample is one large network and the chemical formula only represents the relative abundance of each element. In this work the calculation follows the definition of mole fraction used by

² D_2O with 99.8% deuteration degree from Merck.

[MVC98] which is also used commonly by geologists. Each oxide is considered as one unit. Therefore, sodium trisilicate has four units and albite composition is treated as having eight units.

After loading these capsules were sealed on the other end. During the second welding procedure most part of the capsule body was pressed into a copper block for heat dissipation so that the capsule was kept at ambient temperature except at the welding position. Therefore, water loss during the welding process is negligible. Typical amount of 0.5-0.6 g dry silicate together with of about 20 mg of water were loaded in one capsule.

Sealed capsules were weighted and put into a dry oven at 114 °C for at least 12 hours. Then capsules were checked by weight to eliminate leakages. Only capsules without significant weight loss (<1 mg) after the heating were used in further preparation. Water content is then controlled by means of capsules' weight after each step of processing. This is performed directly after the high temperature high pressure fusion as well as after the capsules being opened and subsequently heated up in the dry oven. For the samples used for neutron scattering experiments weight losses in the preparation stage are smaller than 5% of the added water amount. Hence, most of the water is dissolved in the silicate sample.

2.2.2 High temperature and pressure process

To dissolve water into the silicates, the sample capsules have to be heated at high temperature under high pressure. Therefore, an autoclave with built-in furnace is used for sample preparation. In current work a pressure vessel from the company Dustec® was used. The pressure vessel can be operated under a pressure range of 0-3000 bar, a temperature range of 0-300 °C with a pressurized volume of 0.65 l. Pressures are generated by a membrane compressor from Nova Swiss using Ar gas as pressure medium. The complete setup is shown schematically in Fig.2.3. A pressure indicator from Nova Swiss with two measuring sensors with an accuracy of $\pm 0.5\%$ is used to monitor the pressure. One measures the pressure direct after the compressor. During the sample preparation valve V3 is closed and the pressure in the autoclave is monitored by another sensor shown in DP2.

A self-made furnace was used to heat up samples under high pressure (see Fig.2.4a). The furnace is constructed with thin wall Al_2O_3 ceramic tubes surrounded by PtRh heating wires. The furnace is divided into three heating zones which are controlled independently via an Eurotherm controller 2704 with three controlling circles. Temperature of each heating zone was monitored in the middle of the zone by a Pt/Pt10Rh thermal couple (Type-S). The whole furnace is put into a steel shell and in between filled with MgO powder for thermal isolation. Typically an electrical power of about

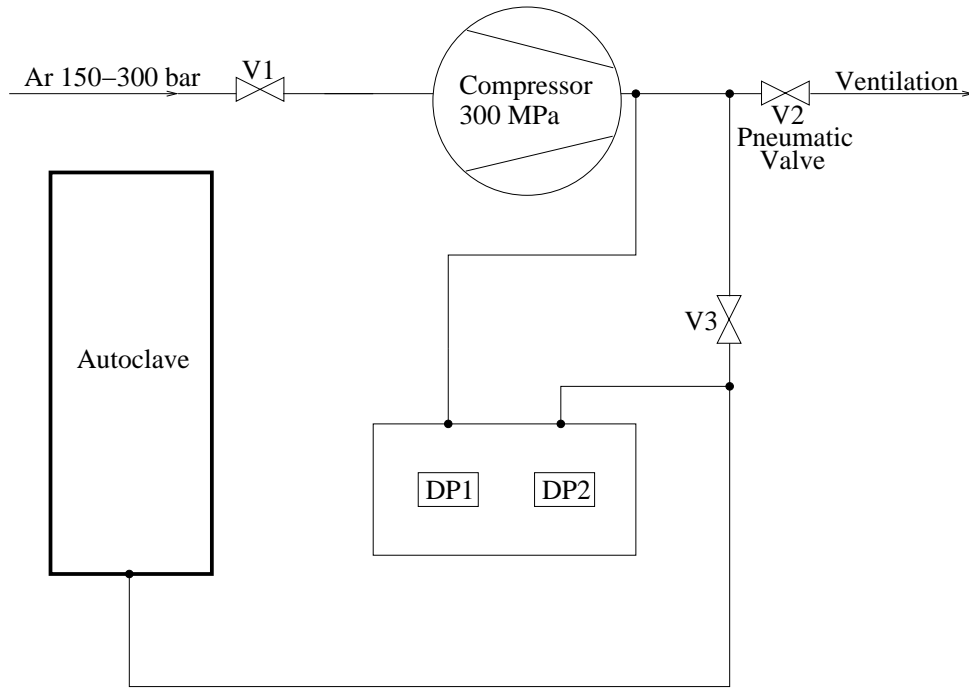


Figure 2.3: Schematic view of the sample preparation setup. The compressor is supplied by Ar gas with a pressure of 150 - 300 bar, controlled via valve V1. With valve V2 closed and valve V3 open, the compressor is able to provide a pressure in the autoclave up to 300 MPa. Pressure direct after the compressor is measured and displayed in DP1. During the sample preparation V3 is closed to keep the pressure in the autoclave relative constant, which is measured and displayed in DP2. After preparation with both V2 and V3 open, the pressure in the autoclave can be slowly released.

1.2 kW is needed to heat the furnace to the sample preparation temperature around 1500 K under a pressure of 300 MPa.

Samples were mounted on a movable stage with an additional thermal couple close to the capsules to monitor its temperature. Using a three heating-zone setup provides a relatively homogeneous temperature over the sample region, which can be seen in Fig.2.5b measured by driving the stage into different positions in the furnace by a motor.

The hydrous sodium trisilicate samples were prepared at a temperature of 1250 °C and the albite and pure SiO₂ samples were prepared at 1400 °C. The preparation time of the samples varies from 5 up to 15 hours. Samples were pressurized and placed between 2nd and 3rd heating zone (see Fig.2.5a) before heating. At beginning the autoclave is filled with Ar to reach a pressure of about 180-200 MPa in the cold state. During heating up the furnace, the pressure will be built up to 300 MPa. The autoclave is water cooled from outside during the sample preparation. The samples were heated up with

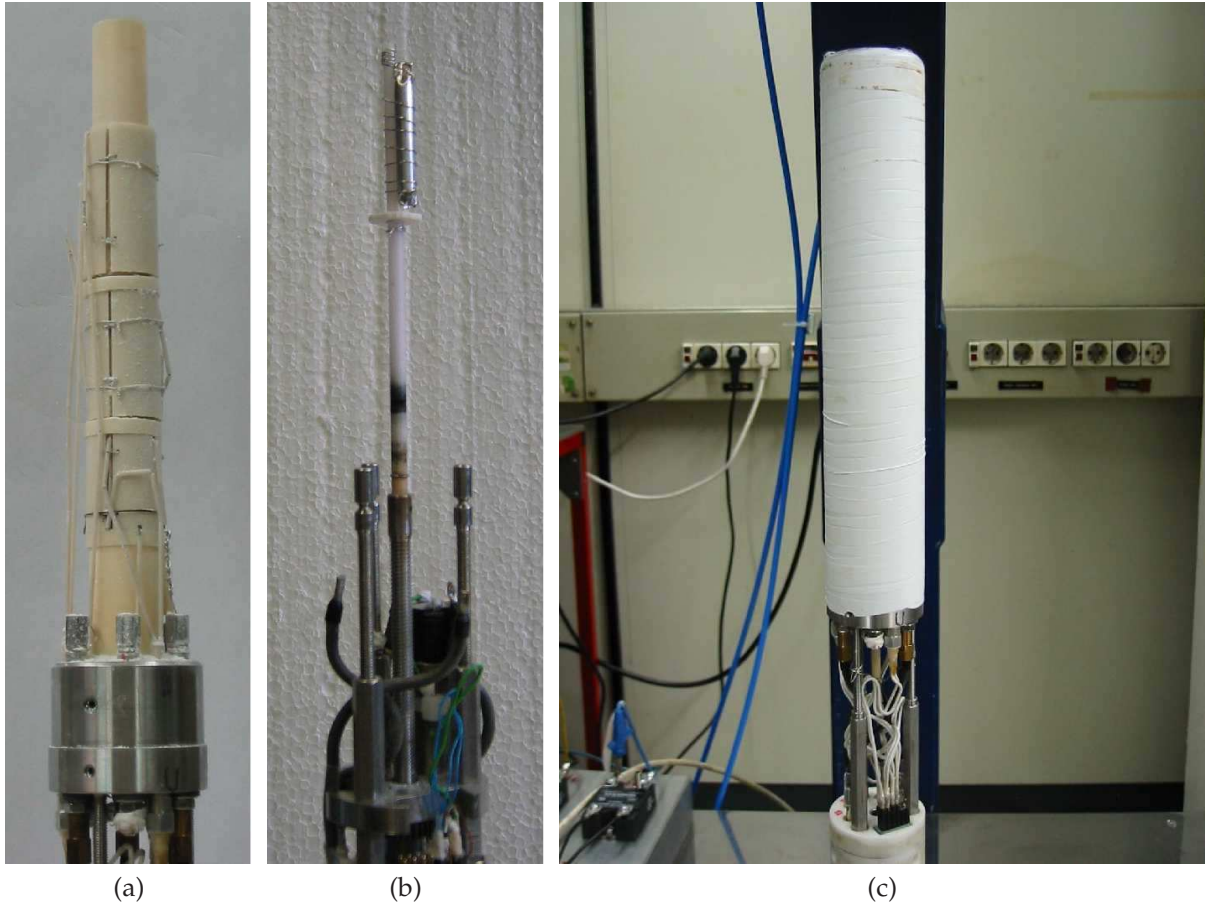


Figure 2.4: Three-zone furnace for sample preparation. a) Furnace without the thermal isolation and the outer shell, showing the three heating zones. The thermal couples are enclosed in the ceramic capillaries. b) Movable stage mounted with one sample capsule, part of the motor can be seen as well. c) Closed furnace mounted on the base stage of the autoclave. The furnace is wrapped with Teflon tapes so that it can be inserted smoothly into the autoclave.

a ramp rate of about 60 K/min to the target temperature. After the desired annealing time, they were quenched adiabatically passing through their glass transition temperatures. Water was then frozen in the glassy state. Quenching is achieved by driving the sample capsules into the cold zone at the bottom of the furnace (cf. Fig.2.5b). The quenching rate is measured by the thermal couple close to the samples to be of about 200 K/min down to T_g . After this high temperature high pressure process the Ar gas pressure medium is slowly vented and samples are taken out from the autoclave.

Deuterated samples are prepared with special care. At the first attempt to prepare deuterated silicates, samples were found later during the neutron experiments to be exchanged with H_2O . This problem has been already encountered in an earlier study [Mül03]. Although the platinum capsules with a larger wall thickness of 0.2 mm were used here this exchange was still not hindered. The later D_2O samples were

D₂O containing samples were successfully prepared. Further improvement could be to enclose the sample capsule completely in another capsule with D₂O buffer loaded and using some H blocking noble metals or alloys as outer capsule material (e.g.: Pt-Au alloy).

The prepared samples were taken out from the capsules and kept in a desiccator. Usually single piece of samples with 0.4-0.5 g can be obtained from one capsule. The rest of the samples either stick to the Pt capsule or break into small pieces. For sample characterization small pieces of samples can be used.

2.3 Sample characterization

The macroscopic properties of the sample are measured with calorimetry/dilatometry for T_g in order to confirm that the samples are homogeneous and having the correct water content before the neutron scattering experiments.

2.3.1 Calorimetry

The glass transition temperature of the hydrous sodium trisilicate samples were measured with differential scanning calorimetry (DSC). Pieces from different positions of one and the same sample were taken. The weight of these pieces is usually in the range of 10-15 mg. The ramp rate used is 15 K/min for all measurements. Fig.2.6 shows the

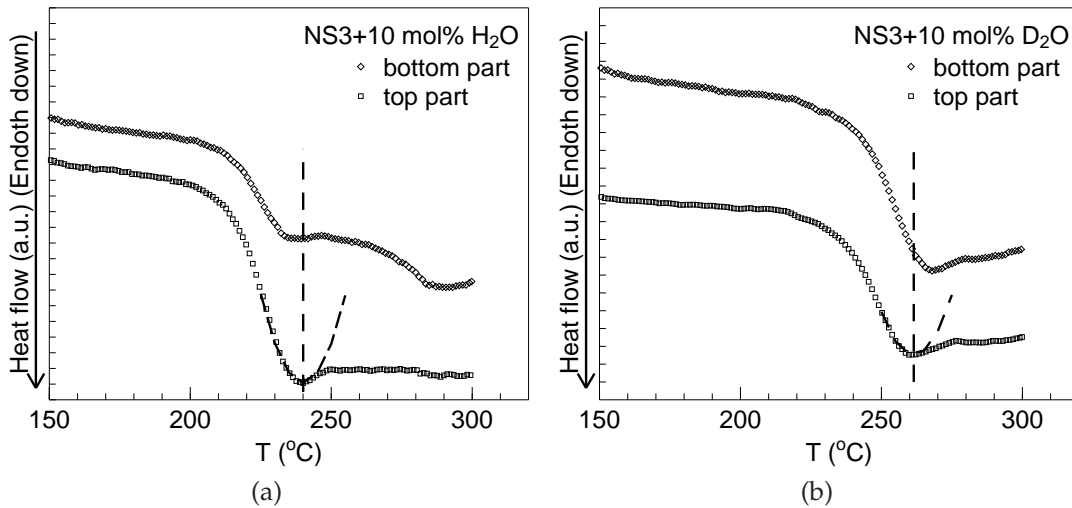


Figure 2.6: DSC measurement curve for different hydrous NS3 samples: a) with 10 mol% H₂O. b) with 10 mol% D₂O.

DSC measurements on a NS3+10mol% H₂O sample and a NS3+10mol% D₂O sample after preparation. The glass transition temperature is characterized by an excess heat

flow required by the samples. The measured calorimetry T_g depends on the experimental factors like thermal history, ramp rate during the measurement, and methods of data evaluation. Therefore, the resulting T_g 's are normally subjected to an uncertainty of about 10-15 °C. The transition temperatures here were obtained by fitting a parabola to the peak minimum. This algorithm of evaluation has already been used in a previous study [Kar05].

It can be seen from the measurement curves that the top and bottom part of each sample are close to each other. This is an indication that the water content in the sample is homogeneous. The T_g of D₂O samples with the same sample is around 20 K higher than the H₂O sample. However, this is believed to be mainly caused by the difference in the quenching rate of the sample since the D₂O samples cannot be completely driven to the bottom of the furnace due to the presence of the buffer capsule. According to the weight controlling, the samples should have the same water content³. This is later confirmed by the counting rate in the neutron experiment according to the scattering cross sections of the samples. Although the T_g measured here can not be used as a direct measure of the water content, the obtained values are closed to the reported values [TTA⁺83]. One should note as well that the glass transition temperature of the dry sodium trisilicate is located at approximately 470 °C [MSS83]. The dissolution of water into silicates drastically reduces the T_g of the silicates.

2.3.2 Dilatometry

For albite and pure silica composition the T_g of the water bearing glasses with 10 mol% water content (around 600-700 °C) is out of the measurable range of the DSC instrument. Thus the samples were measured with dilatometry at the department of earth and environmental sciences, section for mineralogy, petrology and geochemistry, Ludwig-Maximilians-University Munich together with Dr. K.-U. Hess. Instead of measuring the heat flow in dilatometry the change of the sample dimension is recorded as a function of temperature. Thus the basic physical quantity behind is essentially the thermal expansion coefficient of the sample, which is changing at T_g . Typically a sample disk of about 4 mm in diameter and 1 mm in thickness is prepared with plane parallel surfaces. Measurements were performed using Bähr DIL 802V vertical dilatometer equipped with an alumina push rod under constant Ar gas flow. A heating rate of 10 K/min was used for all measurements. The change of the push rod position is recorded against the sample temperature. It should be mentioned that the data pre-

³The glass transition temperature of the samples are very sensitive to the cooling rate of the samples close to their glass transition temperature. In case of the samples which are not quenched by being driven to the cold zone but cooled down with the furnace, the glass transition temperatures at different positions of the sample can differ from each other by more than 100 K due to the different cooling rates in the furnace which vary by a factor of about two.

sented here can not be easily related to the sample thermal expansion coefficient since only the raw data is plotted, which is contributed not only from the expansion of the samples but also from the whole apparatus including the alumina push rod. However, the characteristic transition temperatures can be still determined.

Fig.2.7 shows a comparison between the dilatometer measurement and a DSC measurement on the same NS3+5wt% H₂O sample. For the dilatometer measurement

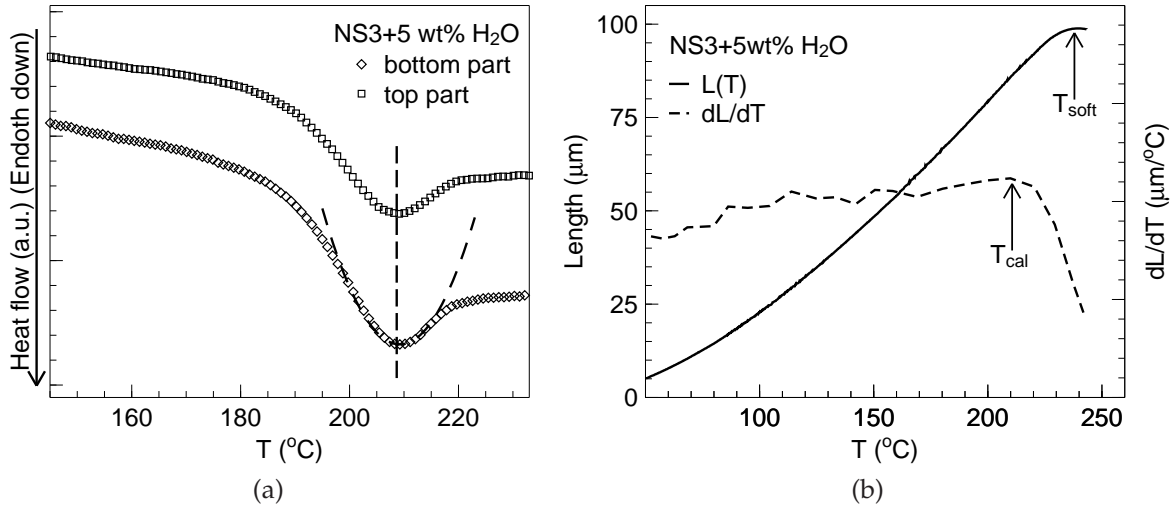


Figure 2.7: Comparison between the DSC measurement results and dilatometry measurement results on a NS3+5wt% H₂O sample: a) DSC measurement. b) Dilatometry measurement.

one can identify two different characteristic temperatures⁴. Close to the end of the scanning curve there is a "softening" point T_{soft} where the scanning curve reaches its maximum. At this temperature the corresponding sample viscosity is of the order of $10^{9.7}$ Pa·s. The program stops shortly after the detection of this point automatically to avoid large deformation of the sample. Before the softening point there is another characteristic temperature T_{cal} which is more clearly visible in the derivative curve where the scanning curve deviates from linear like behaviour. This corresponds to the sample viscosity of the order of $10^{11.3}$ Pa·s, which is compatible to the glass transition temperature measured with the conventional calorimetry methods. For the NS3 sample the softening temperature and the calorimetry glass transition temperature are located around 240 °C and 210 °C, respectively. Compare to the DSC measurement it is clear that the results from these two methods agree within the error bars, although there is a small heating rate difference between the two different methods (5 K).

A measurement on a dry albite sample with dilatometry is shown in Fig.2.8. T_{cal} and T_{soft} can be again identified in Fig.2.8a at 850 °C and 1039 °C, respectively. Furthermore, a second run was subsequently conducted after the first measurement was

⁴Detailed description of the dilatometric method and the corresponding viscosities at characteristic temperatures can be found in e.g.: [HDW95, RPM⁺01].

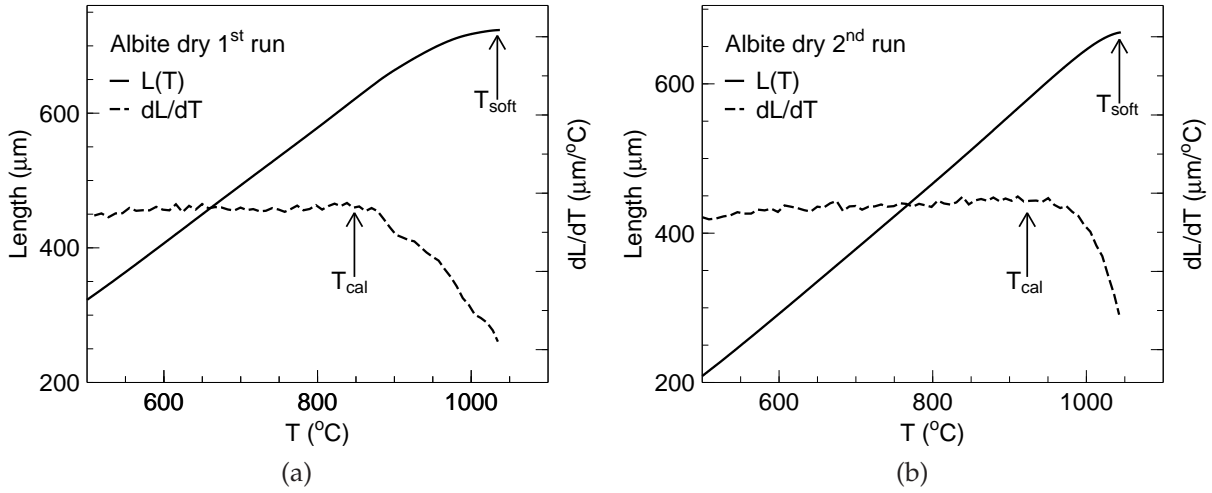


Figure 2.8: Measurements on dry albite sample with dilatometry: a) first measurement. b) Second measurement.

finished and the sample was cooled down with the furnace of the dilatometer. It can be seen that in the second measurement the T_{cal} and T_{soft} are now located at 920 $^\circ\text{C}$ and 1051 $^\circ\text{C}$ respectively, slightly higher than the first measurement. This can be understood that in the first run the sample was subjected to a high quenching rate during the preparation stage. Before the second measurement the sample was cooled down together with the dilatometer furnace where the cooling rate is much smaller and the sample is now relaxed to some extent which results a higher transition temperature, a phenomenon well known for glass transition.

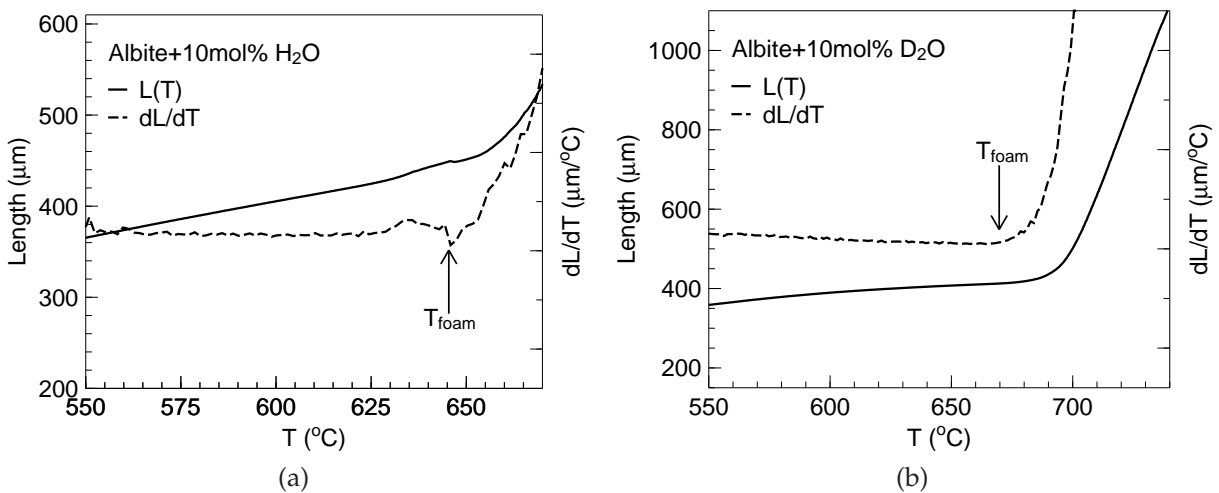


Figure 2.9: Dilatometry measurements on albite samples with 10 mol% H_2O and D_2O . Only the foaming temperature can be identified. a) H_2O containing sample. b) D_2O containing sample.

Albite samples with 10 mol% H_2O and D_2O are measured as well. However, as

plotted in Fig.2.9 no softening point nor calorimetric glass transition temperature can be found. In stead the sample shows enhanced expansion after certain temperature. Actually this is the temperature where the foaming process starts in the sample. In the water bearing NS3 samples this can be also observed in the DSC measurement at a temperature around T_g+50 K. In the hydrous albite samples it seems that the glass transition temperature and the foaming temperature are no longer well separated and foaming starts directly after the glass transition temperature is reached. Thus only the foaming temperature can be used to characterize the sample. Nevertheless, it can be seen that the foaming temperatures of the H₂O and D₂O containing samples are still close. Therefore, no large difference in the water content between these two samples is expected.

During the neutron experiments, the water content of the samples (H₂O and D₂O) can be verified according to their cross sections (see Appendix A) by compared them to a standard scatterer. Thus one has a measure of the sample water content on an absolute scale.

Chapter 3

Theoretical background

In this chapter a basic introduction on neutron scattering theory especially the definition of useful correlation functions is presented in the first section. The second section shows how some diffusion cases could be seen by neutron scattering. The third part gives a brief introduction of the mode coupling theory of viscous liquids and glass transitions which provides general explanations and predictions on the structure relaxation of these disorder systems.

3.1 Neutron scattering

Neutron scattering provides simultaneously structural and dynamic informations on the sample. Basic equations of neutron scattering are presented here. For detailed derivation the reader is referred to text books on neutron scattering theory like [Squ78] or [Lov84].

3.1.1 Basic theory

In a neutron scattering experiment the basic quantity is the double differential scattering cross section, which counts the number of scattered neutrons in a solid angle $d\Omega$ and carrying an energy within the interval $[E, E + dE]$. In the neutron time-of-flight experiments performed in this study the measured intensity is directly related to the double differential scattering cross section as will be shown in the following sections.

In general the scattering of neutrons on a target can be either elastic or inelastic, which means the energy of the scattered neutrons can differ from the incident ones. According to the energy and momentum conservation, the double differential scattering cross section of a single scattering process can be written in the form

$$\left(\frac{\partial^2 \sigma}{\partial \Omega \partial E'} \right)_{\lambda \rightarrow \lambda'} = \frac{k'}{k} \left(\frac{m_N}{2\pi \hbar^2} \right)^2 |\langle \vec{k}' \lambda' | \hat{V} | \vec{k} \lambda \rangle|^2 \delta(\hbar\omega + E_\lambda - E_{\lambda'}) \quad (3.1a)$$

where

$$\hbar\omega = \frac{\hbar^2}{2m_N}(k^2 - k'^2) = E - E' \quad (3.1b)$$

denotes the energy transfer to the neutrons¹.

The incident neutrons have the state $|\vec{k}\rangle$ which changes after the scattering to $|\vec{k}'\rangle$. The state of the target changes from $|\lambda\rangle$ to $|\lambda'\rangle$, with corresponding energies E_λ and $E_{\lambda'}$. The interaction between the target and the neutrons is included in the potential \hat{V} .

The matrix element $\langle \vec{k}'\lambda' | \hat{V} | \vec{k}\lambda \rangle$ represents the transition probability of the whole system from the state \vec{k}, λ to \vec{k}', λ' . This has to be evaluated in order to give a proper expression of the double differential cross section. According to quantum mechanics this matrix element is given explicitly by

$$\langle \vec{k}'\lambda' | \hat{V} | \vec{k}\lambda \rangle = \int \psi_{\vec{k}'}^* \chi_{\lambda'}^* \hat{V} \psi_{\vec{k}} \chi_{\lambda} d\vec{R} d\vec{r} \quad (3.2)$$

where ψ and χ are the wave functions of the neutrons and the target system, respectively. For nuclear scattering the interaction between the neutrons and the nuclei is of short range order compared to the wavelength of the neutron. This only holds for non magnetic scattering, whereas for magnetic scattering the interaction range is in the order of the neutron wavelength but rather weak. In the following section only the case of nuclear scattering is discussed, since magnetic scattering where the change of the spin states happens does not present in the sample systems studied in this work. Therefore the Fermi pseudopotential can be used and the Born approximation is valid as well. The pseudopotential of a single fixed nucleus j can be thus written in the form of a δ -function:

$$V_j(\vec{r} - \vec{R}_j) = \frac{2\pi\hbar^2}{m_N} b_j \delta(\vec{r} - \vec{R}_j) \quad (3.3)$$

that the neutron at the position \vec{r} feels the potential of the nucleus only at \vec{R}_j where it is sitting. The b_j is the scattering length of the j atom. The potential of the whole scattering system can be given by a sum over all the nuclei

$$\hat{V} = \sum_j V_j(\vec{r} - \vec{R}_j) = \frac{2\pi\hbar^2}{m_N} \sum_j b_j \delta(\vec{r} - \vec{R}_j). \quad (3.4)$$

After inserting the potential and the wavefunction of the neutrons (as plan wave), the integral over the neutron position \vec{r} can be carried out. The double differential scatter-

¹Here a positive energy difference represents neutron energy loss according to the common definition of the energy transfer $\hbar\omega$ in the neutron scattering theory and a negative sign means neutron energy gain. In the experimental data however, conventionally an opposite definition is used: a positive energy difference denotes neutron energy gain.

ing cross section reads

$$\left(\frac{\partial^2 \sigma}{\partial \Omega \partial E'} \right)_{\lambda \rightarrow \lambda'} = \frac{k'}{k} \left| \sum_j b_j \langle \lambda' | e^{i\vec{q} \cdot \vec{R}_j} | \lambda \rangle \right|^2 \delta(\hbar\omega + E_\lambda - E_{\lambda'}) \quad (3.5a)$$

where

$$\langle \lambda' | e^{i\vec{q} \cdot \vec{R}_j} | \lambda \rangle = \int \chi_{\lambda'}^* e^{i\vec{q} \cdot \vec{R}_j} \chi_\lambda d\vec{R} \quad (3.5b)$$

and

$$\vec{q} = \vec{k} - \vec{k}'. \quad (3.5c)$$

Replacing the δ -function by its integral form

$$\delta(\hbar\omega + E_\lambda - E_{\lambda'}) = \frac{1}{2\pi\hbar} \int_{-\infty}^{\infty} e^{i(E_{\lambda'} - E_\lambda)t/\hbar} e^{-i\omega t} dt \quad (3.6)$$

and using the relation $\mathbf{H}|\lambda\rangle = E_\lambda|\lambda\rangle$, $\mathbf{H}|\lambda'\rangle = E_{\lambda'}|\lambda'\rangle$ gives the result

$$\left(\frac{\partial^2 \sigma}{\partial \Omega \partial E'} \right)_{\lambda \rightarrow \lambda'} = \frac{k'}{k} \frac{1}{2\pi\hbar} \sum_{jj'} b_{j'} b_j \int_{-\infty}^{\infty} \langle \lambda | e^{-i\vec{q} \cdot \vec{R}_{j'}} | \lambda' \rangle \langle \lambda' | e^{i\mathbf{H}t/\hbar} e^{i\vec{q} \cdot \vec{R}_j} e^{(-i\mathbf{H}t/\hbar)} | \lambda \rangle e^{-i\omega t} dt \quad (3.7)$$

where \mathbf{H} is the Hamiltonian of the scattering system and the scattering lengths of the nuclei are assumed to be real numbers. A summation over the final and initial states λ' and λ then averaging over all λ is necessary since in a real experiment not only a single process $\lambda \rightarrow \lambda'$ but an average over all possible transitions is measured. This is represented in the thermal or ensemble average. For an operator \mathbf{A} at temperature T it is defined by

$$\langle \mathbf{A} \rangle_T = \sum_{\lambda} p_{\lambda}(T) \langle \lambda | \mathbf{A} | \lambda \rangle \quad (3.8)$$

where p_{λ} is the probability of finding the scattering system in the state λ determined by the Boltzmann distribution. Using the closure relation for a pair of operators and the definition of the time-dependent Heisenberg operator $\vec{R}_j(t) = e^{i\mathbf{H}t/\hbar} \vec{R}_j e^{-i\mathbf{H}t/\hbar}$ the double differential scattering cross section becomes finally

$$\left(\frac{\partial^2 \sigma}{\partial \Omega \partial E'} \right) = \frac{k'}{k} \frac{1}{2\pi\hbar} \sum_{jj'} b_{j'} b_j \int_{-\infty}^{\infty} \langle e^{-i\vec{q} \cdot \vec{R}_{j'}(0)} e^{i\vec{q} \cdot \vec{R}_j(t)} \rangle_T e^{-i\omega t} dt \quad (3.9)$$

and the scattering function is defined via

$$S(\vec{q}, \omega) = \frac{1}{2\pi\hbar} \int_{-\infty}^{\infty} \frac{1}{N} \sum_{jj'} \langle e^{-i\vec{q} \cdot \vec{R}_{j'}(0)} e^{i\vec{q} \cdot \vec{R}_j(t)} \rangle_T e^{-i\omega t} dt. \quad (3.10)$$

It can be shown that the scattering function is an asymmetric function of ω . The up-scattering (neutron energy gain) probability is the not same as that of the down-scattering (neutron energy loss). In a scattering event the probability of the scattering system being initially in the higher energy state is reduced by a temperature dependent prefactor of $e^{-\hbar\omega/k_B T}$ compared to its probability of being in the lower energy state due to the Boltzmann weighting factor p_λ .

$$S(\vec{q}, -\omega) = e^{-\hbar\omega/k_B T} S(\vec{q}, \omega) \quad (3.11)$$

This is know as the *principle of detailed balance*.

3.1.2 Coherent/incoherent scattering and correlation functions

For a system that contains a large number of different nuclei: a mixture of either different isotopes from one element and/or different atoms from various elements, the double differential cross section measured in an experiment is an average over all different scattering lengths, which is given by

$$\left(\frac{\partial^2 \sigma}{\partial \Omega \partial E'} \right) = \frac{k'}{k} \frac{1}{2\pi\hbar} \sum_{jj'} \overline{b_{j'} b_j} \int \langle e^{-i\vec{q} \cdot \vec{R}_{j'}(0)} e^{i\vec{q} \cdot \vec{R}_j(t)} \rangle_T e^{-i\omega t} dt. \quad (3.12)$$

This average can be separated into two parts under the assumption that there is no correlation between the scattering length of different nuclei

$$\begin{aligned} \overline{b_{j'} b_j} &= (\bar{b})^2 = \left(\sum_i f_i b_i \right)^2, \quad j' \neq j \\ \overline{b_{j'} b_j} &= \bar{b}^2 = \sum_i f_i b_i^2, \quad j' = j \end{aligned} \quad (3.13)$$

where f_i is the relative abundance of the i atom and b_i is the corresponding scattering length. Use the definition of *coherent* and *incoherent* scattering cross sections $\sigma_{coh} = 4\pi(\bar{b})^2$ and $\sigma_{inc} = 4\pi[\bar{b}^2 - (\bar{b})^2]$, the double differential scattering cross section can be represented in the form of

$$\left(\frac{\partial^2 \sigma}{\partial \Omega \partial E'} \right) = \left(\frac{\partial^2 \sigma}{\partial \Omega \partial E'} \right)_{coh} + \left(\frac{\partial^2 \sigma}{\partial \Omega \partial E'} \right)_{inc} \quad (3.14)$$

where

$$\left(\frac{\partial^2 \sigma}{\partial \Omega \partial E'} \right)_{coh} = \frac{\sigma_{coh}}{4\pi} \frac{k'}{k} \frac{1}{2\pi\hbar} \sum_{jj'} \int \langle e^{-i\vec{q} \cdot \vec{R}_{j'}(0)} e^{i\vec{q} \cdot \vec{R}_j(t)} \rangle_T e^{-i\omega t} dt \quad (3.15a)$$

$$\left(\frac{\partial^2 \sigma}{\partial \Omega \partial E'} \right)_{inc} = \frac{\sigma_{inc}}{4\pi} \frac{k'}{k} \frac{1}{2\pi\hbar} \sum_j \int \langle e^{-i\vec{q} \cdot \vec{R}_j(0)} e^{i\vec{q} \cdot \vec{R}_j(t)} \rangle_T e^{-i\omega t} dt. \quad (3.15b)$$

Van Hove [Hov54] introduced the time dependent pair-distribution function $G(\vec{r}, t)$ which describes the correlation between the presence of a particle at \vec{r}' and time $t = 0$ and the presence of a particle at $\vec{r}' + \vec{r}$ and a later time t , averaged over \vec{r}'

$$G(\vec{r}, t) = \frac{1}{N} \langle \sum_{jj'} \int \delta(\vec{r}' - \vec{R}_j(0)) \delta(\vec{r}' + \vec{r} - \vec{R}_{j'}(t)) d\vec{r}' \rangle. \quad (3.16)$$

By introducing the particle density operator

$$\rho(\vec{r}, t) = \sum_j \delta(\vec{r} - \vec{R}_j(t)) \quad (3.17)$$

the pair-distribution function can be rewritten in the form of the general definition of a correlation function - an ensemble average of two operators

$$G(\vec{r}, t) = \frac{1}{N} \int \langle \rho(\vec{r}', 0) \rho(\vec{r}' + \vec{r}, t) \rangle d\vec{r}'. \quad (3.18)$$

Therefore, $G(\vec{r}, t)$ is also known as the density-density correlation function.

For systems which obey Boltzmann statistics, the pair-distribution function splits naturally into a part which contains only the correlation of the positions of a single particle at different times G_s (self) and a part which correlates pairs of distinct particles G_d (distinct), namely

$$G_s(\vec{r}, t) = \frac{1}{N} \sum_j \int \langle \delta(\vec{r}' - \vec{R}_j(0)) \delta(\vec{r}' + \vec{r} - \vec{R}_j(t)) d\vec{r}' \rangle \quad (3.19a)$$

$$G_d(\vec{r}, t) = \frac{1}{N} \sum_{j \neq j'} \int \langle \delta(\vec{r}' - \vec{R}_j(0)) \delta(\vec{r}' + \vec{r} - \vec{R}_{j'}(t)) d\vec{r}' \rangle \quad (3.19b)$$

with the boundary conditions

$$\int G(\vec{r}, t) d\vec{r} = N, \quad \int G_s(\vec{r}, t) d\vec{r} = 1. \quad (3.19c)$$

Applying the definition of the reciprocal particle density operator $\rho(\vec{q}, t) = \sum_j e^{-i\vec{q} \cdot \vec{R}_j(t)}$ the intermediate scattering function $S(\vec{q}, t)$ can be obtained

$$S(\vec{q}, t) = \frac{1}{N} \sum_{jj'} e^{-i\vec{q} \cdot \vec{R}_{j'}(0)} e^{i\vec{q} \cdot \vec{R}_j(t)} \quad (3.20)$$

which is the spatial Fourier transformation of the pair-distribution function $G(\vec{r}, t)$. Thus, the scattering function defined in equation 3.10 is the spatial and time Fourier transformation of the density-density correlation function

$$S(\vec{q}, \omega) = \frac{1}{2\pi\hbar} \int e^{i\vec{q}\cdot\vec{r}} e^{-i\omega t} G(\vec{r}, t) d\vec{r} dt. \quad (3.21)$$

Moreover, from equation 3.15 and 3.19 it can be shown that the density-density correlation and the self-correlation are related with coherent scattering and incoherent scattering intensities, respectively:

$$\left(\frac{\partial^2 \sigma}{\partial \Omega \partial E'} \right)_{coh} = N \frac{\sigma_{coh}}{4\pi} \frac{k'}{k} S_{coh}(\vec{q}, \omega) = N \frac{\sigma_{coh}}{8\pi^2 \hbar} \frac{k'}{k} \int e^{i\vec{q}\cdot\vec{r}} e^{-i\omega t} G(\vec{r}, t) d\vec{r} dt \quad (3.22a)$$

$$\left(\frac{\partial^2 \sigma}{\partial \Omega \partial E'} \right)_{inc} = N \frac{\sigma_{inc}}{4\pi} \frac{k'}{k} S_{inc}(\vec{q}, \omega) = N \frac{\sigma_{inc}}{8\pi^2 \hbar} \frac{k'}{k} \int e^{i\vec{q}\cdot\vec{r}} e^{-i\omega t} G_s(\vec{r}, t) d\vec{r} dt. \quad (3.22b)$$

These quantities are hence experimentally accessible. The advantage of introducing these correlation functions is that it splits the experiment measured information into two parts. One of them depends only on the experimental parameters. The other provides the structure and dynamic information of the samples.

It should be noted that in real experiments, except in some particular cases, the measured intensity is always a mixture of coherent and incoherent scattering contributions

$$I \propto \left(\frac{\partial^2 \sigma}{\partial \Omega \partial E} \right) = N \frac{k'}{k} \left(\frac{\sigma_{coh}}{4\pi} S_{coh}(q, \omega) + \frac{\sigma_{inc}}{4\pi} S_{inc}(q, \omega) \right). \quad (3.23)$$

Therefore, it is necessary to separate different contributions if one wants to monitor individual correlation functions. Estimation can be made for small momentum transfers where the coherent scattering contribution is small (see later according to equation 3.26) or for elements which scatter exclusively coherent/incoherent. In the intermediate q range a separation of the coherent/incoherent scattering contribution is not trivial without the knowledge of the exact form of the structure factor.

3.1.3 Neutron scattering on liquids and glasses

Liquids and glasses are systems characterized by lacking of long range orders. One does not find atoms at distinct lattice positions like in a single crystal but they are rather randomly distributed. For such isotropic scattering systems only the magnitudes of corresponding \vec{r} and \vec{q} vectors are relevant for the discussion. Therefore, in the following sections the vector forms are replaced by their amplitudes.

Static scattering

For static scattering the approximation is taken as that the time which the neutrons need to pass from one atom to the next is much smaller than the characteristic relaxation time of the scattering system, for example a neutron diffraction experiment conducted at low temperatures with a large enough incident neutron energy. Here the discussion will mainly focus on their connections to the time-of-flight experiment accessible quantities.

A static approximation corresponds to $t \rightarrow 0$ limit of the correlation functions. According to the density-density correlation function 3.19 this gives

$$G(r, 0) = \delta(r) + g(r), \quad G_s(r, 0) = \delta(r). \quad (3.24)$$

$g(r)$ is known as the static pair correlation function. As discussed before, since there is no distinct lattice position, the $g(r)$ of these systems is rather a continuous and smooth function with broad maxima (Fig.3.1). Thus in a diffraction experiment the selection rules according to Bragg condition $\vec{G} = \vec{q}$ do not apply where \vec{G} is the reciprocal lattice vector. There is no sharp Bragg reflection observable in the static structure factor $S(q)$ which is given by

$$S(q) = 1 + \int g(r) e^{iqr} dr. \quad (3.25)$$

Despite the short of long range order, in liquids and glasses there still exist characteristic length scales. For a coherent scatterer typical nearest neighbour distance is reflected in the structure factor at large scattering vector. In certain systems there are additional intermediate range orders due to either chemical interactions between different components (e.g.: in the liquid AlNi alloy [MPPC90]) or particular bonding distance in the system (e.g.: in amorphous SiO₂ [SVP⁺91, Ell91]).

For an one component, pure coherent scattering system in the limit of $q \rightarrow 0$ the static structure factor approaches the value $S(0)$ which can be estimated using the relation

$$S(0) = \rho N_A \kappa_T k_B T / M_A \quad (3.26)$$

where ρ is the number density and κ_T is the isothermal compressibility of the system at a given temperature. N_A denotes the Avogadro number and M_A is the atomic mass of the scatter. In the limit of $q \rightarrow \infty$ the structure factor approaches unity.

For multicomponent systems like silicate or metallic glasses and melts which are mixtures of various kinds of atoms with different coherent and incoherent scattering cross sections, the quantitative or even qualitative interpretation of the structure factor become more difficult. Nevertheless, the small and large q limit can be still discussed. For example, amorphous SiO₂ (silica) shows first maximum (FSDP: first sharp diffrac-

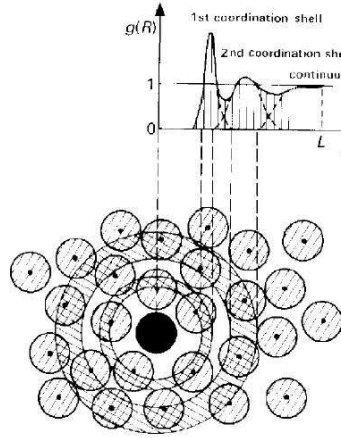


Figure 3.1: Pair correlation function $g(r)$ of a monoatomic liquid. Due to the disorder there is no discrete line but only the broad maxima in the $g(r)$. Nevertheless the first and second coordinate shells can be still clearly recognized which represent the short range order. After [Zol92].

tion peak) in the structure factor around 1.6 \AA^{-1} which represents the characteristic Si-O bonding distance. In a relative "simple" liquid like metallic melts the $S(q) \rightarrow 1$ limit can be observed already at the q range of about $10\text{--}12 \text{ \AA}^{-1}$. However, generally in oxide glasses and melts this does not apply up to $q=18 \text{ \AA}^{-1}$. Only for momentum transfers well above 20 \AA^{-1} the $S(q)$ approaches unity as seen in a recent neutron diffraction experiment [Pöh05].

Incoherent scattering gives only a q independent contribution to the scattering intensity which is normally observed in neutron diffraction experiments as a constant background. But for some systems like H rich samples or V, the incoherent scattering cross section is so large that the sample can be regarded as scatters only incoherently. Structural informations delivered by the coherent scattering can be completely masked by the incoherent intensity.

For neutron time-of-flight experiments the measured scattering function 3.10 is related with the static structure factor by

$$S(q) = \int_{-\infty}^{\infty} S(q, \omega) d\omega. \quad (3.27)$$

However, a direct access to $S(q)$ based on the measured double differential cross sections is not available due to two reasons. First, at elevated temperatures the Debye-Waller factors f_q differs from unity and of which the exact form is unknown. Second, kinematic restrictions on the experiment accessible momentum and energy transfer range do not allow a proper integral of $S(q, \omega)$.

The accessible quantity in the *ToF* experiments is the elastic structure factor $S_{el}(q)$ which is defined as the scattering function at zero energy transfer. In a real experiment the energy resolution of the instrument is finite. Thus, the elastic structure factor is

obtained via an integration of $S(q, \omega)$ over the instrument energy resolution function $R(q, \omega)$

$$S_{el}(q) = \int_{R(q, \omega)} S(q, \omega) d\omega. \quad (3.28)$$

The elastic structure factor is a good approximation of the static structure factor multiplied by the Debye-Waller factor

$$S_{el}(q) = f_q S(q). \quad (3.29)$$

Dynamic scattering

Liquid and glasses are isotropic systems of which the density can be assumed to be uniform for sufficient large length scale r . Thus, the long time limit $t \rightarrow \infty$ of the time dependent density-density correlation function is given by

$$G(r, \infty) = \rho_0 \quad (3.30a)$$

and its self part by

$$G_s(r, \infty) = \frac{\rho_0}{N} \quad (3.30b)$$

where ρ_0 is the particle number density of the scattering system. The long time limit of the self correlation function is effectively zero for large length scale since N becomes a large number.

The self part of the density correlation function $G_s(r, t)$ represents the self motion of a particular atom. It can be assumed to have a Gaussian form (Gaussian approximation)

$$G_s(r, t) = \frac{1}{(6\pi\langle r^2(t) \rangle)^{3/2}} e^{-\frac{3}{2} \frac{r^2}{\langle r^2(t) \rangle}} \quad (3.31)$$

and its time Fourier transformation - the intermediate scattering function - is an exponential like function

$$S_s(q, t) = e^{-\frac{3}{2} \langle r^2(t) \rangle}. \quad (3.32)$$

Characteristic relaxation time τ can be defined here for the exponential function decays to the value e^{-1} . The quantity $\langle r^2(t) \rangle = \langle [\vec{r}(t) - \vec{r}(0)]^2 \rangle$, where $\vec{r}(t)$ is the position of an atom at time t , is known as the mean square displacement of which its time dependence describes atomic motions.

The physical meaning of the density-density correlation function which represents the collective atomic motions is more difficult to understand. On the long time scale the correlation function of a simple liquid still follows an exponential decay but with a relaxation time related to the structure factor. This behaviour is observed already for

example in liquid Argon [DR65]. In glasses $\delta(w)$ like peak exist in the coherent dynamic scattering function corresponding to the quasi-equilibrium sites in the system.

In this work the studies are mainly focused on the time and length scales which are close to the typical τ s for structural relaxation and atomic transport in the silicate melts, corresponding to the elastic and quasielastic part of the dynamic scattering function measured in the neutron time-of-flight experiments. On much smaller time and length scales, atomic motion is governed by local vibrations. This will reduce the elastic and quasi-elastic scattering intensities by additional factors, known as Debye-Waller factor for a coherent scatterer and Lamb-Mössbauer factor for an incoherent scatterer. These intensities are then recovered in the inelastic part of the spectra represent phonon-like modes in liquids and glasses.

3.2 Diffusion

3.2.1 Diffusion in simple liquid

For simple monoatomic liquid on times and distances which are much larger than the local vibration of atoms, atomic motion is governed by diffusion processes via Brownian motion. Thus the mean square displacement shows linear time dependence. The basic equation for diffusion is the Fick's law

$$\frac{\partial C(\vec{r}, t)}{\partial t} = D \nabla^2 C(\vec{r}, t) \quad (3.33)$$

where $C(\vec{r}, t)$ is the concentration (volume number density) of the diffusing particles at the position \vec{r} at time t and D is the diffusion coefficient. For an isotropic diffusion all sites are equivalent and $C(\vec{r}, t)$ is nothing but the self-correlation function $G_s(r, t)$. It can be easily verified that the Gaussian approximation 3.31 is a solution of the Fick's law 3.33 with the Einstein relation

$$D_s t = \frac{1}{6} \langle r^2(t) \rangle. \quad (3.34)$$

The self part of intermediate scattering function hence exhibits a simple exponential decay

$$S_s(q, t) = e^{-(t/\tau(q))} = e^{-D_s q^2 t} \quad (3.35)$$

and its time Fourier transformation $S_s(q, \omega)$ is a Lorentzian function

$$S_s(q, \omega) = \frac{1}{\pi \hbar} \frac{D_s q^2}{D_s q^2 + \omega^2} \quad (3.36)$$

with the full width at half maximum (FWHM) increases linearly with q^2 . For long range translation diffusion corresponding to the $q \rightarrow 0$ limit the diffusion coefficient can be measured by

$$D_s = \frac{1}{2\pi\hbar} \frac{\Gamma_{S_s(q,\omega)}}{q^2} = \frac{1}{\tau q^2} \quad (3.37)$$

At very short length scale the atoms can be regarded as free flying particles having ballistic motion. It can be show further via the derivation of the velocity autocorrelation function [HM86] that in thermal equilibrium the time dependence of the mean square displacement is

$$\langle r^2(t) \rangle = \frac{3k_B T}{M_A} t^2. \quad (3.38)$$

Therefore, the FWHM of the measured scattering function is no longer proportional to q^2 . In the intermediate q range a cross over from a ballistic motion to a diffusive motion happens.

3.2.2 Hopping model and anomalous diffusion

The transport phenomena of mobile atoms in frozen media is often described by hopping like motions. A jump-diffusion model originally discussed by Chudley and Elliott [CE61] to describe such kind of motion in liquids proposes following hypotheses. The diffusing particle is assumed to resident at one site for a given time τ_0 . After this time, it jumps rapidly to another site, within a negligible jumping time. Based on such assumption, the diffusion equation can be written down as:

$$\frac{\partial}{\partial t} P(\vec{r}) = \frac{1}{n\tau} \sum_{\vec{l}_i} [P(\vec{r} + \vec{l}_i) - P(\vec{r})] \quad (3.39)$$

Where $P(\vec{r})$ is the probability of finding a particle at \vec{r} and it can jump to another site which is connected by a displacement vector \vec{l}_i . The jumping distance $|\vec{l}_i|$ is assumed to be much larger than the thermal vibration cloud created by the atom around its equilibrium position. As shown already in the last section, $P(\vec{r}, t)$ is equivalent to the self-correlation function $G_s(\vec{r}, t)$. Solving such differential equation with the boundary condition $G_s(\vec{r}, 0) = \delta(\vec{r})$ and performing a spatial and time Fourier transformation, one gets the neutron scattering function

$$S_s(\vec{q}, \omega) = \frac{1}{\pi} \frac{\Delta\omega(\vec{q})}{[\Delta\omega(\vec{q})]^2 + \omega^2} \quad (3.40)$$

by denoting

$$\Delta\omega(\vec{q}) = \frac{1}{n\tau} \sum_{\vec{l}_i} [1 - \exp(-i\vec{q} \cdot \vec{l}_i)]. \quad (3.41)$$

Note that the $\Delta\omega(\vec{q})$ function has a part which only depends for the scattering vector \vec{q} and a part which only depends on the hopping rate $\nu=1/\tau$. So it can be rewritten in the form of $\Delta\omega(\vec{q})=f(\vec{q})\nu$. The $f(\vec{q})$ is also known as Chudley-Elliott function.

This model has been applied to describe hydrogen diffusion in various metallic systems like Pd [RRGF72] as well as to charge transport phenomena in porous medium [BMK⁺95]. If a characteristic hopping length l is available for a particular system, for the $q \rightarrow 0$ limit a characteristic diffusion coefficient can be related to the resident time τ_0 and the hopping length l by

$$D_s \propto l^2/\tau_0. \quad (3.42)$$

The physical picture behind is that although on a small time and local length scale the motion of atoms are characterized by discrete steps, the mean square displacement still shows long time linear behaviour like it is in a Brownian motion.

However, even towards the long time limit, a diffusive behaviour is not necessarily always having a linear time dependence of the mean square displacement. Diffusive behaviours which deviates from Brownian motion are called anomalous diffusion, which shows the time dependence of the mean square displacement

$$\langle r^2(t) \rangle \propto t^\alpha \quad (3.43)$$

with the time exponent $\alpha \neq 1$.

Anomalous diffusion behaviours can be phenomenologically described by a generalized hopping diffusion model. Hopping can be regarded as thermally activated processes. The hopping rate ν depends on the energy barriers between different sites. If one assumes there exists a distribution of different energy barriers as well as relaxation times, the relaxation behaviour of the complete system is then a superposition of different elementary processes. The relaxation function is hence given by

$$S_s(q, t) = \int \varrho(\tau) e^{-(t/\tau(q))} d\tau = e^{-(t/\tau(q))^\beta} \quad (3.44)$$

which is well approximated by a stretched exponential function used frequently to fit experimental data. The energy distribution function $\varrho(\tau)$ can be then obtained by inverse Laplace transformation [LP90].

The exponent β here is not directly connected to the time exponent α in the time dependence of the mean square displacement equation 3.43. To illustrate more clearly the time exponent, it is necessary to look at the time dependent velocity autocorrelation

function. A theoretical approach in such framework, especially for disordered system, is the effective medium approximation (EMA). It uses the same model of a distribution of energy barriers. [SB91]. The theory generalizes the hopping rates ν to a frequency dependent one $\nu(\omega)$ which can be then solved via self consistent equations depending on the energy barrier distribution. At small q the limit a generalized diffusion coefficient can be related to the hopping rate via again the Einstein relation

$$D_s(\omega) = \frac{1}{6} \langle r^2 \rangle \nu(\omega) \quad (3.45)$$

and the long range diffusion coefficient is given by the $\omega \rightarrow 0$ limit. $D_s(\omega)$ is essentially the time Fourier transform of the velocity autocorrelation function. Thus, the time exponent is included by $D_s(\omega) \propto \omega^{1-\alpha}$. In the regime where $|w| \gg |f(q)\nu(\omega)|$, the scattering function can be reduced to

$$S_s(q, \omega) \propto \nu(\omega) / \omega^2 \quad (3.46)$$

EMA provides hence a description of the anomalous diffusion behaviour which can be used for the interpretation of neutron scattering data [SPSH90]: the high frequency wing of the $S(q, \omega)$ spectra shows an frequency dependence of $\omega^{-(1+\alpha)}$. Despite the wide spectrum of the activation energies and the anomaly of the diffusion behaviour, an Arrhenius law still holds for the temperature dependence of the relaxation time and the diffusion coefficient obtained in such approach.

The time exponent can be derived via fitting the $S(q, \omega)$ with a exponential function. However, a reliable fitting result can be only obtained by fitting at least two decades in the frequency range. Such condition is usually not fulfilled with a single time-of-flight experimental setup. Combination of different experiment results which covers a sufficient large time window is necessary in order to get a proper determination of the time exponent.

It should be pointed out here that such description of the anomalous diffusion is purely phenomenological. In some systems like hydrogen containing crystalline and amorphous metals, the energy barrier distribution can be modeled based on different neighbouring site pairs. But generally the anomalous diffusion behaviour can be also caused by interactions such as liquids near the glass transition [GS92] or diffusion on fractal topology [Hil99]. There is no general microscopic interpretation of anomalous diffusion as well as its time exponent in the description.

3.3 Mode coupling theory and the glass transition

Mode coupling theory provides universal quantities and predictions which describe the dynamics of viscous liquids and their relation to the structure. Especially it gives a general model for idealized glass transition which can be used to understand experimental data. Detailed summary of mode coupling theory can be found in [Göt91, GS92]. In the following section only a brief introduction of basic ideals and results will be presented.

3.3.1 Basic approach

Mode coupling theory uses the normalized density correlation function to describe the dynamics in liquids which is defined by

$$\Phi(q, t) = \frac{\langle \rho^*(q, t) | \rho(q, 0) \rangle}{\langle \rho^*(q, 0) | \rho(q, 0) \rangle} = S(q, t) / S(q). \quad (3.47)$$

The correlation functions can be obtained by solving the general Langevin equation of the Mori-Zwanzig projector formalism

$$\ddot{\Phi}(q, t) + \Omega_q^2 \Phi(q, t) + \nu \dot{\Phi}(q, t) + \Omega_q^2 \int_0^t m_q(t - t') \dot{\Phi}(q, t') dt' = 0. \quad (3.48)$$

In this differential equation the first three terms are similar to the equation of motion of a damped harmonic oscillator with a characteristic frequency Ω_q and a friction force $\nu \dot{\Phi}(q, t)$. The integral term describes the forces which are coupled with the velocity at an earlier time t' by the memory kernel $m_q(t)$. Thus, the state of the system at the time t is linked to its previous state at time t' .

Götze and coworkers used a microscopic approach in the mode coupling theory by expressing the memory kernel $m_q(t)$ in the terms of a Polynomial of coupling constants v_n and density correlators. The coupling constants v_n are determined by the static structure factors [Göt91] and depend on the external control parameters like temperature, packing fraction, interaction potentials, etc. A closed set of equations can be then formulated and the density correlators can be evaluated. Mode coupling theory uses only static structure factors as input, therefore the dynamics in the system is fully determined by its structure.

On the experimental side the number of studies on microscopic dynamics on the order of ps to ns timescales are growing very quickly in the recent years due to the development of neutron scattering techniques. In many experiments the dynamics of liquids close to their glass transitions has been shown to be in good agreement at least qualitatively with the predictions of mode coupling theory, e.g.: in molecular liquids

[TSW⁺98] and bulk metallic glass formers [MBS99]. A review on the comparisons between the mode coupling theory predictions and the experimental results as well as the discussion of the validity of the theory can be found in [Göt99].

3.3.2 Structural relaxation processes and scaling laws

Following the MCT prediction, the microscopic relaxation can be divided into three different regimes which has been discussed already in chapter 1. A schematic representation of these relaxation processes in viscous liquids is shown in Fig.3.2 which is expressed in the term of density correlation functions calculated by the mode coupling theory. At very short time where atomic vibrations are dominant, there is no differ-

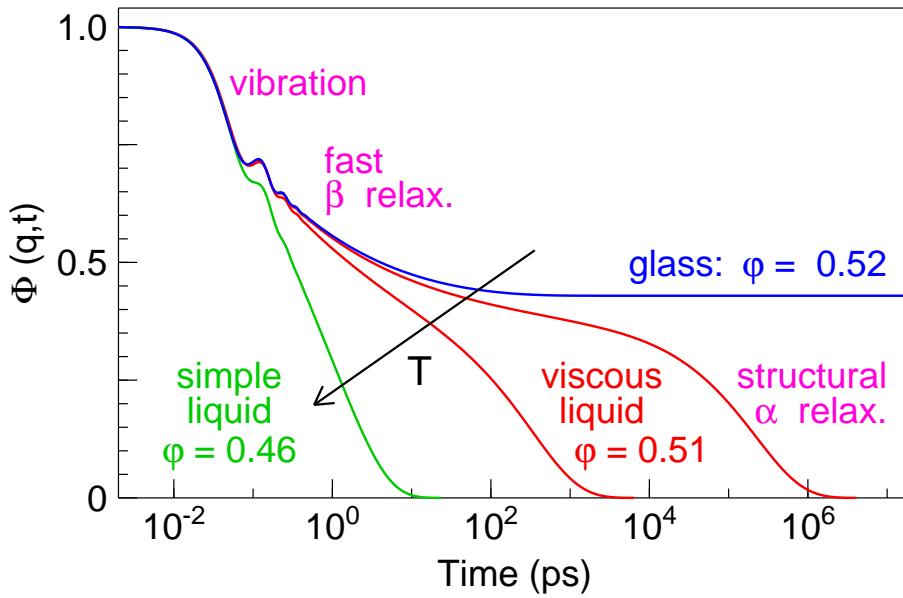


Figure 3.2: Schematic view of different relaxation processes in viscous liquids from the calculation of mode coupling theory. In simple liquid, the structural relaxation as represented by the density correlation function shows an exponential decay and has no β -relaxation process. The red curve shows the density correlation function in viscous liquids and the blue curve shows the idealized glassy state.

ence between simple liquids, viscous liquids and glasses. If one explores a bit longer timescale fast β -relaxation processes become involved and finally at long time the primary α -relaxation sets in. The α -relaxation becomes slower when the temperature decreases and it can be finally frozen in at certain temperature.

One remarkable feature of the mode coupling theory is that although the differential equations over the complete relaxation time window need to be solved numerically, within a finite time regime of a certain relaxation process, the correlation function can

be well described as a simple analytical function with some special properties. The density correlation function can be rewritten according to the theory into the form

$$\Phi(q, t) = f_q + h_q G(t). \quad (3.49)$$

Using such factorization, the correlation function is separated into two parts: the function $G(t)$ expresses the time dependence of the system and the other two factors f_q and h_q govern the q dependence.

The first factor f_q is the so called non-ergodicity parameter or plateau value and the factor h_q is the critical amplitude of the fast β process. The important factor for the structural relaxation and the glass transition is the non-ergodicity parameter f_q . In the liquid state the system is ergodic and the long time limit $t \rightarrow \infty$ of the density correlation function can fully decay to zero. When the temperature decreases below a critical temperature T_c the long time limit of the density correlation function jumps discontinuously from 0 to a non-zero value $0 < f_q < 1$ and $\Phi(q, t \rightarrow \infty) = f_q$. Thus, the critical temperature T_c is the liquid to glass transition temperature which is described in terms of mode coupling theory by a ergodic to non-ergodic transition. The idealized glass transition will be discussed in more detail in next section.

All of these factors shows certain scaling properties as functions of the temperature, or more precisely of the so called separation parameter σ which is a measure of how far the system is away from the critical temperature T_c , e.g.:

$$f_q(T) = f_q^c + h'_q \sqrt{\sigma} \quad (3.50)$$

where f_q^c is the value at the critical temperature.

According to the prediction of mode coupling theory, in the regime of α -relaxation the correlation function $\Phi(q, t)$ can be described by a stretched exponential function

$$\Phi(q, t) = f_q \exp[-(t/\tau_q)^{\beta_q}]. \quad (3.51)$$

The characteristic relaxation time τ_q exhibits as well scaling properties or the well-known time-temperature superposition principle:

$$\tau_q(T) \propto (T - T_c)^{-\gamma} \quad (T > T_c). \quad (3.52)$$

Thus, the correlation function of different temperatures can be scaled to one master function.

3.3.3 Schematic models of glass transition in MCT

It should be mentioned first that the glassy state described in mode coupling theory is an idealized state (the blue line in Fig.3.2). In the real system, even after the glass transition, the correlation function can still decay to zero based on hopping like motions, which is not included in the discussion of the mode coupling approach.

To discuss the qualitative features of the glass transition, mode coupling theory uses the so called schematic models. As discussed already in the last section, the memory kernel in the mode coupling theory is expressed in the terms of coupling constants and correlation functions. The coupling constants depend on the partial structure factors and interaction potentials of different particles in the system. Therefore, these quantities enter into the theory as external control parameters. The schematic models intend to observe under which conditions the glass transition happens. Therefore, the q dependence of the correlator is dropped for simplicity and the memory kernel is expressed by

$$m(t) = F(\mathbf{V}, \phi(t)), \quad F(\mathbf{V}, f) = \sum_{n=1}^N v_n f^n, \quad v_n \geq 0 \quad (3.53)$$

where $\mathbf{V} = (v_1, \dots, v_N)$ can be taken as a vector in the control parameter space. Thus, the schematic models deal essentially the dependence of the long time behaviour of the correlator on the control parameters \mathbf{V} .

At the glass transition where $\mathbf{V} = \mathbf{V}_c$ the resulting correlator changes its qualitative behaviour: the long time limit of the correlation function jump from 0 to a non-zero value. It could be shown that the solution shows singularities at these critical points, a phenomenon known as bifurcation. A glass transition diagram can be drawn from these critical values \mathbf{V}_c which form a surface (or a line in 2d) separating the liquid and glass state.

There are different schematic models depending on the expression of the memory kernel. The simplest model which can reproduce the dynamic feature near the glass transition is the F_{12} and F_{13} models, by using two coupling constants and writing down the polynomial F as

$$F_{12}(f) = v_1 f + v_2 f^2 \quad (3.54a)$$

$$F_{13}(f) = v_1 f + v_3 f^3. \quad (3.54b)$$

The former describes a structural glass transition (type-A glass) and the later is connected with a spin glass transition (type-B glass).

For multicomponent systems, it is often necessary to consider more than one correlator. A model introduced by Bosse and Krieger [KB87] uses two correlators and

expresses the memory kernel as

$$\begin{aligned} m_1(t) &= v_1 f_1^2 + v_2 f_2^2 \\ m_2(t) &= v_3 f_1 f_2 \end{aligned} \tag{3.55}$$

In the Bosse-Krieger mode, depending the position in the glass transition diagram, different dynamics feature can be obtained including for example a glass-glass transition with higher orders of singularities. It is hence quite useful to describe the dynamics in multicomponent systems close to the glass transition.

Chapter 4

Sample environment

In the chapter a detailed description of the high pressure high temperature sample environment is presented. The first section discusses some criteria which should be considered for a high temperature / pressure neutron scattering sample container. The construction of the cell is described in the second section. The characterization of the neutron scattering signals of the empty cell is shown in the last section.

4.1 Basic concepts

As already mentioned for the study of hydrous silicate melts with inelastic neutron scattering a sample environment which provides a temperature range up to 1500 K with a pressure up to several kbars and an available sample volume around 1 cm³ is necessary. The relative large sample volume is mainly due to the intensity requirement of a time-of-flight neutron spectroscopy. In this section some considerations for the design of the high temperature high pressure cell are presented.

4.1.1 High pressure high temperature vessel

One of the most widely used geometries for high pressure vessels is a thick-wall cylinder. However, in the following paragraphs it will be shown that even such a simple geometry needs a proper design in order to reach the maximum possible pressure for a certain material.

Dawson [Daw77] proposed a general calculation on cylindrical tube based pressure vessels. The basic mechanical model behind is a thick-wall tube under internal pressure. Therefore, according to the classical mechanics the general stress-strain equa-

tions can be easily written down as

$$\sigma_r = \frac{p}{\omega^2 - 1} \left(1 - \frac{b^2}{r^2}\right) \quad (4.1a)$$

$$\sigma_t = \frac{p}{\omega^2 - 1} \left(1 + \frac{b^2}{r^2}\right) \quad (4.1b)$$

$$\sigma_z = E\varepsilon_z + \frac{2\mu p}{\omega^2 - 1} \quad (4.1c)$$

where σ_r , σ_t and σ_z are the stresses in radial, tangential and longitudinal directions, respectively. b is the outer diameter of the pressure vessel. ω is the so called wall ratio, which is the ratio of the container outer diameter b to its inner diameter a , $\omega = b/a$ represents a measure of the wall thickness of the pressure vessel. E is the elastic constant of the vessel material and ε_z is the strain in longitudinal direction. Hook's law is hence included already in the equation. The Poisson's ratio of the material is denoted as μ . Boundary conditions are taken into account as such, that at the outer surface of the cylinder the pressure $P_0 = 0$ and inside the cylinder there is a uniform pressure $P_i = p$. For a closed-end cylinder the longitudinal stress is uniform (independent of z position) and can be rewritten as

$$\sigma_z = \frac{p}{\omega^2 - 1} = \frac{\sigma_r + \sigma_t}{2}. \quad (4.2)$$

According to the two equations it can be shown that the largest stress occur at the bore of the cylinder where $r = a$. The pressure vessel should be operated in the elastic regime. In real apparatus some safety margins should be taken into account as well. This means none of these maximum values should exceed the yield strength of the material. Thus according to the distortion energy theory one has

$$2Y_0 = (\sigma_t - \sigma_r)^2 + (\sigma_r - \sigma_z)^2 + (\sigma_z - \sigma_t)^2 \quad (4.3)$$

which leads readily to the maximum pressure can be held in the vessel

$$p = \frac{Y_0(\omega^2 - 1)}{\sqrt{3}\omega^2}, \quad p_{max} = \frac{Y_0}{\sqrt{3}} \approx 0.577Y_0 \quad (\omega \rightarrow \infty). \quad (4.4)$$

Y_0 is determined by the material used for the pressure vessel. The calculation clearly shows that a monobloc cylinder will only provide a maximum operation pressure less than 60% of the material strength. In order to increase the capability of the pressure vessel strengthening methods have to be applied.

There are various ways to strengthen pressure vessels. The general idea is to induce compressive residual stresses in the cell material to compensate the applied pres-

sure. One possibility is for example to shrink-fit two or more cylinders together where the outer diameter of the inner cylinders is slightly larger than the inner diameter of the outer ones. This method is used by Knorr *et al* [KAD99] on a high pressure cell for neutron diffraction applications.

Another possibility is called autofrettaging process which applies an over pressure to the cell which is larger than the maximum pressure will be held in the later operation, for example in the cell used by Sadykov *et al* [SGS95]. Essentially this creates a plastic deformed zone in the inner part of the cylinder and an elastic zone at the outer part of the cylinder. When the over pressure is released, there are residual stresses in the vessel materials which can compensate the applied "normal" operation pressures. It can be shown that effectively the autofrettaging process is equivalent to shrink-fitting infinite number of cylinders together.

Fig. 4.1 shows the calculation results of different strengthening methods as a func-

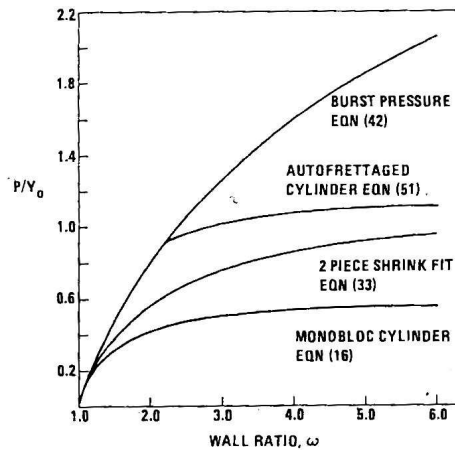


Figure 4.1: Strengthening effects as a function of wall ratio. Calculated for different strengthening methods. It is notable that the capability of a monobloc cylinder only reaches about half of the material strength. After [Daw77].

tion of the wall ratio. Two points should be mentioned according to this figure. First it can be seen that only by a proper design one can achieve nearly 100% of the material strength. Second it is worth to notice that about 80% of the cell capability can be already reached with a wall ratio of about 3. Thus, further increasing the wall thickness does not efficiently improve the performance of the pressure cell.

Autoclaves are pressure vessels subjected to high temperatures. One issue introduced by using the pressure vessel at elevated temperatures is the considerable thermal stresses which could build up during the heating and cooling procedures due to the temperature gradient. Another problem caused by the high pressure high temperature condition is creep of the materials. This is especially important for autoclaves strengthened by the autofrettaging process, since creep will lead to lose of the residual stresses. It is obvious that materials with a good creep resistance will be more favorable for autoclave vessels.

It is known that if the highest temperature imposed to the pressure vessel is at the inner surface, the induced thermal stress could actually increase the maximum pressure which the autoclave can hold. The situation is the inverse when the highest temperature is at the outer surface. Thus, internal heating is more favorable than external heating in the autoclave setup and is hence chosen in this work.

4.1.2 Materials

Since the maximum pressure in the high pressure vessel is directly determined by the strength of the material, the first requirement on the materials used is to have an adequate mechanical strength. For high temperature applications, further constraints of the high temperature strength must be considered. This excludes naturally low melting point materials like aluminum based alloys. Typical materials used for high temperature high pressure vessels are super alloys like Ni-, Co-, Fe based alloys and refractory metal classes like Nb, Mo, Ta, and W. For neutron scattering the container material should have smallest possible scattering and absorption cross sections and should not exhibit prompt activation by neutrons for radiation safety considerations. The neutron scattering cross sections of the elements which are involved in the alloys for high temperature applications are listed in Tab.4.1. For experiments with cold neutrons (wave-

Elements	σ_{coh} (barn)	σ_{inc} (barn)	σ_{abs} (barn)
Co	0.78	4.8	37.18
Fe	11.22	0.4	2.56
Ni	13.3	5.2	4.49
Nb	6.253	0.0024	1.15
Mo	5.67	0.04	2.48
Ta	6	0.01	20.6
W	2.97	1.63	18.3
Zr	6.44	0.02	0.185

Table 4.1: Neutron scattering and absorption cross section for different elements used in alloys for high temperature applications. The absorption cross section values are for thermal neutrons ($v \sim 2200$ m/s). For cold neutrons they are larger than the listed values.

length >4.8 Å), coherent scattering from simple cubic metal crystals are not excited. Thus, only the incoherent scattering and absorption are important. The incoherent scattering cross section of the materials are particularly important for the cell in this work since it will be used for quasielastic neutron scattering experiments. Referring to these cross sections good candidates are Niobium and Zirconium.

From the considerations of good neutron scattering properties as well as high temperature high pressure performance we decided to use Nb based materials for the pres-

sure cell. Nb has a slight higher melting point than Zr thus its high temperature performance is better, although the tensile strength at ambient temperature is bit lower compared to Zr. Furthermore, the incoherent scattering cross section of Nb is only 1/10 of the one of Zr. Another reason to choose Nb rather than Zr is that the commercial available grade of Zr or Zr based alloys usually contain up to 5% Hafnium which is an excellent neutron absorber [Neu06]. Since Hf nearly always presents in the Zr ore and due to their similar properties difficult to separate.

Nb based alloys are often used for aerospace applications where moderate strength is needed at high temperatures. Commercially there are pure Nb and several different classes of alloys available. A suitable alloy for the neutron experiment is Nb1Zr, a Nb alloy with 1 wt% Zr. Alloying 1% Zr improves the strength and high temperature performance, especially the creep resistance considerably compared to pure Nb. The yield strength and tensile strength varies from 138-255 MPa and 241-345 MPa, respectively [Dav90]. An example of the temperature dependence of the alloy strength of commercially available Nb/Nb1Zr products is shown in Fig.4.2. Both Nb and Nb1Zr have a

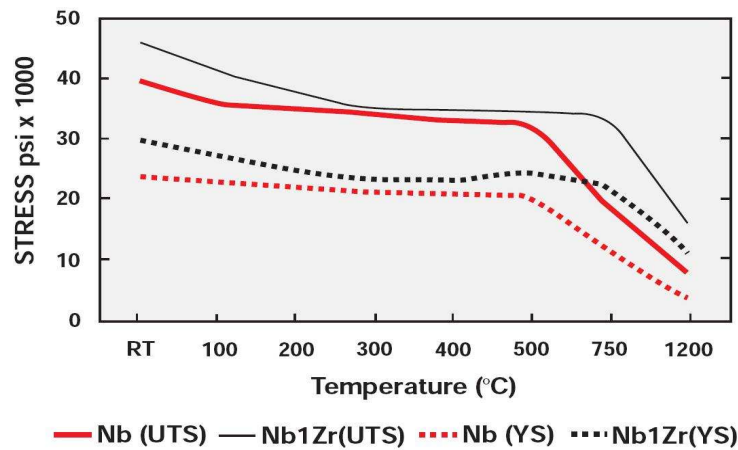


Figure 4.2: Temperature dependence of the yield strength (YS) and ultimate tensile strength (UTS) of the Nb and Nb1Zr alloy. Both materials show no significant strength decrease up to at least 500 °C. Source: Products data sheet, Cabot Supermetals Corporation.

good high temperature performance which can be seen clearly in the figure. Nb shows no significant strength drop up to a temperature of 500 °C. For Nb1Zr this range is even extended to 750 °C.

4.2 Construction and operation of the autoclave

The construction of the pressure cell are based on following considerations: A sample with a dimension around 40 mm long and 5 mm in diameter can be heated up to 1500

K under 200 MPa; A good neutron scattering characteristic and a geometry which fits the time-of-flight spectrometer TOFTOF.

4.2.1 High pressure components

The raw material was delivered in a form of a full cylinder with 40 mm in diameter and 1000 mm long. Four pressure cell were machined out from the raw material. The technical drawing of the cell is shown in Fig.4.3. From the figure it could be seen that

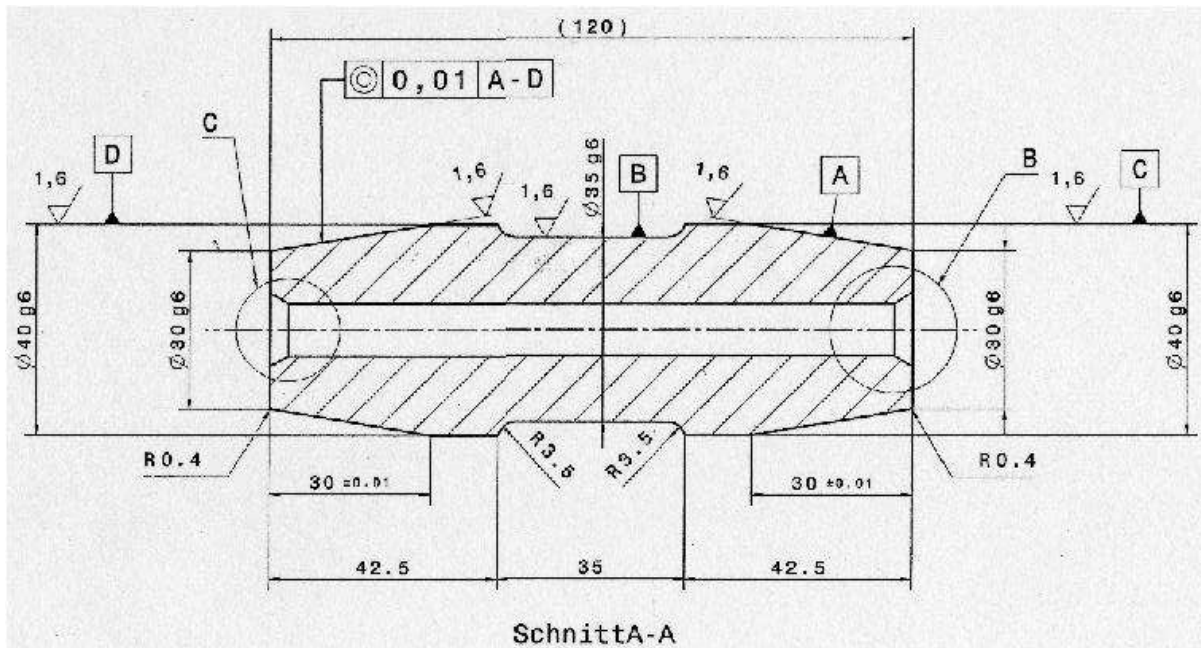


Figure 4.3: Technical drawing of the inner Nb1Zr cell. The dimensions of the cell are shown. The thinnest part of the cell is in the middle where the neutron beam passes through. The rest part of the cell is mostly assembled in a steel jacket. Sealing surfaces of the high pressure components can be seen as well at both end of the cell.

the Nb cell has a total length of 120 mm and an inner diameter of 10 mm. In the middle of the cell within a length of 35 mm the outer diameter was thinned down to 35 mm where the cell will be illuminated by the neutron beam. At the both ends of the cell the the outer diameter is gradually reduced from 40 mm to 30 mm within a length of 30 mm. The sealing surface of high pressure connection can be viewed as well.

The dimension of the cell is chosen as similar to a Nb cell which was used for neutron scattering under high pressure [FA02]. However, in order to test the neutron scattering properties of the cell an experiment with a dummy cell was performed on the TOFTOF spectrometer with the cell at ambient conditions. The results show a reasonable signal with the intensity of the sample together with the cell nearly an order of magnitude higher than the empty cell alone in the elastic region.

It is a natural logic that the cell is designed to have its minimum wall ratio at the part which is illuminated by the beam. However, outside the beam there is no constrain of the material on neutron scattering properties. Thus, high strength material like steel can be used and also with a larger thickness to improved the mechanical stability of the complete setup. Thus, the cell is enclosed in a steel jacket which makes complete setup more compact. Only one has to make sure that those part are not seen by the neutrons. Therefore, the inner surface of the steel jacket at the place close to the neutron beam is covered with Cd foil so that possible diffuse scattering events on the steel can be reduced. The Nb cell alone and the complete setup are shown in Fig.4.4.

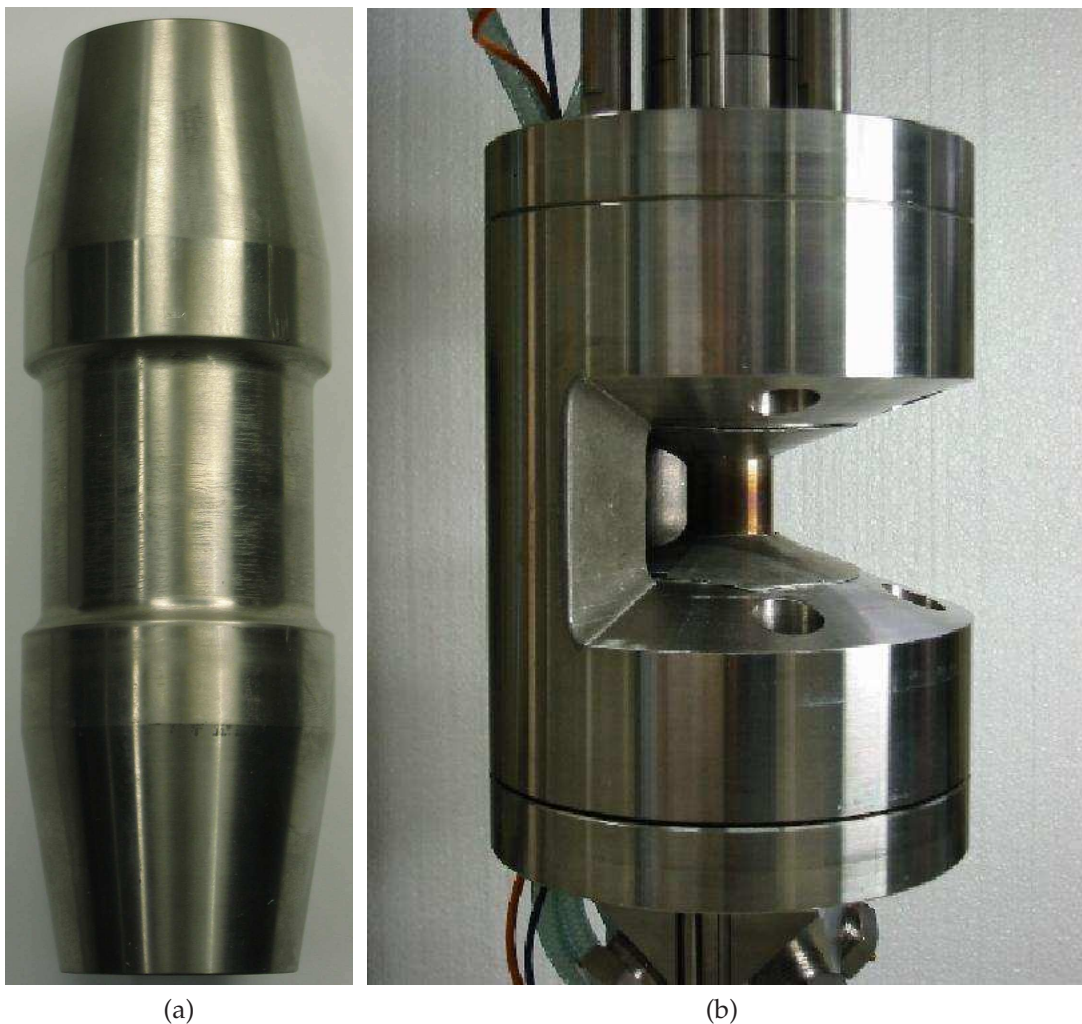


Figure 4.4: The high temperature / high pressure pressure cell for neutron scattering: a). The Nb cell itself b). The complete setup with the steel jacket and the high pressure connections. Close to the cell the steel parts are covered with Cd foils (partly removed here) in order to reduce the scattering on the steel.

It should be mentioned that the strength of the alloy depends largely on the man-

ufactory and processing procedures (for example whether it is recrystallized or cold rolled its strength can be highly different). Thus, no exact strength data is available when we brought the raw material from the supplier.

For safety reasons the cell has to be tested under pressure. A test on the cell with a larger inner diameter of 11 mm under a pressure of about 300 MPa was conducted. The test experiment was done by adapting the cell embedded in the steel jacket to the sample preparation pressure apparatus. The initial idea to enlarge the inner diameter was to perform a bursting experiment. If the bursting pressure of the cell with this dimension could be measured the one of the 10 mm inner diameter cell could be revealed via calculation.

However, it turned out that the cell can sustain a pressure of 300 MPa even with a inner diameter of 11 mm, which is the maximum pressure the compressor used for sample preparation can provide. The maximum pressure was charged four times with each time holding at the pressure for about 3 minutes before releasing. Since the cell with 11 mm inner diameter was not destroyed after the test experiment it is used for further development, although the bursting pressure of such geometry remains unknown. If one considers the tensile strength data in Fig.4.2 applying 300 MPa pressure should also act as an autofretting strengthening process for the cell to some extend.

In the neutron experiments a maximum pressure of 200 MPa was used, which is a factor of 1.5 smaller than the test pressure for safety margin. Besides the 300 MPa pressure test, a long time test which held the pressure of 200 MPa for 24 hours was performed as well. After these experiments no deformation was measured within a precision of about 0.1 mm.

4.2.2 High temperature furnace

The next step is to build a small furnace in the pressure cell which can heat up the sample. Several technical requirements should be taken into account. The furnace should have a good isolation from the cell. Thus, with a moderate power the desired sample temperature can be reached and the Nb cell itself also does not get too hot to lose its strength. The sample, furnace and cell should have a relative tight fit in order to reduce the gas pressure medium at the hot zone. This is mainly due to two intentions: 1) to reduced the background due to scattering on the pressure medium. 2) to limit strong convective gas flow which will leads a large temperature instability. Small gas volume is also favorable for safety issues.

The furnace is mainly composed of three parts. An ceramic tube with an outer diameter of 10.8 mm and a thickness of 1.5 mm serves as a thermal isolation of the furnace from the cell. Another thin ceramic tube with a inner diameter of 5.2 mm and a thickness of 0.8 mm was used to isolate the heating wire electrically from the Pt sample

capsules. Thus, no short circle of the heating element can happen. The tube is only 0.2 mm larger in diameter than the one of the sample to ensure a tight fitting. On the outer surface of this thin ceramic tube a thread was cut with a depth of 0.3 mm, a width of 0.6 mm and a slope of 1 mm for the mounting of the heating wires. Due to special dimensions of the ceramic parts they were machined at the crystal lab of the Physik-Department. To cut the thread on the thin ceramic tube a special tool was made in order to reduce the risk that the tube breaks during machining. Basically the thin tube was glued on a metal rod during cutting and removed afterwards. As heating wire PtRh alloy was used which has a higher electrical resistance than the pure Pt wires and therefore more electrical power can be loaded with the same current. The wire was first rolled into spring-like shape and recrystallized at 1100 °C to remove residual stress then mounted on the inner ceramic tube.

At the bottom of the furnace the heating wire was welded to a Pt tube with a outer diameter of 5 mm and a wall thickness of 0.2 mm which extends the wire outside of the Nb cell. The Pt tube is then connected to massive wires and eventually reaches the high pressure adaptor for external connections. The resistance of the Pt tube is negligible compared to the heating wire. At the top of the furnace the heating wire was welded to a Pt plate which acts as electrical contact for external connection. This connection is later on grounded to the steel part since it is fairly difficult to make another connection from the upper feed-through where the samples are introduced in.

The furnace has a heating zone of 70 mm in length which is about 35 mm longer than the length of the samples. At the bottom of the sample a thermal couple of Pt/Pt10%Rh is inserted into the furnace with a depth of about 15 mm to monitor the temperature below the sample. Samples are inserted from the top of the furnace with an additional thermal couple above the sample to monitor the sample temperature. During the experiment a temperature difference up to 200-300 °C between the upper and lower thermal couples could be built up depending on the pressure and temperature conditions.

In order to test the real temperature and the temperature homogeneity in the cell, a dummy sample (a 4 mm diameter ceramic rod) was inserted into the cell coated with a temperature indicating paint¹ and heated up to 977 °C (upper thermal couple reading) under a pressure of 200 MPa. The result is shown in Fig.4.5. The determined temperature from the paint is around 1000 °C, which is close to the indication of the upper thermal couple. However, due to the coarse temperature steps in the specification a precision smaller than ± 20 °C cannot be expected from such estimation. Nevertheless, it can be clearly seen that the temperature is relative homogeneous since the colour is nearly uniform. This is probably due to the factor that the gas convection in the cell is

¹Typ MC150-12 from Kager Industrieprodukte GmbH.



Figure 4.5: A dummy sample coated with temperature sensitive paint after heated up to 977 °C. It can be seen that the colour is relative uniform. According to the specification of the paint the temperature is of about 1000 °C, however with a large error bar of about ± 20 °C. Therefore, it is close to the upper thermal couple reading within the temperature instability.

still strong. However, this leads also the temperature stability not better than ± 10 -15 °C.

The two thermal couples were read out separately by two Eurotherm controllers 2132. Since the temperature reading of the upper thermal couple is closer to the real sample temperature the upper Eurotherm controller is used for temperature regulation via a solid state relay which controls the power suppliers. Typically an electrical power of 900-1200 W (18-20 A, 50-60 V) is needed depending on the target temperature and pressure conditions.

4.2.3 Other components and adaption to TOFTOF

Figure 4.6 shows the technical drawing of the complete cell. Several other components can be seen from the drawing. The Nb cell is water cooled during the experiment so that it does not get too hot to become soft. Two water cooling heads were in contact with the cell. Nearly the entire outer surface of the cell which is not in the beam is used as contact surface to ensure a good heat transfer. During the experiments the cooling heads are connected to the cooling water circle available at the FRM II.

The connection wires for top thermal couple are leaded out from the furnace to the top of the pressure apparatus. At the top of the apparatus a high pressure adapter provides the connections to the electronics and the high pressure gas line. The electronic wires can be then led out from the pressure cell via this high pressure adaptors.

A high pressure tube with an inner diameter of 10 mm and an outer diameter of 30 mm made out of steel is used to connect the NbZr cell to the high pressure adaptor, which can be also partly seen in Fig.4.6 as well as Fig.4.4. The sample mounted on the stick can be inserted into the furnace via this high pressure tube and reaches its final position. Thus, for changing samples only the adaptor need to be removed and the cell can remain in its position. One should note that the implementation of the high

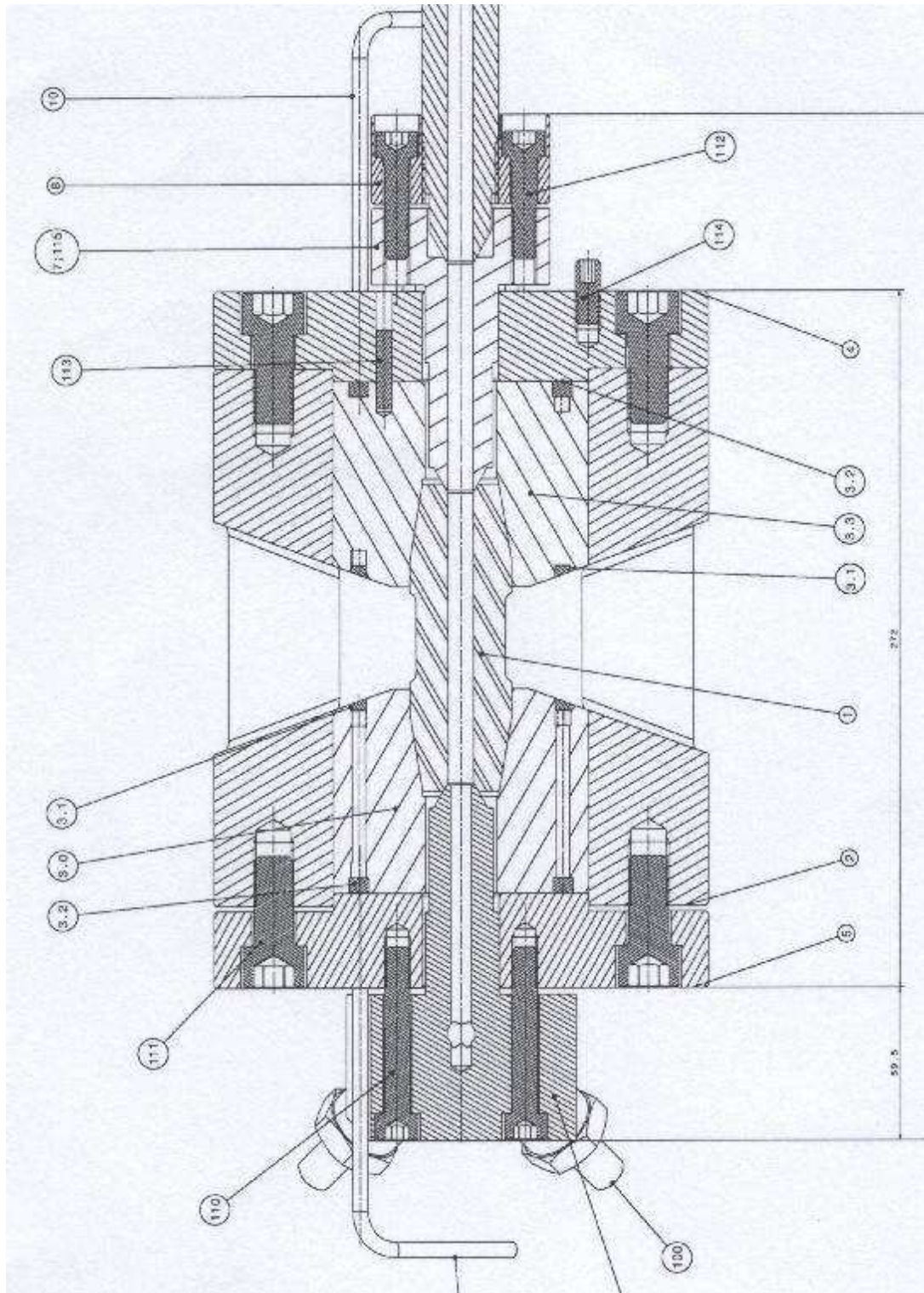


Figure 4.6: Technical drawing of the complete setup, including the Nb cell, the two water cooling head, the outer steel assembly and part of the connections for electrical wiring and gas medium at both ends of the cell. The two cones in the middle of the cell are designed for the entry and exit of incident and scattered neutrons, respectively. The overall dimension the the cell is around 190 mm in diameter and 270 mm in length.

pressure tube will increase the volume which is filled with the pressure medium of the system. This is not favorable from the safety consideration. However, the metal part of the sample stick will again fill this empty space so the volume of the gas medium is reduced to minimum. The sample stick acts also as an electrical contact to the platinum plate at the top of the furnace and then ground it to the steel part.

Prepared hydrous silicate samples were sealed in platinum capsules similar to the ones used for the sample preparation. This results in a sample dimension with 5 mm outer diameter and a length of 40 mm. The glass sample itself is normally smaller than the capsule with 3.5-4 mm in diameter and 25-30 mm in length. A platinum wire was welded to each capsule so that it can be bonded to the thermal couple capillary at the end of the stick as shown in Fig.4.7.



Figure 4.7: Mounting of the sample capsule. A Pt wire is attached to one end of the sample capsule and then bonded to the thermal couple capillary which can be seen in the upper half of the figure. The ceramic capillary extends to the cold part of the sample apparatus and is then connect to a metal tube which guides the wires to the top of the pressure apparatus.

The cell has a radial opening of 240° which allows neutron beam come in from one side of the opening, scattered on the cell and the sample and then reach the detectors at the most of the scattering angles available on the detector bank of the TOFTOF spectrometer.

The complete setup on the TOFTOF spectrometer is shown in Fig.4.8. Besides the pressure cell additional components are an aluminum protection tube and a flanch for the TOFTOF sample chamber, an aluminum plate standing on the flanch which the pressure cell is hanged on.

The aluminum tube has a outer diameter of 220 mm with a thickness of 8 mm in the region out of the beam and of 3 mm in the region which is in the beam. It serves as a final protection of spectrometer from the pressure cell in case of an explosion of the cell. Moreover, together with the flanch it closes the TOFTOF sample chamber so that the chamber can be filled with Argon gas during the measurements to reduced the background from the scattering on air.

Helium gas with a purity of at least 5.0 (99.999%) was used for neutron experiments as pressure medium which is provided by the high pressure gas line connecting the high pressure adaptor at the top of the cell to the compressor. For measuring D_2O

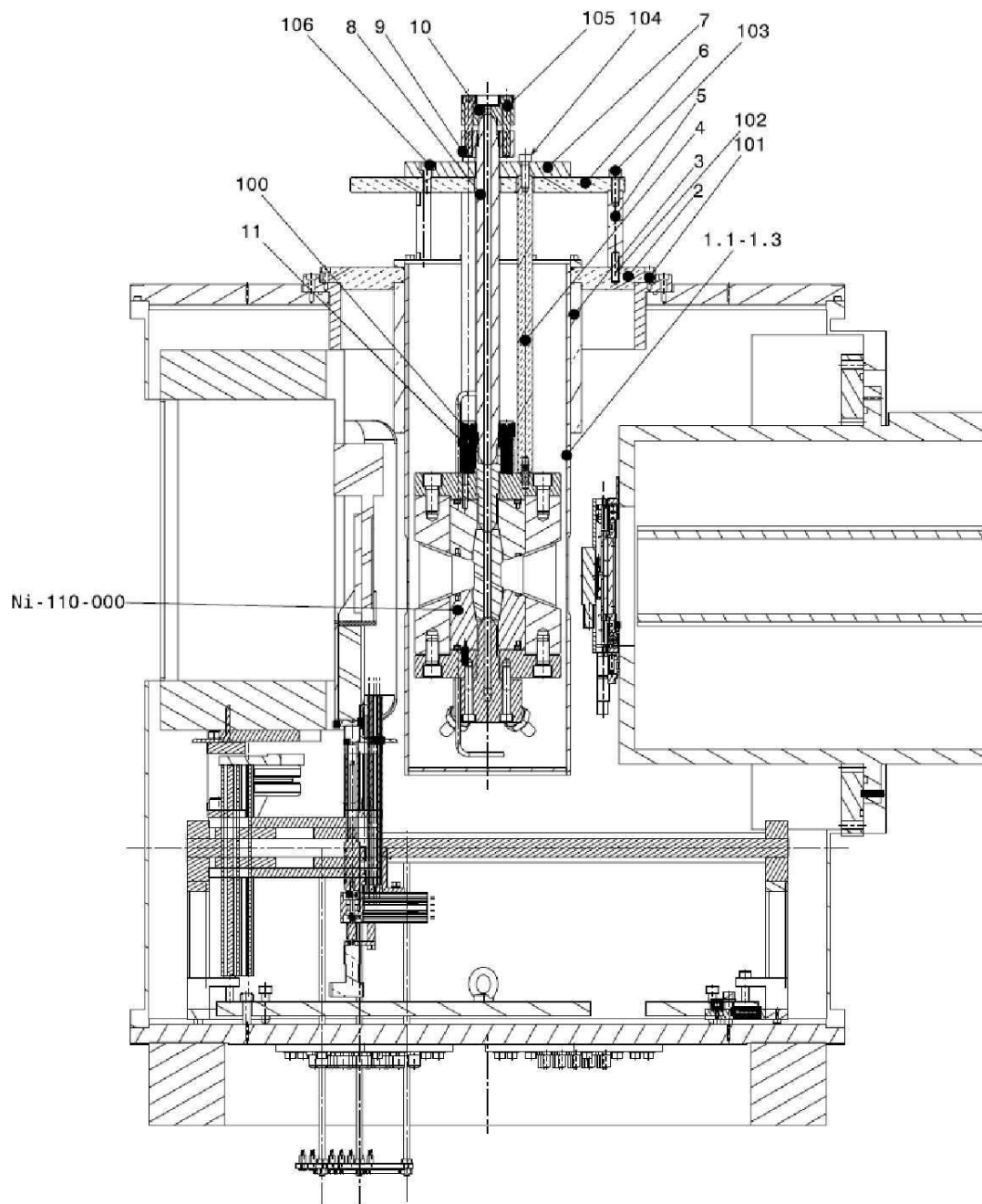


Figure 4.8: Schematic view of the complete setup on the TOFTOF spectrometer at FRM II. The neutron beam is coming from the right hand side of the pressure cell, part of the neutron guide was drawn. The pressure cell is surrounded by an aluminum tube. This aluminum tube also seals sample chamber of the spectrometer since it is filled with Ar gas during the measurement. The cell is hanged on an aluminum plate which is mount on the top of the sample chamber.

containing samples a higher purity of 6.0 is used in order to reduced the possibility that the deuterium is exchanged with hydrogen during the experiments. The gas compressor used for neutron scattering experiment is provided by the sample environment group of Forschungsneutronenquelle Heinz Meier-Leibnitz (FRM II). The compressor is supplied with He gas from a bottle with a pressure of 100-200 bar. A membrane compressor provides a pressure up to 100 MPa (1 kbar). With the combination of a pressure intensifier the compressor can work up to a maximum pressure of 1000 MPa (10 kbar). In order to prevent any over pressure building up in the cell a bursting disk with a limiting pressure of 2250 bar was assembled to the high pressure adapter.

The compressor is controlled via a computer which can regulate the pressure automatically. Therefore, in principle no over pressure could be built up beyond the set point. The actually situation in the experiments is the opposite. Due to the tiny gas volume inside the cell a small leakage will already lead to a drop of the pressure in the cell. In the experiment the pressure was losing due to the leakage of the cell and the compressor has to increase the pressure every 15-20 minutes during the experiment.

For the new sample environment safety check is required prior to the experiment, especially for the high pressure component. A proposal for applying the permission to operate the high pressure high temperature sample environment was submitted to the FRM II safety group and was granted at the beginning of our first beam time in June, 2007. Subsequently the pressure cell was accepted as a standard sample environment and a permanent allowance for the operation was received at the time of the second beam time in November, 2007.

4.3 Neutron scattering characteristics

During our first beam time, spectra of the empty cell were recorded under different conditions. In the empty cell measurements the aluminum protection shielding, the Nb cell and the high temperature furnace is in the beam. All the spectra shown below were measured using an instrument setup with an incoming neutron wavelength of 5.1 Å, a chopper speed at 12,000 rpm and a chopper ratio 3, which gives an energy resolution of about 90 μeV . A beam cross section of 9 mm wide and 22 mm high was used for all measurements. Note that in such experimental setup the cell is not complete illuminated by the beam. Only the part of the cell where the samples are placed is covered by the beam. Such beam dimension is chosen so that the scattering on the cell could be reduced and the signal-to-background ratio can be improved, which is especially necessary in the case of a weak quasielastic signal. However, partial coverage of the beam will lead additional complications for the background correction which will be discussed in more detail in the next chapter.

The measurement on the empty cell is to verify whether the high temperature background is acceptable and how the high pressure medium contributes to the signal. Therefore, spectra of the empty cell were recorded at different temperatures and pressures.

Fig.4.9 shows the measured intensity versus scattering angles of the cell at room

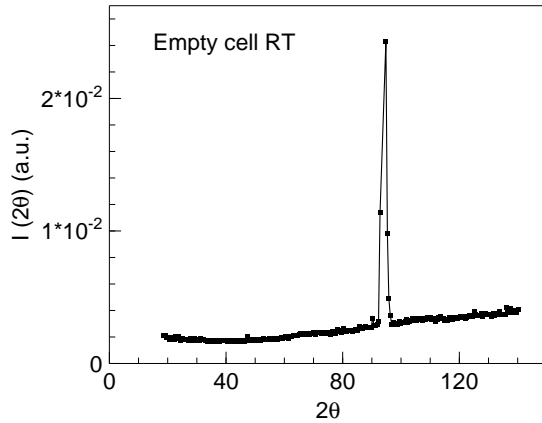


Figure 4.9: Measured intensity vs. scattering angle of the empty pressure cell at room temperature and ambient pressure. The Bragg peak from the Al_2O_3 ceramic parts in the cell can be seen. The flat intensity besides the Bragg peak increases towards large scattering angle due to increasing absorption by the massive pressure cell in forward scattering direction.

temperature and ambient pressure summed over all energy range. It can be seen that the cell delivers a fairly flat intensity over the complete scattering angles and a Bragg peak around 95° . As mentioned already the coherent scattering of the Nb cell is not excited since a wavelength larger than 4.8 \AA was used. This Bragg peak is arising from the aluminum oxide ceramics used for the furnace components. These scattering angles are excluded for further data analysis. What can be also observed is that the scattering intensity increase slightly towards higher scattering angles. This is mainly due to the massive Nb piece in the beam (a total thickness of 24 mm) which make forward scattering less probable than the scattering to large angles.

Fig.4.10a shows the measured spectra for the empty cell filled with He under different pressures at a temperature of 1250 K . With these measurements the influence of the pressure medium can be investigated. As it can be seen from the figure, the spectra of different pressures nearly fall on each other. This shows the background is independent of applied pressure. Therefore, later background measurements are carried out with a pressure of $150\text{-}200 \text{ bar}$, which is directly available from the He gas bottle. It can be also observed that no quasielastic broadening is present in the spectra. This indicates that the He gas used as pressure medium does not contribute significantly to the quasielastic signal.

Fig.4.10b shows the measured spectra for different temperatures under a constant pressure of about 400 bar . In the elastic region the spectra stays nearly unchanged for different high temperatures compared to the room temperature measurement, partic-

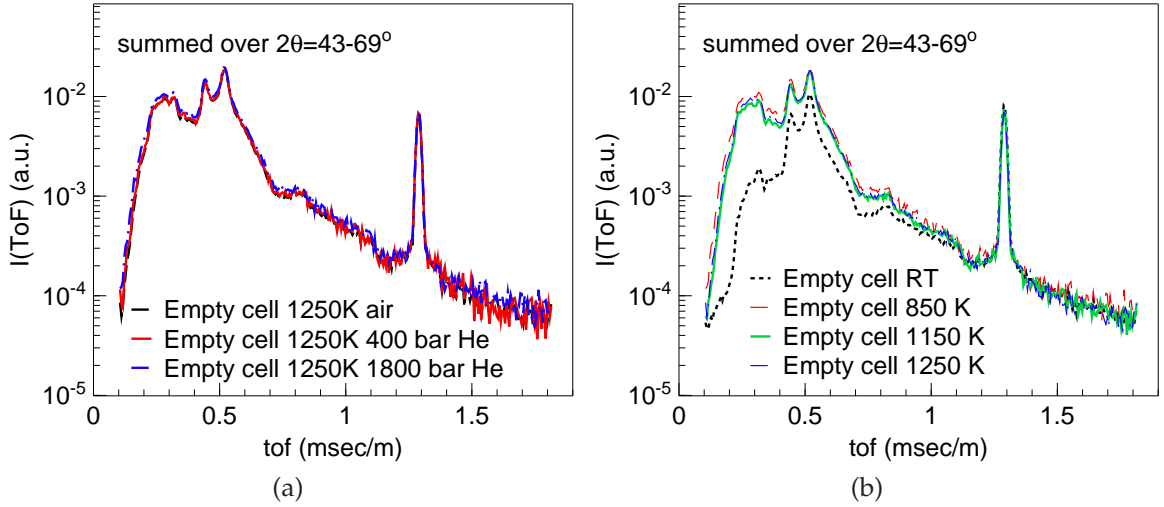


Figure 4.10: Measured spectra of the empty pressure cell under various pressure and temperature conditions. All spectra were summed over a scattering angle range of 43° - 69° , corresponding to the q values from 0.9 \AA^{-1} to 1.4 \AA^{-1} . a) Pressure dependence of the empty cell measurements at a temperature of 1250 K. b) Temperature dependence of empty cell measurements under a pressure of about 400 bar.

ularly no linewidth broadening can be identified. Hence, a good resolution for measuring a quasielastic signal from the samples can be obtained for the high temperature measurements. In the inelastic region the intensity increases with increasing temperature, which is due to the higher population of phonon levels in the Nb alloy since the cell itself also gets heated up during the measurement. However, after certain time a steady condition of the heat exchange process is reached and the inelastic spectra do not vary largely with respect to temperature.

Fig.4.11 shows the empty pressure cell measurements together with a NS3+10mol% H_2O sample at 1250 K under 1800 bar. It can be seen that the sample signal is well above the signal coming from the empty cell within the elastic and quasielastic region. The signal-to-background ratio is of about 10:1 in this region. The quasielastic broadening of the spectrum is dominantly contributed from the sample. In the deep inelastic region the intensity of the sample and the empty cell are rather close to each other. It will be difficult to get access to the inelastic spectra of the samples. It should be noted here that the spectrum of the empty cell at 1250 K and 1800 bar was recorded where the sample volume was completely occupied by He gas under such condition. The gas volume in the beam will be significantly reduced when there is a sample in the cell. The cell is hence not operated under the optimum conditions since a larger gas volume leads significant increase of the convection in the cell and a higher electrical power is needed in order to reach steady conditions. Even though no quasielastic contribution

from the empty cell was observed.

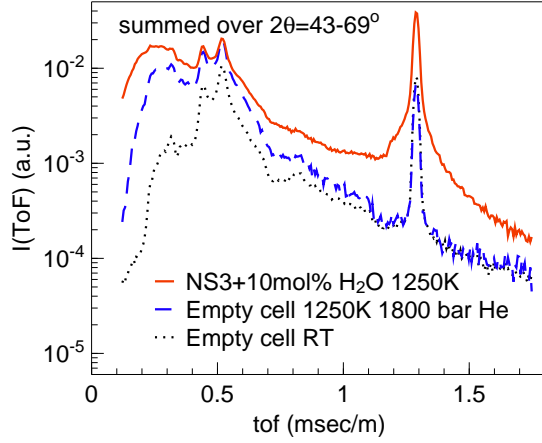


Figure 4.11: Measured $I(2\theta, ToF)$ of the empty pressure cell and a NS3+10mol% H_2O sample at 1250 K under 1800 bar. The quasielastic broadening arises dominantly from the sample. The signal-to-background ratio is of about 10:1 within the quasielastic region.

In conclusion from these measurements, the pressure cell constructed is suitable for quasielastic neutron scattering study under high temperatures and pressures. The sample environment provides a working temperature range from room temperature up to 1000 °C under a pressure of about 2 kbar. The cell delivers an acceptable signal-to-background ratio of about 10:1 within the elastic and quasielastic region. The contribution of He gas medium to the signal can be neglected, for both room temperature measurements and under high temperature/high pressure conditions. It will be difficult to extract inelastic spectra of the samples measured in such pressure cell due to the presence of the massive Nb cell in the beam.

Chapter 5

Neutron scattering experiment

The neutron experimental setup is described in the following chapter. The basic principle of neutron time-of-flight spectroscopy and the instrument setup used for the investigation of the hydrous silicate melts is presented. The data reduction processes are shown in the third section. Especially the problems caused by the massive pressure cell on signal correction are discussed. The last section presents the principle of the neutron backscattering experiments.

5.1 Time-of-flight spectroscopy

Neutron time-of-flight spectrometers are one major class of spectrometers for inelastic neutron scattering. In neutron time-of-flight spectroscopy the energy and momentum transfer of the scattered neutrons are determined simultaneously by measuring the neutron flight time from the sample position to the detectors and the scattering angles. Hence the dynamic scattering function $S(q, \omega)$ is measured directly in a broad range of q and ω .

The neutron time-of-flight experiments in this work were carried out exclusively at the TOFTOF spectrometer at FRM II. The schematic view of the instrument setup is shown in Fig.5.1. The instrument provides a high neutron flux ($\sim 10^{10}$ n/cm²/s, unperturbed) at the sample position accompanied with an excellent signal-to-background ratio [UMNP07]. A detailed description of the spectrometer could be found at [UNP07]. In the next paragraphs a brief introduction on the instrument setup will be presented.

The white neutron beam is delivered from the FRM II cold source operated with liquid D₂ at a temperature of 25 K. The white beam has a Maxwellian velocity distribution with a maximum located at the wavelength around 3 Å.

The TOFTOF spectrometer is a chopper time-of-flight spectrometer, the neutron beam is monochromated with a multi-disc chopper system which can be seen at the left side of Fig.5.1. The chopper disks are made of carbon-fiber-reinforced plastics coated

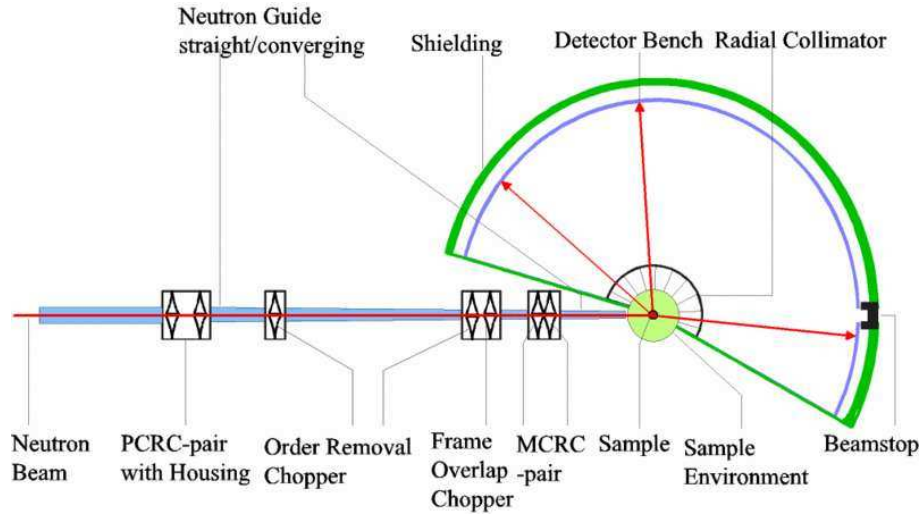


Figure 5.1: Schematic view of the instrument setup of the TOFTOF time-of-flight spectrometer at FRM II.

with ^{10}B as a neutron absorber. Thus, an optimum strength and weight is achieved which allows them to rotate at high frequencies in order to provide a good energy resolution. The chopper system cuts the continuous beam into pulses and selects one distinct neutron velocity out of the white pulses initially having a velocity distribution from the cold source.

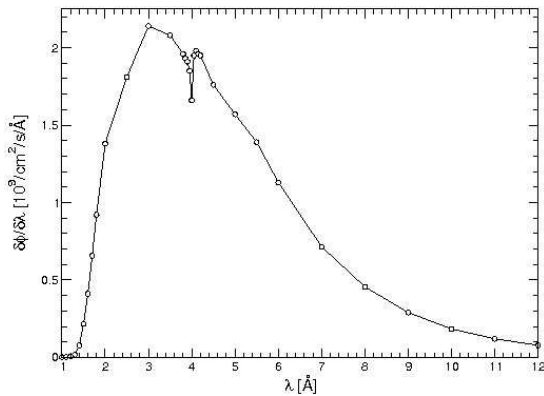


Figure 5.2: White beam flux at the sample position of TOFTOF spectrometer as a function of wavelength. The spectrum comes primarily from the Maxwell distribution of the velocity of neutrons moderated by the cold source of the FRM II which has a maximum located around 3 \AA corresponding to a temperature of 25 K.

The pulsed and monochromated beam are then guided to the sample position, scattered on the sample and the sample environment. The sample and the sample environment are sitting in the sample chamber which is filled with Ar during the measurement. Scattering on the air can be hence minimized. Directly after the sample and its environment, a radial collimator is mounted at the entrance of the flight chamber which is oscillating continuously around the sample. The radial collimator consists thin metal foils coated with Gd_2O_3 which are oriented radially to the sample. By this

way the sample environment can be mapped out and ideally only neutrons which are scattered on the sample can reach the detectors within an acceptance of about 10 cm diameter. However, this requires the sample to be positioned in the focus of the radial collimator. For the pressure cell this is defined by the flanch which closes the sample chamber.

The scattered neutrons the flight chamber will be detected at the end of the flight path by the detectors. The flight chamber is completely shielded with polyethylene and B_4C and filled with Ar gas as well, separated by a thin Al foil from the sample chamber. The detectors are mounted on the detector bank and with an equal distance of 4 m to the sample. Therefore, the energy of the detected neutrons is determined by the time which they need to pass this flight distance and reach the detectors after being scattered on the sample. This time normalized by the flight path gives the time-of-flight (ToF), which is the inverse of the neutron velocity in the unit of [ms/m]. According to the neutron velocity typical flight times are in the order of milliseconds.

When a pulse of neutrons arrives at the sample and its environment neutrons can be scattered either elastically or inelastically. Elastically scattered neutrons arrive at the detectors at a time determined by the incident neutron velocity and their flight path. Inelastically scattered neutrons can arrive either earlier or later, depending whether they gain or lose energy. Neutron pulses reach the sample with a finite time separation between each pulse and the detectors are counting continuously in time. Thus, if the time for the inelastically scattered neutrons to reach the detectors is longer than the time interval between two neutron pulses it will be counted among the neutrons of the next pulse. This problem is called frame overlap. It cannot be completely suppressed since the down scattered neutrons can be infinitely slow. A frame overlap chopper is used (see Fig.5.1) to remove a defined number of pulses. Thus, the time interval between two neutron pulses becomes larger and the frame overlapping is reduced. However, this is on the cost of reducing beam intensity. In the experiment often a compromise is used which allows the down scattered neutrons with wavelength larger than $f\lambda_i$ to overlap. f is called frame overlap ratio and λ_i is the wavelength of the incident neutrons.

An advantage of chopper disc time-of-flight spectrometer is that different incident neutron wavelengths and energy resolutions can be chosen by varying the phase difference between the choppers and the rotation frequency of the choppers according to the need of the experiment. For a given incident neutron wavelength the instrument energy resolution improves with increasing chopper frequency. For a given chopper frequency, increasing the incident neutron wavelength will also improve the energy resolution. However, one should keep in mind that both are at the expense of the neutron flux due to two reasons. First more neutrons are cut out by the choppers in order

to achieve a better energy resolution and the frame overlap ratio has to be increased as well since the neutrons are slower. Second due to the spectrum of the cold source, long wavelength neutrons are less available since they are on the tail of the spectrum (see Fig.5.2).



Figure 5.3: The detector bank of the TOFTOF spectrometer. The detector bank provides spaces for up to 1006 detectors. Currently 603 detectors are mounted on the rack.

The detector bank covers a scattering angle 2θ range of 7° to 140° which can be seen in Fig.5.3. The momentum transfer q it is related with the scattering angle at a fixed incident neutron wavelength by

$$q = \frac{4\pi}{\lambda_i} \sin\theta. \quad (5.1)$$

According to equation 3.1b and equation 3.5c the momentum and energy transfer are

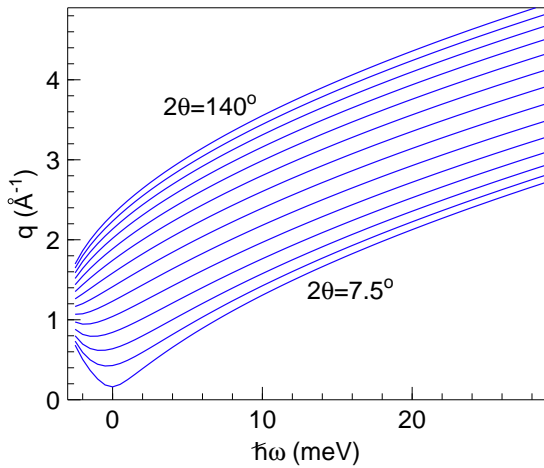


Figure 5.4: Accessible q - ω range of the TOFTOF spectrometer, calculated for incident neutron wavelength of 5.1 \AA , according to equation 5.2. The bottom curve stands for the smallest scattering angle of 7.5° and top curve stands for the highest scattering angle of 140° .

not two variables independent of each other. For a given incident neutron wavelength the accessible momentum and energy transfer on an instrument are limited by the

accessible scattering angles. We have following relation

$$q = \sqrt{\frac{2m_N}{\hbar^2}(2E_i \pm \hbar\omega - 2\sqrt{E_i(E_i \pm \hbar\omega)}\cos 2\theta)}. \quad (5.2)$$

The accessible q - ω range on TOFTOF for the incident neutron wavelength of 5.1 Å are represented in Fig.5.4.

5.2 Experimental setup

For most of the experiments performed in this work a neutron wavelength of 5.1 Å is chosen together with a chopper frequency of 12,000 rpm which is a good compromise between energy resolution and neutron flux. A frame overlap ratio 3 is chosen for this chopper frequency. The energy resolution of such experiment setup yields a value of (FWHM) about 90 μ eV.

For hydrous albite and pure silica samples another instrument configuration with a better resolution was used. An incident neutron wavelength of 6.5 Å together with a chopper frequency of 16,000 rpm and a frame overlap ratio of 4 delivers an energy resolution around 35 μ eV. However, the neutron flux is only of about 1/3 of the previous setup due to the refined resolution following the discussion in the last section.

The samples were measured at five different temperatures from 850 K to 1250 K. Room temperature measurements and measurements with Vanadium samples are taken as references. The empty Al protection tube was first mounted to close the TOFTOF sample chamber. Then the cell is built in. Samples were fully enclosed in Pt capsules. The sample is mounted on the sample stick and inserted from the top of the cell. After inserting the sample the cell was closed and connected to the gas compressor. The cell was first compressed to the target pressure of measurement, typically 180-190 MPa. Afterwards the samples were heated up slowly with a ramp rate of about 20-30 K/min. Cooling water is only switched on when the sample temperature is above 100 °C. Thus, condensed water in the cell can be avoided. Usually the sample was first heated to the highest target temperature and kept for about 20-30 minutes before the measurements start to make sure that it is melted and homogenous. A beam section of $w9 \text{ mm} \times h22 \text{ mm}$ was used and optimized in position in order to obtain the maximum sample signal.

Typical counting times for one temperature are 2-3 hours for samples containing H₂O and 8-10 hours for samples containing D₂O with the 5.1 Å incident neutron wavelength. However, samples can get crystallized for the low temperature measurements around 850 K. At this temperature the counting time is reduced down to 3 hours. D₂O containing samples were not measured at the highest temperature of 1250 K due to

a measurable exchange with the proton during the measurements (observation of increasing of counting rate with time) and samples were only measured at four different temperatures. For the measurements with 6.5 Å incident neutron wavelength the counting time is larger due to the reduction in neutron flux. It should be noted that due to the presence of the massive cell good statistics of the raw spectrum still does not necessarily indicate good statistics of the sample signal since the signal of the cell contributes substantially to the raw spectrum. After the measurement the sample was first heated above 900 °C for some minutes before cooling down rapidly below its glass transition temperature in order to prevent crystallization. After cooled down to room temperature the pressure was released gradually and the cell can be opened again for changing samples.

For both incident neutron wavelength the Bragg peak of the Nb1Zr cell is not excited. However, due to the presence of the ceramic components of the furnace the Bragg peak of the Al₂O₃ is excited and can be seen already in the empty cell measurements (see e.g.: Fig.4.9). This corresponds to the scattering angle range around 90.3°-96.8°. Consequently at the momentum transfer q around 1.7-1.8 Å the measured signals were cut out.

5.3 Reduction of neutron data

In this section the reduction of raw neutron scattering data is presented. For the data reduction and analysis the FRIDA program [WK07] developed originally by Joachim Wuttke was used.

The raw data reduction includes normalization to a Vanadium standard, correction of detector efficiency (of the neutron wavelength), correction for self-absorption and interpolation to constant wavenumbers q .

The incident neutron beam is measured by a monitor which gives the monitor counting rate

$$R_M = P_M A_M \Phi_i \quad (5.3)$$

where P_M is detector efficiency of monitor for a given incident neutron wavelength. A_M is the detection area of the monitor and Φ_i is the incoming neutron flux. The number of the counted scattered neutrons on the sample and its container which is detected within a solid angle $\Delta\Omega$ and the time interval Δt is given by

$$N_{SC} = P(2\theta)P(\lambda)A_{SC}\Phi_i I_{SC}(2\theta, ToF)\Delta t\Delta\Omega. \quad (5.4)$$

$P(2\theta)$ is the detection probability of the neutron as a function of the scattering angle, which represents the difference in detection efficiency between different detectors.

$P(\lambda)$ is the detection efficiency of different neutron wavelengths. A_{SC} is the area of the samples illuminated by the beam. Normalizing the counted neutron number N_{SC} by the monitor counting rate leads the counts to be independent of the incident neutron flux.

Normalization to an incoherent scattering standard gives the scattered neutron intensity on an absolute scale independent of the detection time interval and detection probabilities. This is typically done with a Vanadium standard. Vanadium can be considered as a pure incoherent scatterer. Only the intensities of the elastically scattered neutrons from the Vanadium sample are taken for the normalization

$$N_V = P(2\theta)P(\lambda_{el})A_V\Phi_i I_V(2\theta)\Delta\Omega. \quad (5.5)$$

which is then corrected with the Debye-Waller factor of the Vanadium calculated at the measurement temperature. After normalized to the Vanadium intensity the scattering intensity can be obtained by

$$I_{SIG}(2\theta, ToF) = \frac{N_{SC}}{N_V} \frac{P(\lambda_{el})}{P(\lambda)} \frac{A_V}{A_{SC}} \frac{I_V(2\theta)}{\Delta t} \quad (5.6)$$

The time-of-flight ToF represents the energy of the neutrons. It can be related to the energy transfer $\hbar\omega$ by

$$\hbar\omega = \frac{1}{2}m_N[(1/ToF_{el})^2 - (1/ToF)^2]. \quad (5.7)$$

Thus, the double differential scattering cross section can be represented in terms of the neutron flight time given by

$$\frac{\partial^2 \sigma}{\partial \Omega \partial \omega} = \frac{\partial^2 \sigma}{\partial \Omega \partial ToF} \frac{\partial ToF}{\partial \omega} = \frac{\partial^2 \sigma}{\partial \Omega \partial ToF} \frac{\hbar ToF^3}{m_N}. \quad (5.8)$$

The measured intensity is proportional to the double differential scattering cross section

$$\frac{\partial^2 \sigma}{\partial \Omega \partial \omega} \propto \frac{k_f}{k_i} S_{SIG}(2\theta, \omega); \quad \frac{\partial^2 \sigma}{\partial \Omega \partial ToF} \propto I_{SIG}(2\theta, ToF) \quad (5.9)$$

and by inserting equation 5.8 the measured intensity can be converted from ToF to energy ω using

$$S_{SIG}(2\theta, \omega) = A \frac{k_i}{k_f} \frac{\hbar ToF^3}{m_N} I_{SIG}(2\theta, ToF) \quad (5.10)$$

The prefactor A is related with the number density of the scatterers, the flight path of the neutron (scattering geometry) in the sample and the Vanadium. The final neutron wavenumber k_f also depends on the ToF which leads a ToF^4 dependence of the

scattering intensity on the neutron time-of-flight spectra. In order to obtain the correct scattering intensity S_{SIG} the detector efficiency for different neutron wavelength should be taken into account as well.

The measured intensity in a neutron scattering experiment is contributed from the sample (S_S) and the pressure cell (S_C), which are not additive. A simple subtraction of the scattering signal of the empty cell from the one of the sample with the cell (S_{SC}) is not possible. Necessary corrections from the calculation of Paalman and Pings for cylindrical sample geometry is used here to take into account the loss of the intensity due to absorption [PP62]. Different correction factors are used which are functions of the scattering angle and the neutron energy transfer. The correction factor $A_{S,SC}$ counts for the intensity loss of the neutrons which are scattered on the sample and absorbed by either the sample or its container. $A_{C,SC}$ counts for the intensity loss of the neutrons which are scattered on the container and absorbed by either the sample or the container. $A_{C,C}$ takes account for the intensity loss which is only from the container. These factors are calculated using the absorption cross sections of the sample and the cell and an optical path length (depends on the sample geometry) of the incoming and scattered neutron beam. The factors $A_{C,SC}$ and $A_{C,C}$ are often grouped into one factor $A_{rel} = \frac{A_{C,SC}}{A_{C,C}}$ since they correct the scattering from the container.

The normalization and background subtraction are done within the FRIDA program. However, several points should be noted due to presence of the massive pressure cell which leads the resulting intensity cannot be compared with the measurements results obtained with a standard sample environment on an absolute scale.

The Paalmann and Pings calculation can be further developed for partial beam coverage. These calculations are all based on a homogenous beam profile which is presented at TOFTOF. The advantage of these formalisms is that the correction factors can be expressed in terms of analytical functions. However, due to the complex structure of sample environment (aluminum protection, cell, ceramic furnace, sample capsule) and the partial beam coverage these calculations only provide an approximation. The exact value of these factors can be only deduced with numerical methods like for example Monto-Carlo simulations [BBTC91]. Thus the calculation done by the FRIDA program only gives an estimation of these factors.

In order to perform the calculation, the knowledge of cell transmission, scatterer number density of the sample and the scattering and absorption cross sections are necessary. The exact values of the first two quantities are unknown. The absorptance of the cell needs to be measured under a transmission geometry which is not available on the TOFTOF spectrometer. The transmission of the cell is taken from a Nb cell with a similar amount of Nb material in the beam [FA02]. The number density of the sample need to be calculated with the knowledge of the density of the samples.

However, most of the density data is available only for the samples in the glassy state. So far there is rarely any density data of the melt since they need to be measured under high pressure. The number density of the scatterer are estimated from the amount of the sample which is filled into the capsule and assuming it occupies of the volume of which the sample has after the measurements. The estimated scatterer density is closed to the one estimated using the sample density of the glassy state. H_2O and D_2O samples are assumed to have the same number density of scatterers since the area which is illuminated by the beam is completely filled by the samples.

The sample signals were normalized to a Vanadium signal obtained by direct subtracting the empty cell intensity from Vanadium intensity measured with the pressure cell. This is not a problem with the standard sample environment. However, the self absorption correction of the Vanadium signal which is not performed during the normalization cannot be neglected due to the strong absorption on the massive cell. The incoherent scattering nature of the Vanadium signal is not changed but its intensity is not on a correct absolute scale.

To summerize, these uncertainties should only scales the sample signals with additional prefactors. However, these factors are the same for all of the sample signals and the relative scale between different sample signals are not affected. Moreover the relaxation behaviour of the signals are not changed either.

The calculated correction factors are shown in Fig.5.5 for the H_2O containing samples. It could be seen that both correction factors are fairly independent of the energy

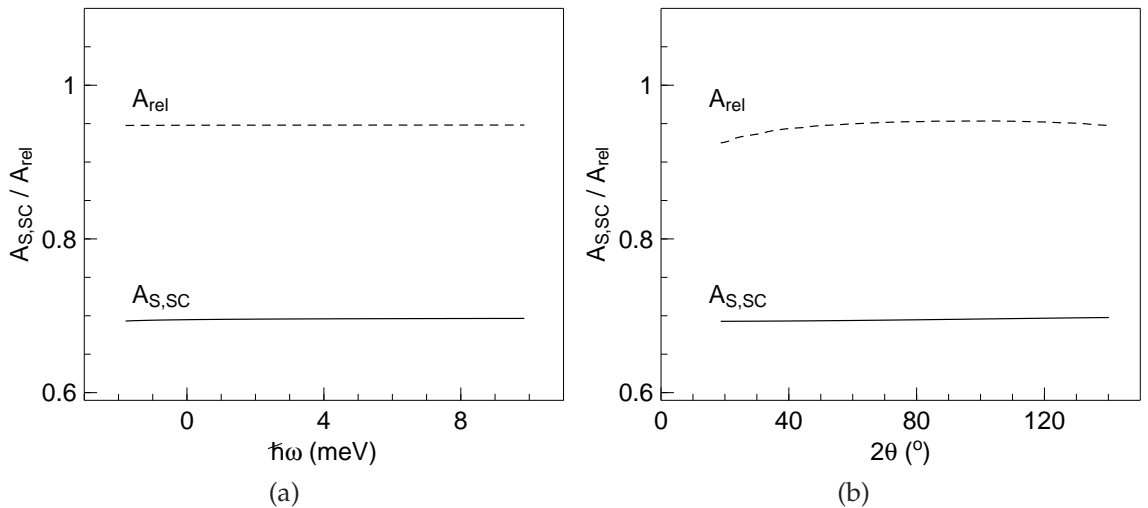


Figure 5.5: Self absorption correction factors for a NS3 sample with 10 mol% H_2O . The energy and scattering angle dependence of the correction factors are shown in a) and b), respectively. The correction factors for the container $A_{C,SC}$ and $A_{C,C}$ are grouped into one factor A_{rel} .

transfer and scattering angle. For H_2O samples the $A_{S,SC}$ is of about 0.7 which means

the signal of the sample is lowered by about 30% due to absorption. For D₂O samples this correction is smaller since the D₂O samples have less scattering power. The correction factor A_{rel} is located around 0.95 which is a rather small correction. At low neutron energy and small scattering the correction factor become smaller since the slow neutron are more probable to be absorbed and the path length of the neutrons are longer for forward scattering. The subtraction of background is done by applying:

$$S_S(2\theta, \omega) = S_{SC}(2\theta, \omega) \frac{1}{A_{S,SC}} - S_C(2\theta, \omega) \frac{A_{rel}}{A_{S,SC}}. \quad (5.11)$$

Multiple scattering effects are neglected since from the scatterer density and scattering cross sections of the sample the scattering power is estimated to be not larger than 8%. Furthermore, Pt used as sample capsule material is rather a strong neutron absorber.

The obtained sample signal after correction is related to the scattering function by a prefactor contains the scattering cross sections of different elements weighted by their relative abundance

$$S_S(2\theta, \omega) = \left(\sum_j f_j \sigma_j \right) AS(q, \omega). \quad (5.12)$$

For isotope substitution H₂O and D₂O containing samples of the same concentration were prepared for each silicate composition. Differential signal can be built by subtraction of the D₂O sample signal from the one of the H₂O containing sample. It can be easily verified according to equation 5.12 the prefactor for the differential signal contains only the scattering cross section of H and D since for other elements their scattering cross sections and abundance are identical and therefore canceled out during the subtraction. Thus one has

$$S_S^{diff}(2\theta, \omega) = f_H(\sigma_H - \sigma_D) AS_H(q, \omega) \quad (5.13)$$

Therefore, by building the differential signals pure information on hydrogen dynamics can be obtained. Moreover, owing to the huge incoherent scatter cross section of the H atoms (see Appendix A), the term $\sigma_H - \sigma_D$ can be approximated by σ_H^i and

$$S_S^{diff}(2\theta, \omega) = f_H \sigma_H^i AS_H^i(q, \omega) \quad (5.14)$$

nearly pure incoherent signal can be obtained.

Finally scattering intensity $S(q, \omega)$ is calculated by interpolation of the $S(2\theta, \omega)$ to constant wavenumbers q . After these correction the scattering function $S(q, \omega)$ is still convoluted with the instrument resolution function and it is not normalized by the sample scattering cross sections. Thus, the $S(q, \omega)$ obtained here for further discussion

are weighted by the scattering cross sections.

There are two ways to analyze the data, either in the energy domain or in the time domain, both should give the same results. For energy domain analysis the fitting functions need be convoluted with the instrument resolution function. The instrument resolution function is measured with Vanadium standard and dry samples at room temperature. The instrument resolution function of the TOFTOF spectrometer can be well approximated by a Gaussian function [UNP07]. Therefore, the measured signal is fitted with a Gaussian function and the fitting result is used for further data analysis.

Another way to analysis the data is to perform a Fourier transformation of the scattering function $S(q, \omega)$ to obtain the intermediate scattering function $S(q, t)$. For

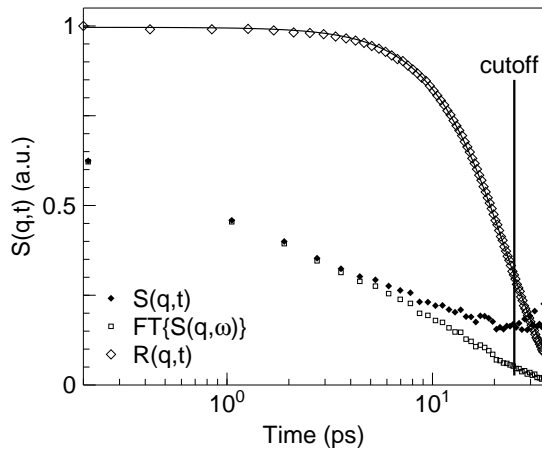


Figure 5.6: Deconvolution of the instrument resolution function $R(q, t)$ from the Fourier transformed scattering function $S(q, \omega)$ to obtain the intermediate scattering function $S(q, t)$. The instrument resolution function can be well approximated by a Gaussian function (thin solid line). The cutoff at large time is taken as the resolution function decays to about 30% of its initial value. This corresponds to a timescale up to 25 ps.

calculation of the Fourier transformation only data of $S(q, \omega)$ on the positive energy transfer side is used (neutron energy gain). However, due to the finite range of the energy transfer, a proper $t \rightarrow 0$ limit can not be obtained. For the resolution function the zero time limit is obtained by extrapolating the small time data to $t = 0$. Thus, the sample signal $S(q, t = 0)$ does not correspond to the static structure factor $S(q)$. After the Fourier transformation the sample signal is still convoluted with the instrument resolution function. The advantage of the time domain data analysis is that the deconvoluted signal can be obtained by a simple division of the sample signal by the instrument resolution, as shown in Fig.5.6. It could also be observed that the instrument resolution function can be well approximated by a Gaussian function. Therefore, for later data evaluation this Gaussian fitting for the instrument resolution function were used.

The cutoff at large times is taken where the resolution function decays to about 30% of its initial value, corresponding to a timescale up to 25 ps. For the time larger than the cutoff time the spectra are dominated by the instrument resolution function.

5.4 Neutron backscattering spectroscopy

Neutron backscattering spectroscopy measures the same physical quantity as in the neutron time-of-flight experiment: the scattering function $S(q, \omega)$, however with a significantly different energy transfer range. Typically neutron backscattering spectroscopy measures a dynamic range of maximum several tens of μeV with an energy resolution in the sub- μeV range. This give access to timescale up to the order of ns.

To achieve an energy resolution in the sub- μeV range neutron backscattering spectroscopy uses crystal Bragg reflection for both monochromatization and analyzation of the neutron energy. The Bragg reflection condition is given by

$$n\lambda = 2d\sin\theta. \quad (5.15)$$

The uncertainty or in other words the resolution can be easily shown by differentiating 5.15

$$\frac{\Delta\lambda}{\lambda} = \frac{\Delta d}{d} + \frac{\Delta\theta}{\tan\theta}. \quad (5.16)$$

According to this relation the uncertainty in crystal monochromatization is coming from two contributions: lattice misfit of the monochromator crystal Δd and the divergence in the neutron incident angle $\Delta\theta$.

Backscattering benefits from the fact that under the scattering angle $2\theta=180^\circ$ the angular contribution vanishes. Thus, the energy resolution $\Delta\lambda/\lambda$ reaches its minimum which only depends on the degree of lattice mismatch¹. Typically Silicon {111} lattice plane is used for monochromatization and under backscattering condition this results an incident neutron wavelength of 6.271 Å which fulfills the Bragg condition.

However, practically although under backscattering condition the neutron beam is perpendicular to the crystal Bragg plan, not all the neutrons in the beam will hit the plan at an angle of 90° since the neutron trajectories in a beam will never be all parallel. The $\Delta\theta$ in the incident angle does contributes to the wavelength uncertainty.

The scattered neutrons energies are analyzed in the same backscattering manner. In this sense a backscattering spectrometer is very similar to a triple-axis instrument. However, to cover an energy transfer range which is determined by how much the incident and scattering neutron energies are shifted to each other, it cannot be realized by varying the Bragg angle of the monochromator crystal like as it is done on the triple-axis spectrometer since this will destroy the excellent energy resolution. It can be only achieved using methods like continuous changing the monochromator d spacing by changing its temperature, or via a Doppler motion of the monochromator.

¹The $\Delta d/d$ value will never reaches zero even for a perfect crystal due to dynamical scattering, which defines a lower (theoretical) limit for the energy resolution of the backscattering technique, called Darwin width.

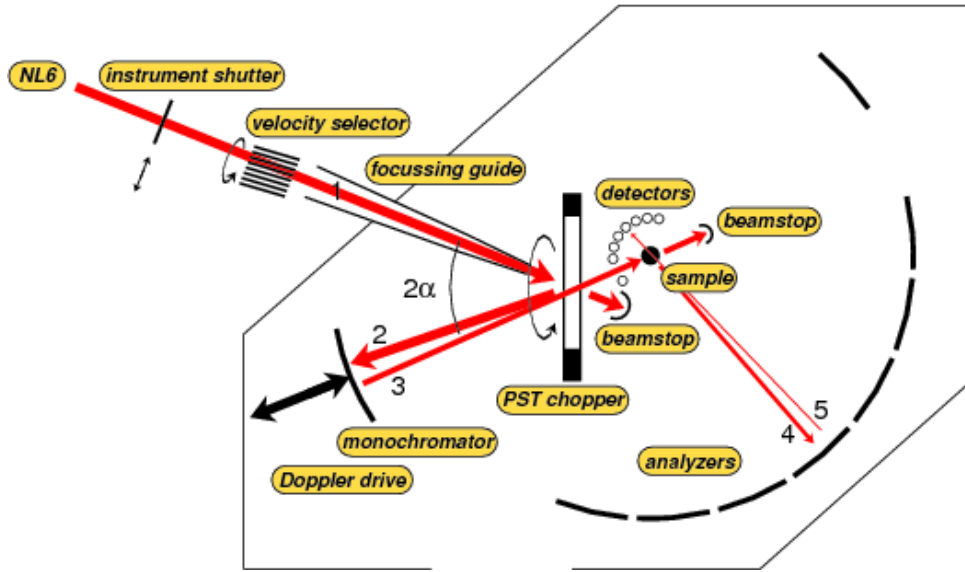


Figure 5.7: General layout of the SPHERES instrument. The main component of the spectrometer are a neutron velocity selector, a converging neutron guide, a PST chopper, a monochromator mounted on a Doppler driver, small and large angle analyzers and neutron detectors. The neutron pathways are briefly shown. It can be seen that the neutrons pass the sample twice before detection. from [Wut08].

Neutron backscattering spectroscopy is inherently an intensity limited technique due to its excellent energy resolution. The neutrons have to pass the sample twice before they are detected due to the backscattering geometry. Many efforts have been devoted to increase the neutron flux. The backscattering measurements in this work were performed at the spectrometer SPHERES from the Jülich center for neutron science at FRM II. SPHERES is a third-generation backscattering spectrometer. A major improvement of such kind of backscattering spectrometers is the use of a phase-space transformation (PST) chopper. The PST chopper shifts the incident neutron energy towards the wavelength which fulfills the Bragg condition of the monochromator crystal plane. Thus additional gain in the neutron flux can be achieved². A detailed description of the principle of such instrument can be found in [MDGN03] based on the high flux backscattering spectrometer HFBS at NIST Center for Neutron Research (Maryland, USA) which has almost the same layout. The instrument layout of the SPHERES spectrometer is shown in Fig.5.7.

The instrument has been realigned from its original setup for the high temperature high pressure experiments, mainly due to the fact that in the original setup the sample to detector distance is not enough to place the aluminum tube. Thus the sample

²However, the neutron flux gain is at the expense of larger beam divergence, which might increase the background.

to detector distance in our experiment is enlarged and the Si analyzers are adjusted accordingly.

However, the pressure cell is mainly designed for the TOFTOF spectrometer. The angular opening of the pressure cell only covers a range of 240° . Thus the small angle analyzer of the backscattering spectrometer cannot be used. The steel part of the cell was used as a beam stop which spans over 120° and the small angle analyzer is blocked. We used the Si 111 analyzer with an incident neutron wavelength of 6.271 \AA configuration. Mainly two Doppler driver speeds of 0.5 m/s and 0.3 m/s were used which provide dynamic ranges of $\pm 3.3 \text{ } \mu\text{eV}$ and $\pm 1.98 \text{ } \mu\text{eV}$, respectively. One hydrous sodium trisilicate sample was measured at two different temperatures. A temperature scan was performed as well, in which the Doppler driver speed was lowered down to 0.2 m/s .

Chapter 6

Dynamics in hydrous silicate melts

6.1 Dry sodium trisilicates

The instrument resolution of $90 \mu\text{eV}$ of the experimental setup using 5.1 \AA incident neutron wavelength on TOFTOF allows to measure a diffusion coefficient with a lower limit of the order of $10^{-10} \text{ m}^2\text{s}^{-1}$, estimated with the simple formula 3.37. Therefore,

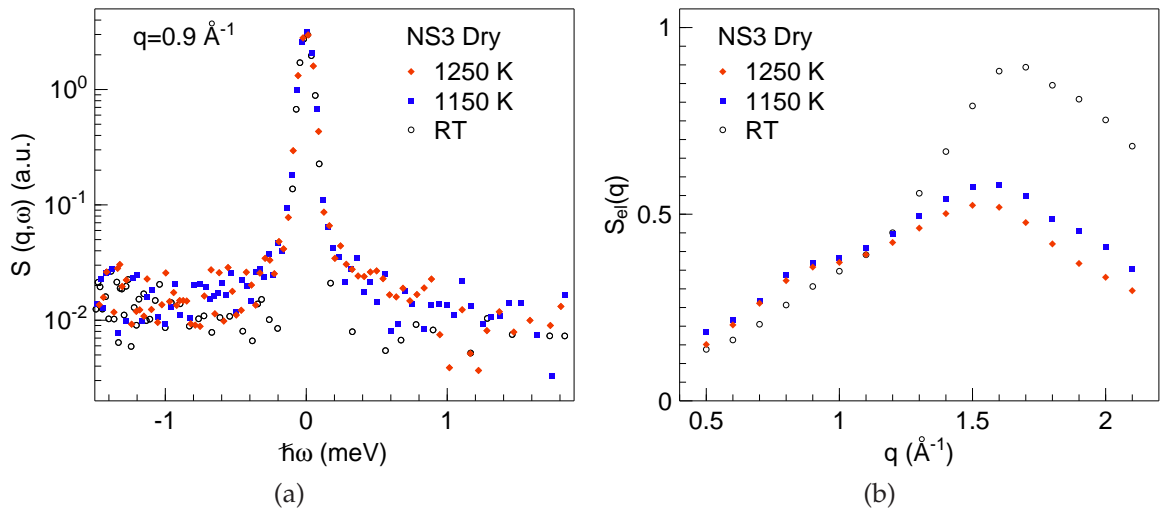


Figure 6.1: Measurements on the dry sodium trisilicate sample at room temperature, 1150 K and 1250 K within the pressure cell. a). Scattering function $S(q, \omega)$ at $q=0.9 \text{ \AA}^{-1}$, a small quasielastic broadening at elevated temperatures is visible compared to the room temperature measurement. b). Quasielastic structure factor calculated from an integration of the $S(q, \omega)$ over the energy range of $[-0.3, 0.3] \text{ meV}$. The arising of prepeak around 0.9 \AA^{-1} at high temperatures can be observed after the correction of the massive pressure cell background.

according to the data presented in Fig.1.2a sodium diffusion could also be observed at the temperature range of the measurements on TOFTOF, although the absolute amplitude (intensity) is rather low. This is confirmed with the measurement on the dry

sodium trisilicate melt within the pressure cell as shown in Fig.6.1.

The measurements were performed on a dry sodium trisilicate sample sealed in a Pt capsule with the pressure cell loaded with He gas bottle pressure around 150 bar. A small quasielastic signal is visible for the measurement at 1150 K and 1250 K compared to the room temperature measurement taken as a reference of the instrumental energy resolution. Only these two temperatures are measured since at even lower temperatures the sample crystallizes easily. Dry sodium trisilicate is a rather weak scattering system, the data presented here were counted on TOFTOF for at least 6 hours. Still at room temperature the signal is weak and the statistics is not very good after background subtraction. The quasielastic structure factor were calculated from the scattering function by integration over the energy range of $[-0.3, 0.3]$ meV. The prepeak feature at 0.9 \AA^{-1} representing the channel structure in the melt can be observed even with the measurement performed in the massive cell.

6.2 Hydrus sodium trisilicate melt

To study the hydrogen dynamics differential signals from H_2O and D_2O containing samples were built. Thus the quasielastic signal arises from the sodium diffusion does not contribute to the differential signal. The coherent scattering from the Si-O matrix can be subtracted and nearly pure incoherent signal from the H atoms can be obtained.

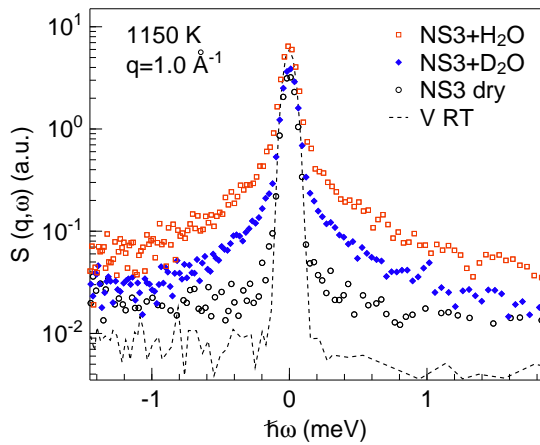


Figure 6.2: Different scattering functions measured on TOFTOF with 5.1 \AA incident neutron wavelength. Both H_2O and D_2O containing samples have 10 mol% water content. Vanadium spectrum at room temperature represents the instrumental resolution function. All silicate sample signals exhibit a quasielastic broadening.

Fig.6.2 shows different scattering functions measured at 1150 K. Sodium trisilicate samples with 10 mol% H_2O and D_2O samples are measured. The intensity of the H_2O containing sample is of about twice higher than the D_2O containing sample after the background subtraction which is in good agreement with the corresponding scattering cross sections. Thus a contrast variation is possible with a reasonable statistics. The linewidth of the dry sodium trisilicate spectrum is much smaller than the hydrous

samples. This is a first evidence that the dynamics in the water bearing melts are faster than the dry silicate melts. The D_2O signal has a smaller linewidth compared to the H_2O signal as well. However, this is only due to the scattering function of the fast proton dynamics is weighted by a much smaller incoherent scattering cross section.

6.2.1 Energy domain analysis

Contrast variation is performed for hydrous sodium trisilicate samples at 4 different temperatures from 850 K up to 1150 K. After performing the background correction, The scattering intensity $S(2\theta, \omega)$ from D_2O containing sample was subtracted from the one of the H_2O containing sample. From the resulting differetial intensity the scattering function $S(q, \omega)$ is calculated by extrapolation to constant q values. An interval of 0.2 \AA^{-1} is used for the extrapolation in order to improve the data statistics.

Fig.6.3 shows the differential signal $S(q, \omega)$ of sodium trisilicate sample with 10 mol% water content at different momentum transfers. Compared to the resolution

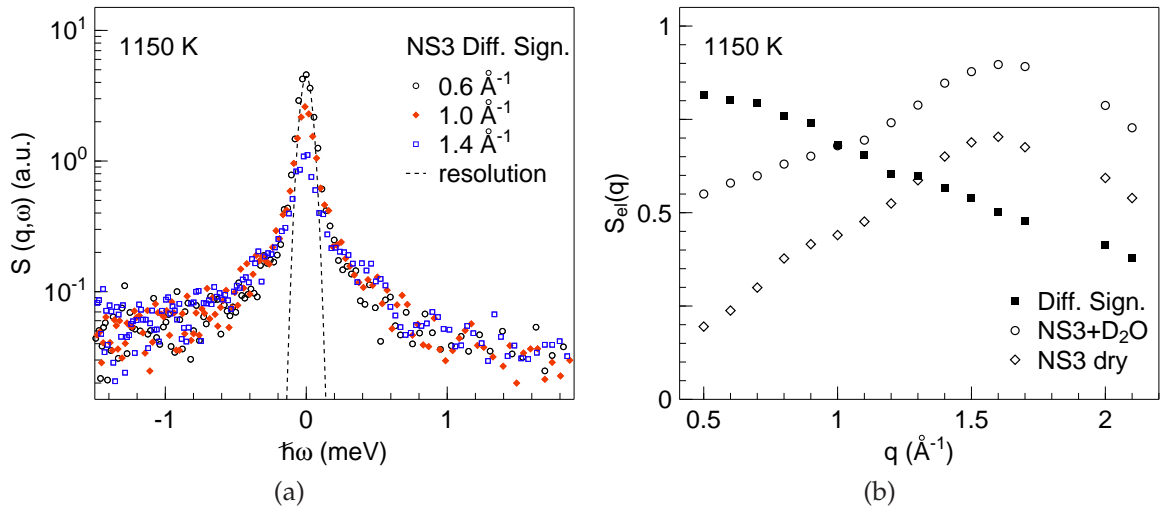


Figure 6.3: Contrast variation and the differential signal at 1150 K. a) Scattering function $S(q, \omega)$ at different momentum transfer. b) Quasielastic structure factor, intergrated over $[-2, 2]$ meV. The structure factor shows only a smooth decay, which is an indication of a pure incoherent scatterer, while the ones of the D_2O and dry samples all repret the melt structure.

funtion a quasielastic broadening is clearly visible. However, if one refers to simple diffusion behaviour a q^2 dependence of the linewidth would be expected. This is clearly not the case here since the linewidth of the signal does not show pronounced q dependence. The quasielastic structure factor was obtained by integration over an energy range of $[-2, 2]$ meV. The structure only shows a relative smooth decay, while for the D_2O containing and the dry samples they all show the q dependence which

represents the melt structure. This is an indication that the data correction procedure, especially the self-absorption correction does not change the relative scale between the signals of the H_2O containing sample and the D_2O containing samples. Otherwise it will show oscillation as a function of q since the structure factor of the D_2O signal would be weighted by a wrong value and will enter the signal. However, it should be noted that this quasielastic structure factor shows a quite strong decay as a function of q . It is not clear here whether this is due to a strong q dependent of the Debye-Waller factor or some other reasons.

Fig.6.4 shows the differential signal at two different momentum transfers of 1.0 \AA^{-1} and 1.4 \AA^{-1} at different temperatures. Both momentum transfers are below the first structure maximum of the sodium trisilicate melt (cf. Fig.6.1b). It could be seen that

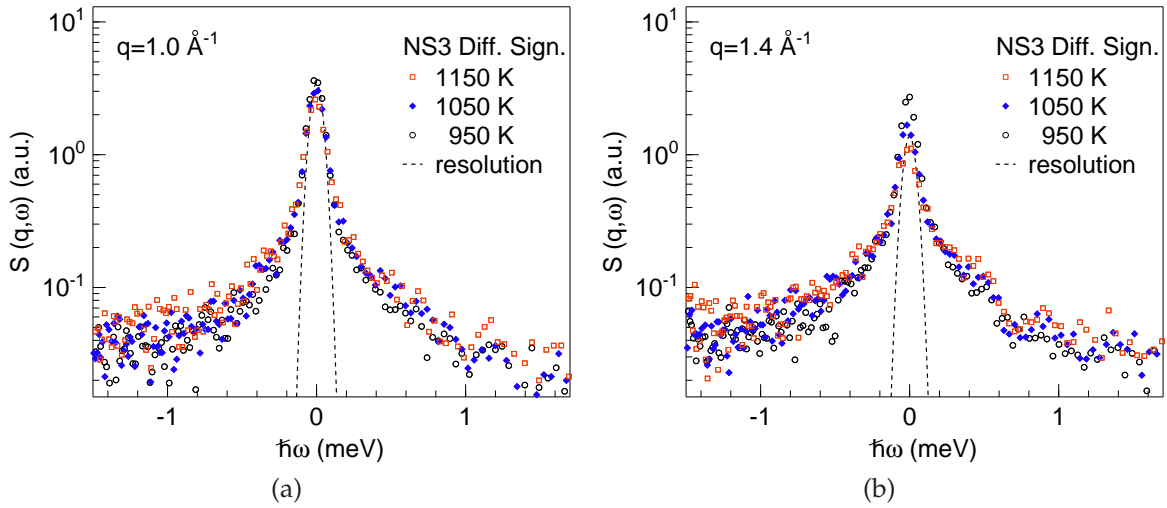


Figure 6.4: Measured scattering function $S(q, \omega)$ at different temperatures 950 K, 1050 K and 1150 K. Differential signals are presented. Only weak temperature dependence of the scattering function is observed for both momentum transfers: a) 1.0 \AA^{-1} . b) 1.4 \AA^{-1} .

at both momentum transfers the spectra are significantly broader than the instrument resolution function. However, the temperature dependence of the scattering function is rather weak. The linewidth of the scattering function only changes slightly, especially at small momentum transfer at 1.0 \AA^{-1} . It seems that the increasing of the temperature does not lead to a strong speeding-up of the proton dynamics. The elastic amplitude decreases as the temperature increases which can be due to the decrease of the Debye-Waller factor.

In order to obtain the typical relaxation time of the proton the differential signal need to be fitted with a proper model. In viscous liquid often an (stretched) exponential decay of the correlators is expected. In the energy domain analysis this corresponds to a simple Lorentzian function or the Fourier transformation of a stretched exponential

function (KWW function) convoluted with the instrumental energy resolution function $R(q, \omega)$

$$S(q, \omega) = \text{FT}\{A \exp(-t/\tau)^\beta + \text{bg}\} \otimes R(q, \omega). \quad (6.1)$$

Fig.6.5 shows the fitting results for two different temperatures of 950 K and 1150 K at the momentum transfer of 1.0 \AA^{-1} and 1.4 \AA^{-1} according to equation 6.1. The data

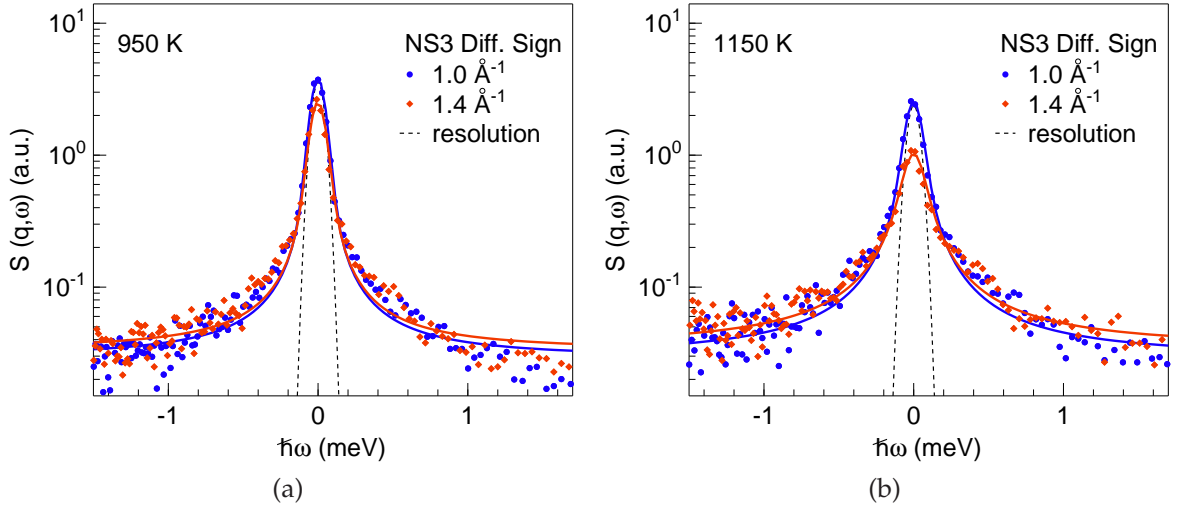


Figure 6.5: Differential scattering function of two different temperatures of 950 K and 1150 K at the momentum transfer of 1.0 \AA^{-1} and 1.4 \AA^{-1} , fitted with the Fourier transformation of a stretched exponential function plus a background, convoluted with the instrument resolution function.

were fitted within an energy transfer range of $[-2, 2] \text{ meV}$. The background is independent of the energy transfers. For the fitting procedure the stretching exponent β is fixed as an input. Different exponents from 0.6 to 1.0 were used to fit the data. However as it could be seen from the figure that the fitting function cannot fully match the scattering function, especially in the wing parts of the quasielastic signals. The measured differential scattering function contains obviously an elastic contribution which is more pronounced at lower temperatures. This causes the underestimation of the relaxation time τ or extreme small stretching exponents β which is not physically meaningful if it is fitted with a KWW function.

The next possible model one could use is a stretched exponential decay according to equation 6.1 plus an additional elastic contribution. However this leads to at least 4 free parameters: amplitude of the (Fourier transformed) stretched exponential function A , amplitude of the elastic contribution, the characteristic relaxation time τ and the stretch exponent β . Since the ratio between the amplitude of the elastic contribution and of the exponential function is unknown before the fitting this could lead to an over-interpretation of the data.

Many H containing sample systems, especially disordered systems often show anomalous diffusion behaviour of the hydrogen dynamics. Sub-linear dependence of the mean square displacement of the proton has been observed. According to the introduction in the section 3.2.2, for such diffusion behaviour the high frequency wing of the scattering function could show a power law behaviour $\omega^{-(1+\alpha)}$. Fig.6.6 shows the fitting results of the differential scattering function of 950 K and 1150 K at the momentum transfer of 1.0 \AA^{-1} by an power law function $h\omega^{-(1+\alpha)}$. The main advantage

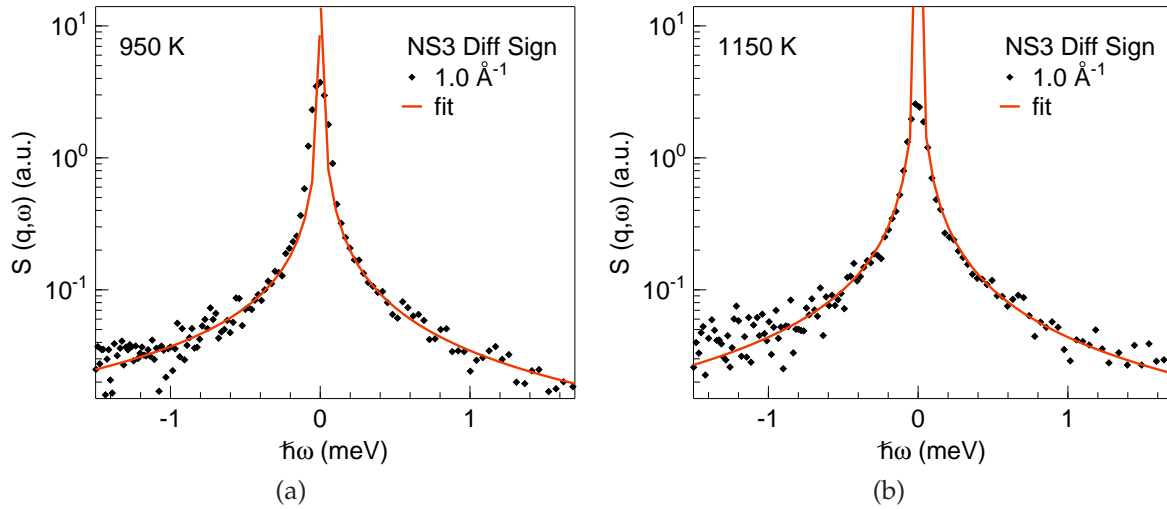


Figure 6.6: Differential scattering function $S(q, \omega)$ of a) 950 K and b) 1150 K, both at the momentum transfer of 1.0 \AA^{-1} . The scattering function is fitted with a power law function $h\omega^{-(1+\alpha)}$ for the large energy transfer part and is thus not convoluted with the instrument resolution function.

is that the fitting function does not need to be convoluted with the instrumental energy resolution function. The power law behaviour appears at large energy transfer and is thus not affected by the instrument resolution function. The fitting ranges were $[0.3, 2.1] \text{ meV}$ for the positive half of the spectra (neutron energy gain) and $[-1.7, -0.3] \text{ meV}$ for the negative half of the spectra (neutron energy loss) which are both beyond the range of the instrument resolution function.

From the figure it can be seen that for both temperatures the power law can well describe the signal at large energy transfers. However, due the limit of the energy range the time exponent obtained from the fitting subjects to large errors. Furthermore, the approximation of $|w| \gg |f(q)\nu(\omega)|$ is not completely valid. Thus the Chudley-Elliott function $f(q)$ enters and the time exponent shows q dependence at large momentum transfer. The $f(q)$ here cannot be revealed as like hydrogen diffusion in single crystal metal from the structure (e.g.: bcc or fcc). A good determination on the time exponent is therefore not feasible.

In the energy domain analysis the overlap of the elastic component and the (Fourier

transformed) exponential component intensity cannot be easily resolved. In such case it is better to analysis the spectra in the time domain since the amplitudes of different components are separated in timescales. Nevertheless the analysis in energy domain on the high frequency wings of the spectra still indicates that there might be an anomalous diffusion behaviour of the proton.

6.2.2 Time domain analysis

The elastic contribution in the scattering function $S(q, \omega)$ is represented in the intermediate scattering function $S(q, t)$ as a constant at large timescale. Fig.6.7 shows a comparison between the intermediate scattering function of the proton signal in hydrous sodium trisilicate melt and the one of the sodium in sodium disilicate melt. The

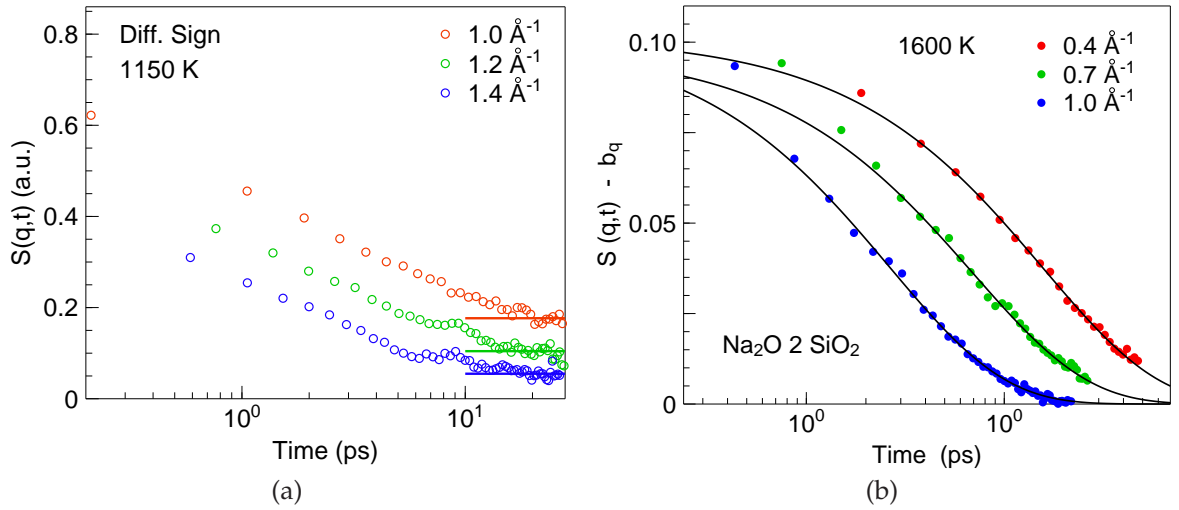


Figure 6.7: Intermediate scattering function of different diffusing species in silicate melts at different temperatures. a) Proton signal in hydrous sodium trisilicate melt at 1150 K. The thin lines show the non-zero constant value at large time. b) Sodium signal in sodium disilicate melt at 1600 K. The scattering intensities b_q from Si-O matrix has been subtracted, from [KMKS06]. The decay of the scattering function represents sodium ion relaxation in the silicate melt, which can be described by a stretched exponential function.

dynamics of proton in hydrous sodium trisilicate melt shows significant differences compared to that of the sodium in sodium disilicate melt. In sodium silicate melt the dynamics can be well described by a stretched exponential function with a stretched exponent around 0.75. In contrast the proton dynamics exhibits extreme stretching. If it is described by a stretched exponential function the stretching exponent would be extremely small which is unphysical.

It can also be noticed that the proton dynamics is not that fast as one would expected from the comparison with the sodium dynamics in sodium silicates. In sodium

disilicate when the contribution from the slow Si-O matrix is subtracted, sodium dynamics can be observed which decays completely to zero within a timescale up to about 30 ps at 1600 K. However, the proton dynamics still not fully decays to zero at a time round 20-25 ps at 1150 K, even with the contribution from the slow matrix is excluded via contrast variation. A notable non-zero constant $f^2(q)$ can be identified which is more pronounced at small momentum transfers where the dynamics is not that fast.

It is a question now what is the origin of this slow component in the proton dynamics. If one refers to water speciation in the hydrous silicate the slow component could be the molecular water. Thus, it could be that there exists different proton environments in the melt. However, it can be shown in the following section that with a detailed analysis of the q and temperature dependence of the plateau value and the amplitude of the decay such cases can be excluded.

An extreme stretching of the intermediate scattering function indicates that it could be described with a logarithmic decay. Fig.6.8 shows the differential signal of the intermediate scattering function fitted with a logarithmic function and a constant plateau value $f^2(q)$ at large time. Here the pure incoherent signal of the proton is normalized to its $t = 0$ value $S(q, t = 0)$. The plateau value is first determined by fitting a constant at the time interval of 18-25 ps. This corresponds to the resolution function decays to 50%-30% of its initial value. The fitted logarithmic function is given by

$$S(q, t) = f^1(q) + h_q \ln(t/\tau_0) \quad (6.2)$$

where τ_0 is fixed at 3 ps. Thus the long time constant value $f^2(q)$ and the amplitude of the logarithmic decay $f^1(q)$ are independent of each other. It can be seen that the logarithmic function describes the scattering function quite well in this time interval. For even smaller time (less than 0.8 ps) the contribution of vibrational motion can become more significant.

Fig.6.9 shows the q and temperature dependence of the amplitude of logarithmic decay $f^1(q)$ and the plateau value $f^2(q)$. It can be seen that the plateau value shows a rather smooth decay as a function of momentum transfer. The presence of slow molecular water dynamics can be hence exclude since otherwise the $f^2(q)$ would show oscillation at the momentum transfer around $q=1.0 \text{ \AA}^{-1}$ which represents the characteristic length scale in molecular water. Furthermore it is known that the concentration ratio between the hydroxyl and the molecular water changes as a function of temperature [BN03]. However, as shown in Fig.6.9b the difference between $f^1(q)$ and $f^2(q)$ is fairly independence of temperature. Thus, from our observation there is no evidence of different proton environments due to different water species which leads to different proton dynamics.

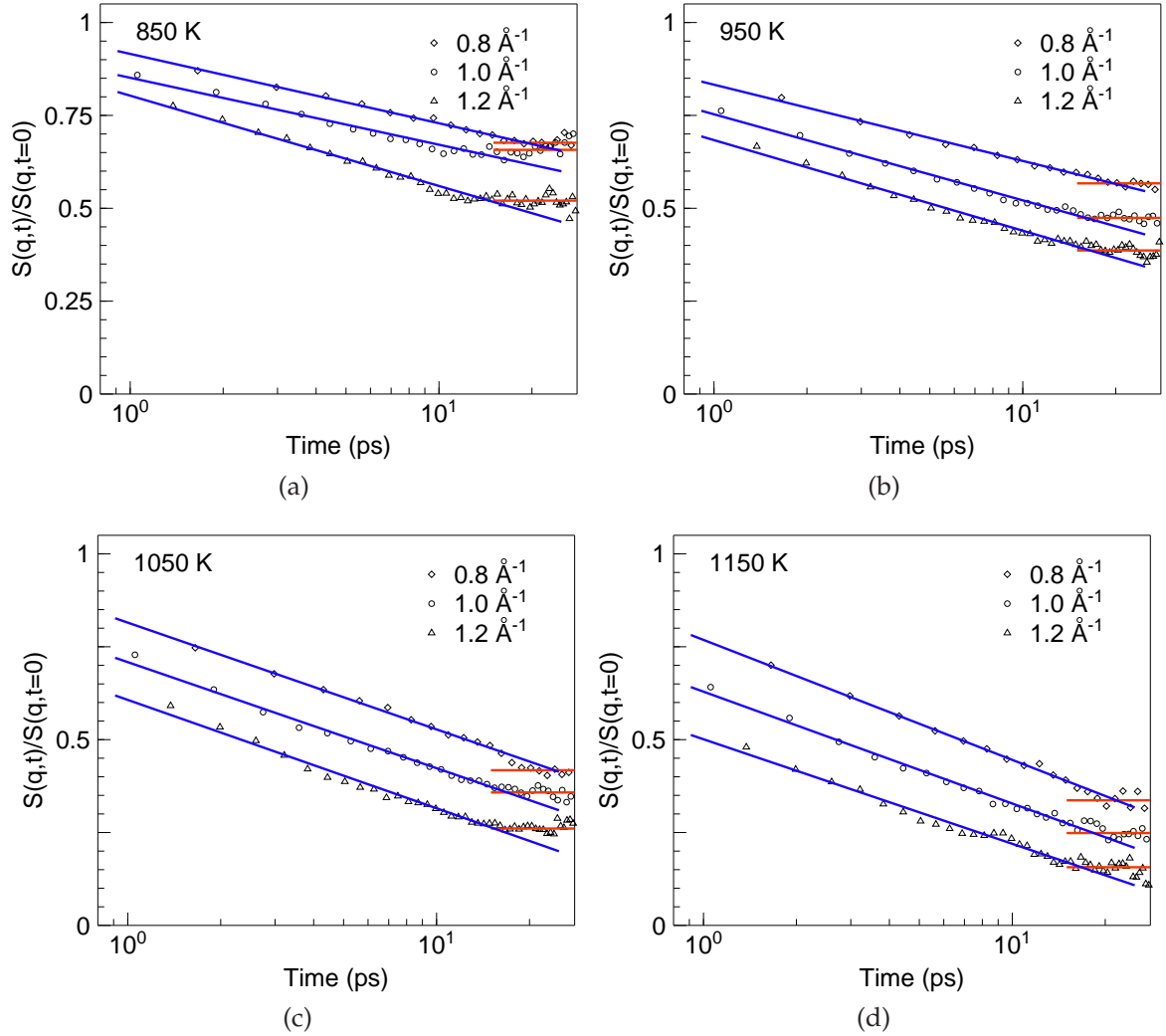


Figure 6.8: Intermediate scattering functions of the differential signal at different temperatures and momentum transfers. The scattering functions were fitted with a logarithmic function for the time range of 0.8-18 ps and a constant plateau value at 18-25 ps. For the fitting the τ_0 in equation 6.2 is fixed at 3 ps in order to make the amplitude $f^1(q)$ and $f^2(q)$ be independent of each other.

Mode couple theory has predicted the intermediate scattering functions could show logarithmic decay behaviour when the systems have higher order glass transitions [GS89, FHL92]. Anomalous diffusion behaviour can be also found under such scenario. This is understood as a signature that in the system there are different competitive arrest mechanisms.

Such dynamic feature has been observed in molecular dynamic simulations for both sodium silicates [HKB02, VH06] and colloidal systems [MC06a, MC06b]. Generally systems exhibit such dynamics are mixtures of different particles with a sufficient large size disparity and of weak interactions. The arrest mechanisms of the small par-

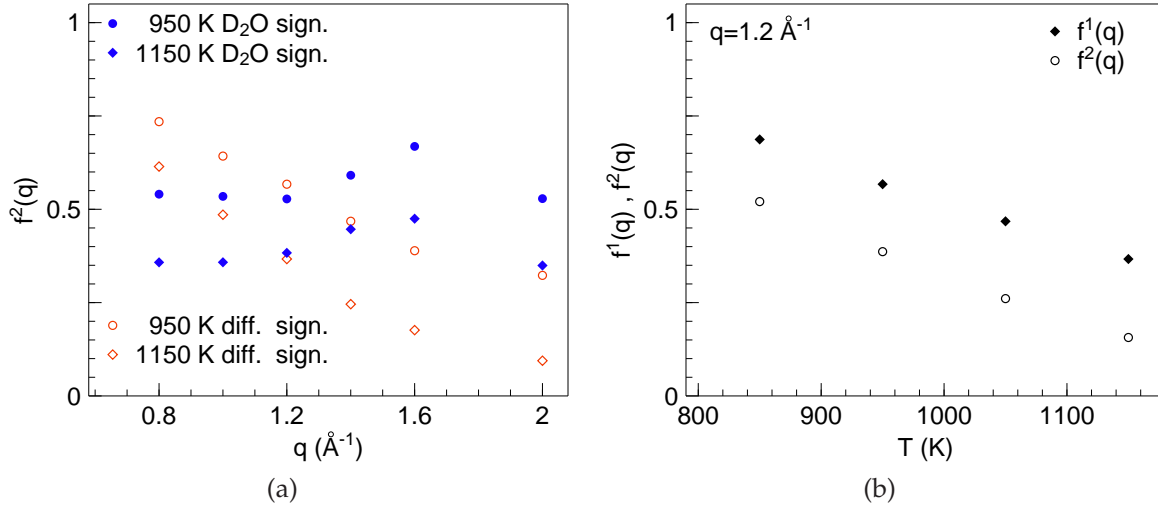


Figure 6.9: Q and temperature dependence of the amplitude of the logarithmic decay $f^1(q)$ and the constant value $f^2(q)$. a) Plateau value as a function of q , shown for two different temperatures. Values from the D₂O samples are shown as well for comparison which represent the melt structure. b) Temperature dependence of $f^1(q)$ and $f^2(q)$ at $q = 1.2 \text{ \AA}^{-1}$.

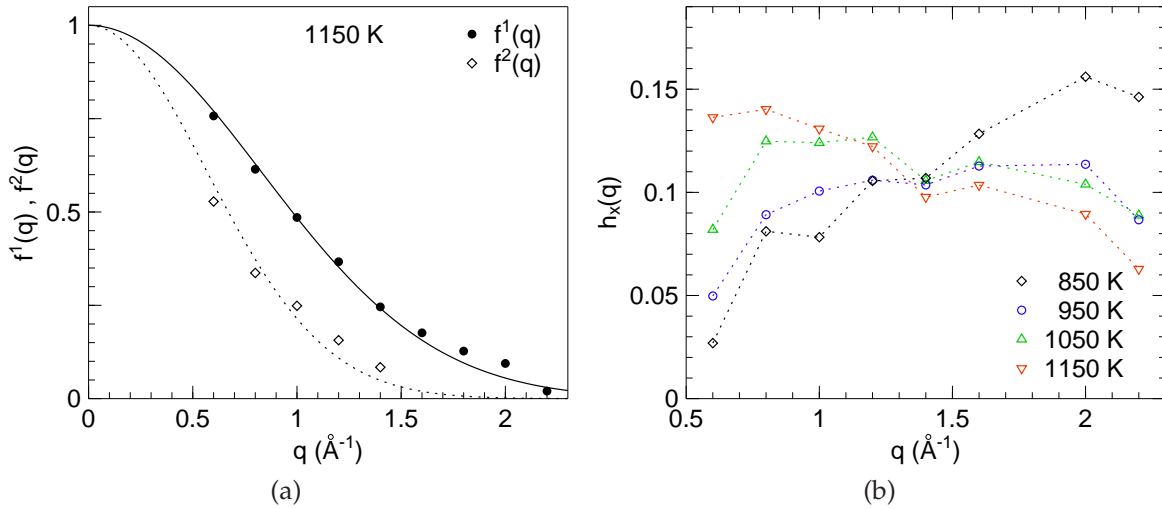


Figure 6.10: Momentum transfer and temperature dependence of the resulting fit parameters. Mode coupling theory predicts the $f^1(q)$ and $f^2(q)$ are smooth functions of momentum transfer which can be fitted with Gaussian function (thin lines). In $h_x(q)$ the thin lines are only guides for eyes.

ticles could be either caused by the large particles or by the complete system. Under certain conditions, a double glass transition can occur, where the small particles can still diffuse in the immobile glassy large particle matrix before the complete system frozen in. From the calculation of the mode coupling theory the $f^1(q)$ and $f^2(q)$ as well as the slope of the logarithmic decay h_x show unique q and temperature depen-

dence under such scenario. Our observations in the hydrous silicate melt have shown qualitatively similar features.

Another character in the dynamics of these systems is the decoupling of different correlation functions in timescales, often by orders of magnitude. Such feature has been observed here as well as in the hydrous (dry) sodium silicate melts that the dynamics of proton (sodium) are of orders of magnitude faster than the Si-O matrix.

It should be noted that till now such observation are mostly reported in the molecular dynamic computer simulations since a wide observation time windows is needed in order to make an ambiguous conclusion. Thus, investigations with larger timescales are necessary on the hydrous silicate melts to monitor how this plateau value in current time window decays finally to zero.

6.3 Deuterated sodium trisilicate melt

Fig.6.11 shows the measured spectra of deuterated sodium trisilicate melt with 10 mol% D₂O content for two different temperatures and momentum transfers. As it

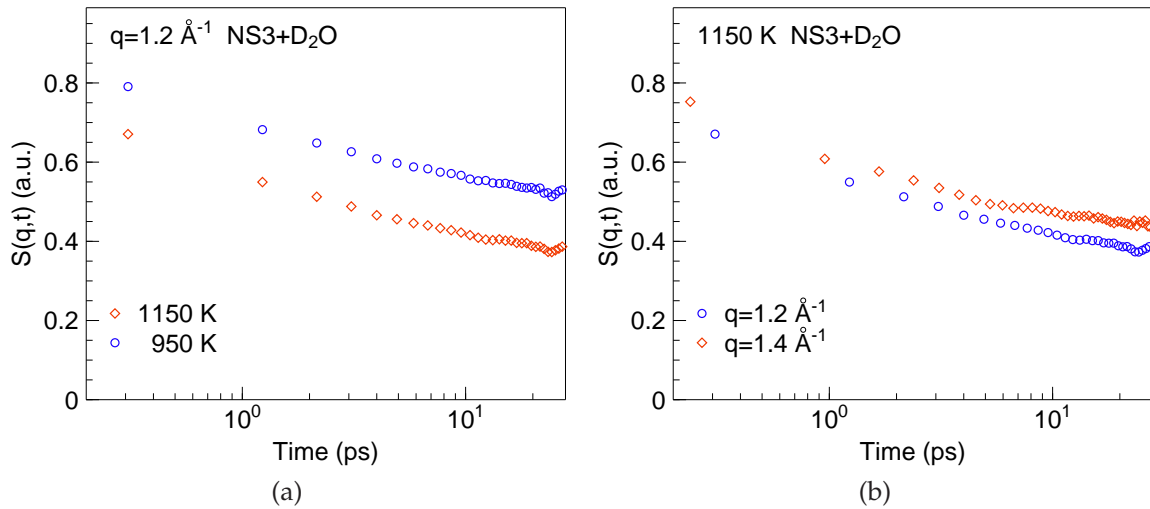


Figure 6.11: Measured spectra of deuterated sodium trisilicate melts. a) Intermediate scattering function at two different temperatures of 950 K and 1150 K, respectively. b) Spectra of two different momentum transfers of 1.2 Å and 1.4 Å, respectively at a temperature of 1150 K.

can be seen from the spectra, the D₂O samples show slower dynamics compared to the corresponding proton signals. The overall intensity is lower due to the smaller scattering cross sections but the second plateau value $f^2(q)$ is higher. It also exhibits a different q dependence if one refers to Fig.6.9a. This is mainly due to the fact that in the D₂O containing samples, the signal is dominantly coherent and contributed not only from the scattering on D₂O but also on sodium, silicon and oxygen atoms. It should be

noted that the mode coupling theory predicts a slower dynamics of the coherent correlator at some characteristics q values in such system, for example in sodium silicate melts [HKB02, VH06]. However, such prediction cannot be directly verified here since the signal composes not only the coherent scattering from deuterium but also from the sodium and Si-O matrix.

6.4 Backscattering measurement

In order to measure at longer timescale a neutron backscattering experiment was performed. Prior to the high temperature and pressure experiment, a test measurement was conducted using a dummy cell same as the one used for TOFTOF test experiment with the original SPHERES setup (unchanged, so that small angle analyzers can be used). The test was done by measuring spectra of the empty cell, empty cell with a Al_2O_3 ceramic piece same as used for the furnace and the complete cell together with a hydrous NS3 sample. All measurements were performed at room temperature with a Doppler speed of 1.3 m/s. The spectra are shown in Fig.6.12. A significant contribution

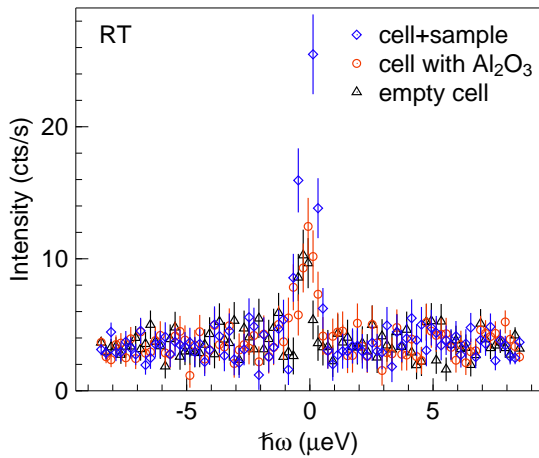


Figure 6.12: Spectra from the test experiment of a dummy cell at SPHERES. Measurements are done with the Nb cell only, Nb cell with Al_2O_3 ceramics and the whole assembly with a sample. Here a large contribution from the sample can be still seen (factor of 2), although signals were quite noisy.

from the sample to the signal can be still identified.

For the high temperature high pressure experiment one protonated sodium trisilicate sample was measured with 10 mol% total water content. A temperature scan was performed with the Doppler driver speed at 0.2 m/s, corresponding to a dynamic range of $\pm 1.32 \mu\text{eV}$, in order to observe the onset temperature of the dynamics. The sample was first heated up to 850 °C than cooled down to around 150 °C with a constant cooling rate of 1 °C/min. Spectra were recorded with an accumulation time of 3 minutes. The measured spectra were then integrated over the complete energy range to give the intensity. The intensity as a function of temperature is shown in Fig.6.13.

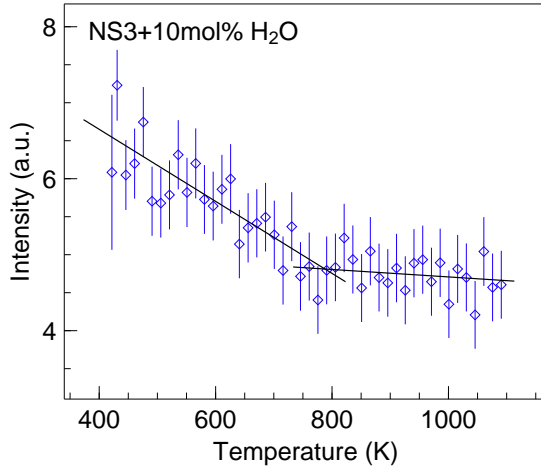


Figure 6.13: Temperature scan of the hydrous sodium trisilicate sample with 10 mol% H_2O from 850 °C down to 150 °C with a cooling rate of 1 °C/min. Two generally trends can be seen with different slopes as fitted by two lines. However, at high temperature the intensity might be already dominated by the background.

Two trends can be identified in the figure. However, the high temperature trend is almost a constant and is very likely that it only represents the background level if one refers to the high temperature spectra in Fig.6.14a. Therefore, an unambiguous transition temperature cannot be concluded.

The sample was measured then at two different temperatures of 750 K and 900 K, respectively. The measured spectra are shown in Fig.6.14. Compared to the room

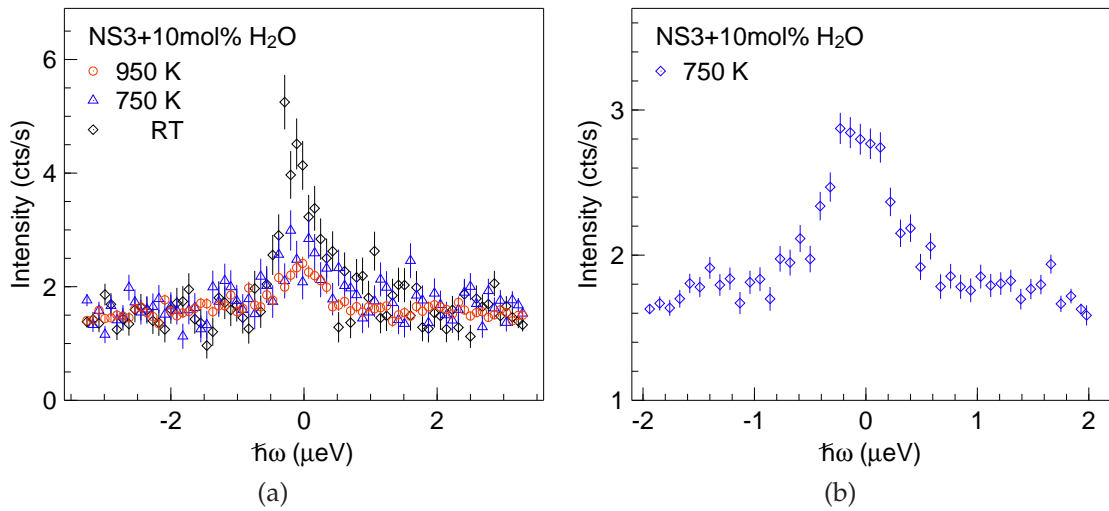


Figure 6.14: Measured spectra of sodium trisilicate melt with 10 mol% H_2O at different temperatures. a) Intensity as a function of energy transfer at room temperature, 750 K and 900 K with a Doppler driver speed of 0.5 m/s. b) Spectrum of the same sample measured at 750 K with a Doppler driver speed of 0.3 m/s.

temperature measurement a reduction in the elastic peak intensity can be seen. However due to the high background a quasielastic broadening cannot be quantitatively

resolved. The sample was measured as well at a slower Doppler driver velocity of 0.3 m/s to increase the neutron flux but this does not improve the situation very much.

In conclusion, although the high pressure high temperature conditions can be reached at SPHERES, due to the massive pressure cell which creates a high background a quasielastic broadening cannot be resolved in any spectrum.

6.5 Other silicate systems

Pure silica and albite samples with 10 mol% total water content were measured on TOFTOF spectrometer as well. Both systems are having significant higher viscosities compared to the hydrous sodium trisilicates if one refers to the glass transition temperatures of the dry systems ($\text{SiO}_2 \sim 1500$ K [Brü70], albite 1050 K [RPM⁺01]). Fig.6.15 shows the measured intermediate scattering function $S(q, t)$ of the hydrous silica and

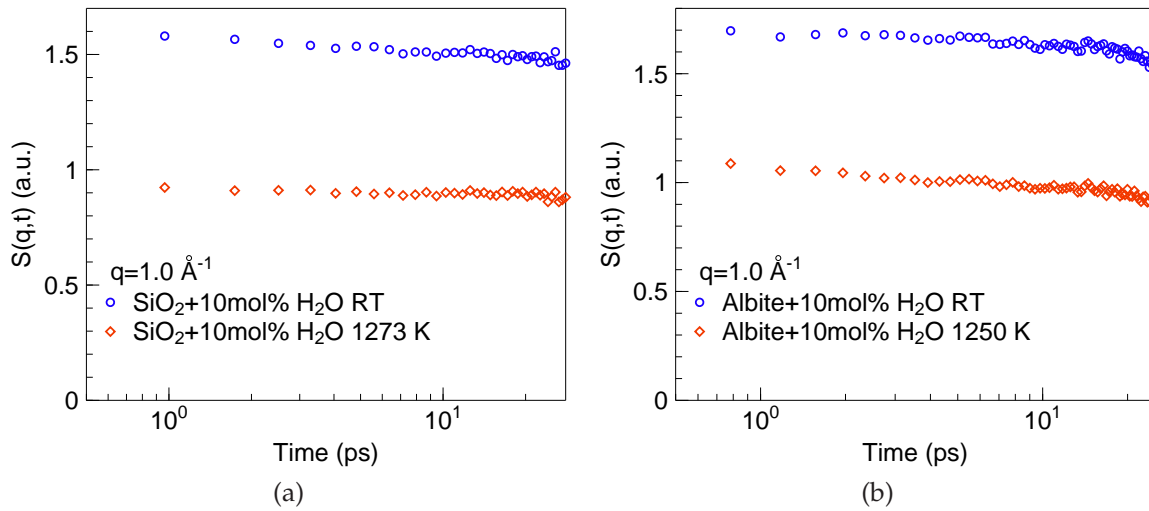


Figure 6.15: Measured intermediate scattering function $S(q, t)$ of the hydrous silica and albite melts. Within the time window of the observation the scattering function does not decay. Room temperature measurements are shown for comparison. It can be seen they are almost identical except the difference in the absolute value.

albite samples at room temperature and around 1250 K, respectively. The measured scattering functions remain nearly constant within the complete time window of the observation. Compared with the room temperature measurements, the spectra at elevated temperature have almost the same feature, only the absolute intensities are different. This indicates that the relaxation time of all the species in the system are larger than at least 25 ps. In albite system it should be noted that the addition of water does not speed up the sodium dynamics up to a relaxation time of 25 ps as well.

The hydrous albite samples were measured with a refined energy resolution using an incoming neutron wavelength of 6.5 Å. Such setup gives access to relaxation time up to 70 ps. The measured spectra of the pure proton signal at the highest measured temperature of 1250 K and a hydrous sample at room temperature are shown in Fig.6.16.

The measured spectra show basically the same behaviour like the spectra measured with lower energy resolution. Within the observation time window up to 70 ps the intermediate scattering function does not decay. Thus it can be concluded that the dynamics is not fast enough at this temperature to be investigated using the current instrument setup at TOFTOF.

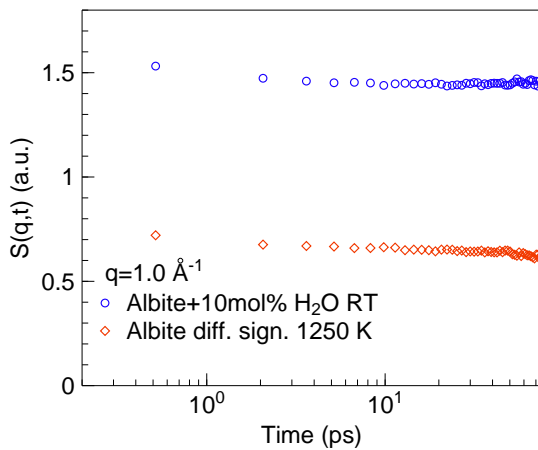


Figure 6.16: Measured intermediate scattering function of hydrous albite sample using the high resolution setup. Such setup gives access to a time window up to 70 ps. However by comparing the room temperature measurement with the highest temperature measurement it can be concluded that there is no onset of observable dynamics in this time window.

Problems of further increase of the measurement temperature

In this study the highest investigation temperature is 1273 K (1000 °C), used at the measurements of the hydrous silica sample. It will be certainly very interesting to observe the dynamics in silica system, since the results can directly clarify the role of the proton in silicates and to be compared with alkali oxides. However, no higher temperature measurement was performed, although the furnace in the pressure cell is capable to reach a temperature up to 1500 K and at higher temperature the dynamics in hydrous silica and albite melts might speed up to a measurable timescale of using the current instrument setup. This is mainly due to two considerations. First, increasing temperature of the furnace will increase the Nb cell temperature as well, which might lead to a reduction in the Nb strength and cause a failure of the cell. Second, increasing the temperature of the melt will increase as well the pressure which is needed to suppress water evaporation. It could happen that at higher temperatures the 200 MPa pressure is not sufficient and the sample will be foamed. Due to the tested pressure of 300 MPa

a further increase of the operation pressure beyond 200 MPa is not allowed according to the safety margin constrain.

From the measurements here it can only be concluded that the lower boundary value for diffusion coefficients in these systems is on the order of $10^{-10} \text{ m}^2\text{s}^{-1}$ in the temperature range of this study, although the glass transition temperature of the samples has already be decreased by a factor of 2 by adding 10 mol% of water.

Chapter 7

Outlook

7.1 Neutron scattering experiments

According to the results of the measurements on hydrous sodium trisilicate melts it is necessary to explore a broader timescale in order to verify the double glass transition scenario predicted by mode coupling theory. Essentially the final decay behaviour of the plateau $f^2(q)$ to zero at large timescale is still missing, which is expected by the theory to be a stretched exponential decay.

To study the dynamics of such system the ideal conditions would be to have an instrument setup which has a fine resolution as well as a large dynamical range, which ensures an access to a large time window. At the time of writing this thesis, a proposal has been submitted for the application of beam time on the neutron backscattering spectrometer BASIS at the Oak Ridge National Laboratory. BASIS is chosen for following reasons: 1) It is a spallation source based spectrometer located at SNS, an additional gain of neutron flux can be hence achieved for TOF kind instruments. 2) It is designed for high energy resolution as well as large energy and momentum transfer experiments by using a nearly backscattering geometry. For such setup the analyzers and the detectors are located at the same side of the sample. Thus, a gain in the accessible momentum transfer and neutron flux can be achieved, since the neutrons only pass the sample and its environment once. This is particularly helpful for the pressure cell design in this study since a complete access to all radial angles is not necessary. The drawback is of course the worse energy resolution compared to traditional exact backscattering geometry spectrometer. However, by using a nearly backscattering geometry (88°) an energy resolution as good as $2 \mu\text{eV}$ can be achieved which is still better than the time-of-flight type instrument and is sufficient to study the dynamics up to the order of ns.

Such experiment will allow the study of the final decay of the proton dynamics and gain more insight of the water species diffusion mechanisms. Also a comparison

with the prediction of the mode coupling theory is possible.

If the measurements on hydrous sodium trisilicate melt turn out to be successful, subsequent investigations can be performed on SiO_2 and albite systems as well. Hydrous SiO_2 system would be particularly interesting since it is the simplest system and the results (especially the one of the D_2O containing samples) can be directly compared with the theory predictions on the coherent correlators as well.

7.2 Diffusion couple measurements

7.2.1 Ex-situ experiments

Due to the limit of the instrumental energy resolution and the anomalous diffusion behaviour, a self diffusion coefficient of the proton in hydrous silicate melts is not available with the neutron scattering techniques. However, diffusion coefficients can be still measured with other techniques.

One of the primary methods to investigate diffusion is the diffusion couple experiment. In such experiments two specimens with different concentrations of diffusion species are put together under a certain temperature (as well as pressure) conditions which allows these species to diffuse. After reaching the desired time of the diffusion, the experiment is stopped (normally by quenching) and the concentration profiles are examined usually via thin sections of the samples and diffusion coefficient can be obtained by Matano analysis.

In these measurements diffusions are studied on a macroscopic length and time scales. Typical diffusion distances are from μm up to cm range with a diffusion time in order of minutes to hours. Even very slow diffusions can be measured with such technique e.g.: [BS00].

It should be noted that in such experiments different diffusion coefficients can be measured. If the concentration of the diffusing species are different, the diffusion is driven by chemical potential gradient and the resulting diffusion coefficient is the chemical diffusion coefficient. If the chemical composition of the two diffusion couples are the same, only different isotopes of one (same) element are present in the initial samples, one measures the self diffusion coefficient of the element, which is often called tracer diffusion coefficient where the diffusion is driven by entropic forces. The tracer diffusion coefficient is comparable with the diffusion coefficients measured with neutron scattering techniques.

Diffusion couple technique has been widely used to study water diffusion in silicates on many compositions (e.g.: [ZS91, NB97], for a recent experiment see [Beh06]) and diffusion mechanisms and models are proposed (for review see [BN97, Zha99]). In

most of these experiments the initial (total) water concentrations in the two diffusion couples are different and therefore chemical diffusion coefficients are measured. However, such method can be applied to measure tracer diffusion coefficient as well using silicate diffusion couple samples having the same water content with $\text{H}_2\text{O}/\text{D}_2\text{O}$ and the results from such experiments can be compared with the neutron experiments results. Current sample preparation apparatus is already suitable for such studies without significant modifications since it provides a pressure up to 300 MPa and a quite homogenous temperature profile over the sample (see Fig.2.5b).

It is not easy to clarify the diffusion mechanisms with the diffusion couple experiment alone since the obtained results is an average over macroscopic scales and is hence effectively at one q value. However, it provides as well important informations, for example whether the self diffusion coefficient is connected with melt viscosity according to the Einstein relation.

7.2.2 Neutron radiography

Combination of diffusion couple experiments and time-resolved radiography gives the possibilities of direct in-situ observation of diffusion processes. Such experiments have been already performed with X-ray radiography on metallic melts [GMMF06].

H is an ideal scatterer for neutron imaging owing to its large scattering cross section which can create a good contrast. Neutron radiography and tomography have been demonstrated to be a very useful tool for non-destructive imaging and time-resolved imaging can be used to study dynamic properties of the sample. For example, it has been applied to measure the viscosity of silicate melts using falling sphere method [BWK⁺01, KWHB03]. Perform diffusion couple experiments with $\text{H}_2\text{O}/\text{dry}$ or $\text{H}_2\text{O}/\text{D}_2\text{O}$ samples to create contrast for neutrons imaging should be in principle possible using the current pressure cell setup and both chemical and self diffusion coefficients can be measured. However, to use such technique a major challenge would be to provide a homogenous and stable temperature profile over the complete sample under high pressure conditions.

Appendix A

Neutron scattering cross sections

Following table lists a number of elements which are present in the samples studied by this work. Coherent, incoherent and absorption cross sections are shown for each elements. The values are taken from [DL02] for bound nuclei. Values for absorption cross section correspond to that of the thermal neutrons ($v=2200$ m/s, $\lambda=1.8$ Å).

Ele.	σ_{coh}	σ_{inc}	σ_{ab}
Al	1.495(4)	0.0082(6)	0.231(3)
H	1.7568(10)	80.26(6)	0.3326(7)
D	5.592(7)	2.05(3)	0.000519(7)
Na	1.66(2)	1.62(3)	0.530(5)
O	4.232(6)	0.000(8)	0.00019(2)
Si	2.163(10)	0.004(8)	0.171(3)

Table A.1: Neutron scattering cross sections for the elements which are present in the sample system of this study. Values are given in barn [10^{-24} cm²].

The scattering cross sections for the different samples in the study are listed in the following table.

Sample	σ_{coh}	σ_{inc}	Sample	σ_{coh}	σ_{inc}
NS3+10mol% H ₂ O	3.217	5.585	NS3+10mol% D ₂ O	3.471	0.381
SiO ₂ +10mol% H ₂ O	3.446	5.352	SiO ₂ +10mol% D ₂ O	3.702	0.138
Albite+10mol% H ₂ O	3.275	5.087	Albite+10mol% D ₂ O	3.513	0.242
NS3 dry	3.286	0.271	Albite dry	3.346	0.127

Table A.2: Scattering cross sections (in barn) for samples used in this study. Note the difference between H₂O and D₂O containing samples.

Appendix B

List of neutron scattering experiments

Following tables list the neutron scattering experiments which have been performed during the time of this thesis and their basic setup. All hydrous samples have a total water content of 10 mol%.

TOFTOF June 2007

$\lambda=5.1 \text{ \AA}$

chopper speed 12,000 rpm

chopper ratio 3

High T/P cell

Sample	Temperature	time
V	RT	1 hr
empty cell	RT, 850-1250 K	11.5 hrs
NS3 + H ₂ O	RT, 850-1250 K	25 hrs
NS3 + "D ₂ O" ¹	RT, 850-1250 K	11 hrs
NS3 dry	RT, 1050-1150 K	15 hrs
SiO ₂ + H ₂ O	RT, 1150-1273 K	6 hrs

¹Sample exchanged with H₂O during the preparation.

TOFTOF November 2007

$\lambda=5.1 \text{ \AA}$

chopper speed 12,000 rpm

chopper ratio 3

High T/P cell

Sample	Temperature	time
V	RT	2 hrs
empty cell	RT, 850-1250 K	11 hrs
NS3 + D ₂ O	RT, 850-1150 K	37 hrs
Albite + H ₂ O	RT, 1250 K	14 hrs
Albite + D ₂ O	RT, 1250 K	2 hrs
Cd	RT	2 hrs

$\lambda=6.5 \text{ \AA}$
 chopper speed 16,000 rpm
 chopper ratio 4
 High T/P cell

Sample	Temperature	time
V	RT	2 hrs
empty cell	RT, 1250 K	3 hrs
Albite + H ₂ O	RT, 1250 K	17.5 hrs
Albite + D ₂ O	RT, 1250 K	6 hrs

SPHERES July 2008

$\lambda=6.271 \text{ \AA}$
 Si 111 monochromator
 Doppler speed 0.2 m/s
 $-1.32 \mu\text{eV} < E < 1.32 \mu\text{eV}$
 temperature scan

Sample	Temperature	time
NS3 + H ₂ O	ramp RT-1150 K	2 hrs
NS3 + H ₂ O	ramp 1150-430 K	15 hrs

$\lambda=6.271 \text{ \AA}$
 Si 111 monochromator
 Doppler speed 0.5 m/s
 $-3.3 \mu\text{eV} < E < 3.3 \mu\text{eV}$

Sample	Temperature	time
NS3 + H ₂ O	RT	20 hrs
NS3 + H ₂ O	750 K	2.5 hrs
NS3 + H ₂ O	900 K	44 hrs
V (no cell)	RT	20 hrs

$\lambda=6.271 \text{ \AA}$
 Si 111 monochromator
 Doppler speed 0.3 m/s
 $-1.98 \mu\text{eV} < E < 1.98 \mu\text{eV}$

Sample	Temperature	time
NS3 + H ₂ O	750 K	20 hrs

List of Figures

1.1	Different techniques to measure the glass transition temperature	3
1.2	Structure relaxation and transport coefficients in sodium silicates	5
1.3	Formation of diffusion channels in sodium trisilicate melts	5
1.4	Effects of different components on the structure of silicate melts	6
1.5	Viscosity of hydrous silicate melts and the water speciation	8
2.1	Dry sodium trisilicate block sample after preparation	12
2.2	Preparation of the sample capsules for water dissolution	14
2.3	Schematic view of the sample preparation setup	16
2.4	Three-zone furnace for sample preparation	17
2.5	Sketch of the preparation furnace and its temperature profile	18
2.6	DSC measurements on hydrous sodium trisilicate samples	19
2.7	Comparison between DSC and dilatometry measurement results	21
2.8	Dilatometric measurement results of a dry albite sample	22
2.9	Dilatometric measurement results of hydrous albite samples	22
3.1	Pair correlation function $g(r)$ of a monoatomic liquid	31
3.2	MCT calculations of different relaxation processes in viscous liquids . . .	38
4.1	Strengthening effects as a function of wall ratio	44
4.2	Temperature dependence of the strength of Nb and Nb1Zr alloy	46
4.3	Technical drawing of the inner Nb1Zr cell	47
4.4	The high temperature / high pressure sample environment	48
4.5	Temperature measurements using temperature sensitive paints	51
4.6	Technical drawing of the complete neutron scattering apparatus	52
4.7	Stick to insert the sample capsule into the pressure cell	53
4.8	Schematic view of the complete setup on the TOFTOF spectrometer . . .	54
4.9	Intensity as a function of scattering angle of the empty pressure cell . . .	56
4.10	Spectra of the empty pressure cell under different temperature and pres- sure conditions	57

4.11	$I(2\theta, ToF)$ of the empty pressure cell and a hydrous silicate sample at 1250 K under 1800 bar	58
5.1	Schematic view of the TOFTOF time-of-flight spectrometer setup	60
5.2	White beam flux at the sample position of TOFTOF spectrometer	60
5.3	Detector bank of the TOFTOF spectrometer	62
5.4	Accessible q - ω range on the TOFTOF spectrometer using 5.1 Å incoming wavelength	62
5.5	Self absorption correction factors for a NS3 sample with 10 mol% H ₂ O	67
5.6	Deconvolution of the instrument resolution function in time space	69
5.7	General layout of the neutron backscattering spectrometer SPHERES	71
6.1	Measured spectra of dry sodium trisilicate melt on TOFTOF	73
6.2	Scattering functions of different samples measured on TOFTOF at 1150 K	74
6.3	Contrast variation and the differential signal at 1150 K	75
6.4	Measured scattering function $S(q, \omega)$ at different temperatures	76
6.5	Differential scattering functions fitted with power law equation	77
6.6	Comparison between proton relaxation and sodium relaxation	78
6.7	Intermediate scattering function of different diffusing species in dry and hydrous sodium silicate melts	79
6.8	Logarithmic decay of the proton relaxation in hydrous sodium trisilicate melt with 10 mol% water content	81
6.9	Q and temperature dependence of the amplitude of the logarithmic decay $f^1(q)$ and the constant value $f^2(q)$	82
6.10	Momentum transfer and temperature dependence of the resulting logarithmic fit parameters	82
6.11	Measured spectra of deuterated sodium trisilicate melts	83
6.12	Spectra from the test experiment of a dummy cell at SPHERES	84
6.13	Temperature scan of the sodium trisilicate melt with 10 mol% H ₂ O measured on SPHERES from 1120 K to 420 K	85
6.14	Neutron backscattering spectra of sodium trisilicate melt with 10 mol% H ₂ O for different temperatures measured at SPHERES	85
6.15	Intermediate scattering function of the hydrous silica and albite melts	86
6.16	Intermediate scattering function of hydrous albite sample measured with the high resolution setup on TOFTOF	87

List of Tables

2.1	Conversion from water mol % to wt % of the samples	14
4.1	Neutron scattering and absorption cross section for different elements used in alloys for high temperature applications.	45
A.1	Neutron scattering cross sections of elements	93
A.2	Neutron scattering cross sections of the samples in this study	93

Acknowledgement

First I would like to thank Prof. Andreas Meyer for offering me the possibility to finish this thesis under his supervision, for his continuous support during the complete thesis time as well as for introducing me into this very interesting field of physics and geology.

I would like to thank Prof. Winfried Petry for giving me the chance to work on my thesis in his chair.

For the neutron experiments at FRM II I would like to express my thanks to Dr. Tobias Unruh, Dr. Jürgen Peters and Dipl.-Ing. Jandal Ringe for many efforts to setup my new sample environment, for kindly providing the gas pressure generator and support. I also thank Dr. Tobias Unruh for the discussion on the neutron data.

Special thanks to Dr. Kai-Uwe Hess at the department of earth and environmental sciences, LMU, who helped me on the measurements there, introduced me on many geological topics and discussed with me on the results.

At DLR I would like to thank Dr. Thomas Voigtmann for discussions and Dipl.-Phys. Ines Pommrich for her help during the neutron beam time.

I thank Dr. Joachim Wuttke at JCNS for his support during the neutron backscattering experiment.

For the development of the sample preparation apparatus and the high temperature high pressure cell I would like to thank Dipl.-Ing. Josef Kaplonski at E13 and Mr. Michael Stanger at Kristalllabor for their active support.

At E13 I would like to express my thanks to Prof. Walter Schirmacher, my PhD colleagues Dipl.-Phys. Sebastian Stüber and Dipl.-Phys. Andreas Meier-Koll for discussions, help during beam times and daily work. I also thank all the other members, for their help and providing a nice working atmosphere.

The Financial support from DFG under the grant number Me1958/8-2 is kindly acknowledged.

I thank Prof. Andreas Meyer, Dr. Florian Kargl and Mr. Constantin Tomaras for reading my manuscript.

Finally I would like to thank my family for continuously supporting my scientific work abroad.

Bibliography

- [BBTC91] T. Bausenwein, H. Bertagnolli, K. Tödheide, and P. Chieux. Nucl. Instr. and Meth. Phys. Res. B, **61**(4), p.527, 1991. 66
- [Beh06] H. Behrens. Adv. Sci. Tech., **46**, p.79, 2006. 90
- [BMK⁺95] M. Ben-Chorin, F. Möller, F. Koch, W. Schirmacher, and M. Eberhard. Phys. Rev. B., **51**(4), p.2199, 1995. 35
- [BN97] H. Behrens and M. Nowak. Contrib. Mineral. Petrol., **126**(4), p.377, 1997. 90
- [BN03] H. Behrens and M. Nowak. Phase Trans., **76**(1&2), p.45, 2003. 7, 8, 80
- [Brü70] R. Brückner. *Properties and structure of vitreous silica I*. J. Non-Cryst. Solids, **5**, p.123–175, 1970. 11, 86
- [BS92] R. Brüning and K. Samwer. Phys. Rev. B, **46**(18), p.11319, 1992. 3
- [BS00] H. Behrens and F. Schulze. In *Applied Mineralogy in Research, Economy, Technology, Ecology and Culture. Proceedings ICAM*, D. Rammlmair, J. Mederer, T. Oberthür, R.B. Heimann, and H. Pentinghaus, editors, page 95. Balkema, Rotterdam, 2000. 90
- [BWK⁺01] G. Bayon, B. Winkler, A. Kahle, B. Hennion, and P. Boutrouille. Non-destr. Test. Eval., **16**, p.287, 2001. 91
- [CE61] C.T. Chudley and R.J. Elliott. Proc. Phys. Soc., **77**, p.353, 1961. 34
- [CLH⁺97] H.Z. Cummins, G. Li, Y.H. Hwang, G.Q. Shen, W.M. Du, J. Hernandez, and N.J. Tao. Z. Phys. B, **103**, p.501, 1997. 4
- [Cow01] J.M.G. Cowie. *Polymers: chemistry & physics of modern materials*. Nelson Thoners Ltd., 2nd edition, 2001. 3

- [Dav90] J.R. Davis, editor. *Metals Handbook Volume 2, Properties and Selection: Nonferrous Alloys and Special-Purpose Materials*. ASM International, Metals Park, Ohio, 10th edition, 1990. 46
- [Daw77] V.C.D Dawson. *High pressure containment in cylindrical vessels*. In *High Pressure Technology I, Equipment Design, Materials, and Properties*, I.L. Spain and J. Paauwe, editors. Dekker, New York, 1977. 42, 44
- [Din96] D.B. Dingwell. *Volcanic dilemma: Flow or blow?* *Science*, **273**(23), p.1054, 1996. 1
- [DL02] A.-J. Dianoux and G. Lander, editors. *Neutron Data Booklet, Institut Laue-Langevin*. 2002. 93
- [DR65] B.A. Dasannacharya and K.R. Rao. *Phys. Rev.*, **137**(2A), p.A417, 1965. 33
- [DRH96] D.B. Dingwell, C. Romano, and K.-U. Hess. *The effect of water on the viscosity of a haplogranitic melt under P-T-X conditions relevant to silicic volcanism*. *Contrib. Mineral. Petrol.*, **124**(19), 1996. 7, 8, 13
- [DW89] D.B. Dingwell and S.L. Webb. *Phys. Chem. Miner.*, **16**, p.508, 1989. 1
- [Ell91] S.R. Elliott. *Phys. Rev. Lett.*, **67**(6), p.711, 1991. 30
- [FA02] B. Frick and C. Alba-Simionesco. *Appl. Phys. A*, **74**(Suppl.), p.S549, 2002. 47, 66
- [FHL92] M. Fuchs, I. Hofacker, and A. Latz. *Phys. Rev. A*, **45**(2), p.898, 1992. 81
- [GM98] A. Grzechnik and P.F. McMillan. *Am. Mineral.*, **83**, p.331, 1998. 8
- [GMMF06] A. Griesche, F.G. Moreno, M.-P. Macht, and G. Froberg. *Mater. Sci. Forum*, **508**, p.567, 2006. 91
- [Göt91] W. Götze. *Aspects of Structural Glass Transitions*. In *Liquids, freezing and glass transition, Les Houches 1989, Session LI*, J.P. Hansen, D. Levesque, and J. Zinn-Justin, editors. North-Holland, Amsterdam, 1991. 37
- [Göt99] W. Götze. *Recent tests of the mode-coupling theory for glassy dynamics*. *J. Phys.: Condens. Matter*, **11**, p.A1–A45, 1999. 38
- [GS89] W. Götze and L. Sjögren. *J. Phys.: Condens. Matter*, **1**, p.4203–4222, 1989. 81
- [GS92] W. Götze and L. Sjögren. *Rep. Prog. Phys.*, **55**, p.241–376, 1992. 36, 37

- [HDW95] K.-U. Hess, D.B. Dingwell, and S.L. Webb. *Am. Miner.*, **80**, p.297–304, 1995. 6, 21
- [Hil99] R. Hilfer. *On fractional diffusion and its relation with continous time random walks*. In *Anomalous diffusion: From Basis to Applications*, A. Pękalski and K. Sznajd-Weron, editors, page 77. Springer, Berlin, 1999. 36
- [HKB02] J. Horbach, W. Kob, and K. Binder. *Phys. Rev. Lett.*, **88**(12), p.125502, 2002. 81, 84
- [HM86] J.P. Hansen and I.R. McDonald. *Theory of simple liquids*. Academic Press, London, 1986. 34
- [Hov54] L. van Hove. *Phys. Rev.*, **95**(1), p.249, 1954. 28
- [IHB⁺05] S. Indris, P. Heitjans, H. Behrens, R. Zorn, and B. Frick. *Phys. Rev. B*, **71**, p.064205, 2005. 9
- [JBB51] J.R. Johnson, R.H. Bristow, and H. Blau. *Am. Ceram. Soc.*, **34**(6), p.165, 1951. 4
- [KAD99] K. Knorr, B. Annighöffer, and W. Depmeier. *J. Appl. Cryst.*, **32**, p.373, 1999. 44
- [Kar05] F. Kargl. *The interplay of structure and microscopic dynamics in oxidic melts observed by means inelastic neutron scattering*. Dissertation, Physikdepartment E13, TU München, 2005. 20
- [KB87] U. Krieger and J. Bosse. In *Amorphous and Liquid Materials*, vol. 118 of NATO ASI E: *Applied Physics*, E. Lüscher, G. Fritsch, and G. Jacucci, editors. Nijhoff, Dordrecht, 1987. 40
- [KDS89] S.C. Kohn, R. Dupree, and M.E. Smith. *Nature*, **337**(9), p.539, 1989. 7
- [KDSW96] R. Knoche, D.B. Dingwell, F.A. Serfert, and S.L. Webb. *Chem. Geol.*, **116**, p.1–16, 1996. 4, 12
- [KM04] F. Kargl and A. Meyer. *Chem. Geol.*, **213**, p.165, 2004. 7
- [KMKS06] F. Kargl, A. Meyer, M.M. Koza, and H. Schober. *Phys. Rev. B*, **74**, p.014304, 2006. 4, 5, 79
- [KWHB03] A. Kahle, B. Winkler, B. Hennion, and P. Boutrouille. *Rev. Sci. Instr.*, **74**, p.3717, 2003. 91

- [Lov84] S.W. Lovesey. *Theory of neutron scattering from condensed matter, I+II*. Clarendon Press, Oxford, 1984. 24
- [LP90] C.P. Lindsey and G.D. Patterson. *J. Chem. Phys.*, **73**(7), p.3348, 1990. 35
- [MA80] J.W. Morgan and E. Anders. *Proc. Natl. Acad. Sci.*, **77**(3), p.6973–6977, 1980. 1
- [MBS99] A. Meyer, R. Busch, and H. Schober. *Phys. Rev. Lett.*, **83**(24), p.5027, 1999. 38
- [MC06a] A.J. Moreno and J. Colmenero. *J. Chem. Phys.*, **125**, p.164507, 2006. 81
- [MC06b] A.J. Moreno and J. Colmenero. *Phys. Rev. E*, **74**, p.021409, 2006. 81
- [McM94] P.F. McMillan. *Rev. Mineral.*, **30**(1), p.132–156, 1994. 8
- [MDGN03] A. Meyer, R.M. Dimeo, P.M. Gehring, and D.A. Neumann. *Rev. Sci. Instr.*, **74**(5), p.2759, 2003. 71
- [MHK⁺04] A. Meyer, J. Horbach, W. Kob, F. Kargl, and H. Schober. *Phys. Rev. Lett.*, **93**(2), p.027801, 2004. 5, 6
- [MPPC90] M. Maret, T. Pomme, A. Pasturel, and P. Chieux. *Phys. Rev. B*, **42**(3), p.1598, 1990. 30
- [MPSR93] P.F. McMillan, B.T. Poe, T.R. Stanton, and R.L. Remmele. *Phys. Chem. Mineral.*, **19**, p.454, 1993. 7
- [MSD02] A. Meyer, H. Schober, and D.B. Dingwell. *Europhys. Lett*, **59**(5), p.708, 2002. 4
- [MSS83] O.V. Mazurin, M.V. Streltsina, and T.P. Shvaiko-Shvaikovskaya. *Handbook of Glass, Part A: silica glass and binary silicate glasses*. Elsevier, 1983. 20
- [Mül03] A. Müller. *Struktur und Dynamik wasserhaltiger Silikatgläser untersucht mit Neutronenstreuung*. Diploma thesis, Physikdepartment E13, TU München, 2003. 17
- [MVC98] G. Moore, T. Vennemann, and I. S. E. Carmichael. *Am. Mineral*, **83**, p.36, 1998. 15
- [NB97] M. Nowak and H. Behrens. *Contrib. Mineral. Petrol.*, **126**(4), p.365, 1997. 90
- [Neu06] J. Neuhaus. Private communication, 2006. 46

- [PBK04] M. Pöhlmann, M. Benoit, and W. Kob. Phys. Rev. B, **70**(18), p.184209, 2004. 9
- [PMM⁺] M. Pöhlmann, A.R. Müller, A. Meyer, H. Schober, and T. Hansen. *Structural and dynamical properties of hydrous amorphous silicates as seen by neutron scattering*. Submitted to Phys. Rev. B. 8
- [Pöh05] M. Pöhlmann. *Structure and Dynamics of Hydrous silica(te) as seen by Molecular Dynamics Computer Simulations and Neutron Scattering*. Dissertation, Physikdepartment E13, TU München, 2005. 10, 31
- [PP62] H.H. Paalman and C.J. Pings. J. Appl. Phys., **33**(8), 1962. 66
- [RPM⁺01] C. Romano, B. Poe, V. Mincione, K.-U. Hess, and D.B. Dingwell. Chem. Geol., **174**(1-3), p.115, 2001. 21, 86
- [RRGF72] J.M. Rowe, J.J. Rush, L.A. de Graaf, and G.A. Ferguson. Phys. Rev. Lett., **29**(18), p.1250, 1972. 35
- [SB91] W. Schirmacher and B. Bunsenges. Phys. Chem., **95**, p.368, 1991. 36
- [SGS95] R.A. Sadykov, P.L. Gruzin, and V.A. Suhoparov. High Pressure Res., **14**, p.199, 1995. 44
- [SMD95] J.F. Stebbins, P.F. McMillan, and D.B. Dingwell, editors. *Structure, Dynamics and Properties of Silicate Melts*. Reviews in Mineralogy **32**. Mineral. Soc. of Am., Washington, 1995. 2
- [SPSH90] W. Schirmacher, M. Prem, J.-B. Suck, and A. Heidemann. Europhys. Lett., **13**(6), p.523, 1990. 36
- [Squ78] G.L. Squires. *Introduction to the theory of thermal neutron scattering*. Cambridge University Press, London, 1978. 24
- [Sto82] E. Stolper. Contrib. Mineral. Petrol., **81**, p.1–17, 1982. 7, 8
- [SVP⁺91] S. Susman, K.J. Volin, D.L. Price, M. Grimsditch, J.P. Rino, R.K. Kalia, P. Vashishta, G. Gwanmesia, Y. Wang, and R.C. Liebermann. Phys. Rev. B, **43**(1), p.1194, 1991. 30
- [TSW⁺98] A. Töller, H. Schober, J. Wuttke, O.G. Randl, and F. Fujara. Phys. Rev. Lett, **80**(11), p.2374, 1998. 38
- [TTA⁺83] M. Tomozawa, M. Takata, J. Acocella, E.B. Watson, and T. Takamori. J. Non-Cryst. Solids, **56**(1-3), p.343–348, 1983. 20

- [UMNP07] T. Unruh, A. Meyer, J. Neuhaus, and W. Petry. Neutron News, **18**(2), p.22–24, 2007. 59
- [UNP07] T. Unruh, J. Neuhaus, and W. Petry. *The high-resolution time-of-flight spectrometer TOFTOF*. Nucl. Instr. and Meth. A, **580**(3), p.1414, 2007. 59, 69
- [VH06] Th. Voigtmann and J. Horbach. Europhys. Lett., **74**(3), p.459, 2006. 81, 84
- [WK07] J. Wuttke and F. Kargl. <http://sourceforge.net/projects/frida/>, 2007. 64
- [Wut08] J. Wuttke. SPHERES online handbook, 2008. Jülich Center for Neutron Science. 71
- [Zha99] Y. Zhang. Rev. Geophys., **37**(4), p.493, 1999. 8, 14, 90
- [ZKHS96] N. Zotov, H. Keppler, A.C. Hannon, and A.K. Soper. J. Non-Cryst. Solid, **202**(1-2), p.153, 1996. 8
- [Zol92] I.V. Zolotuchin. *Physikalische Eigenschaften amorpher metallischer Werkstoffe*. Dt. Verl. für Grundstoffindustrie, Leipzig, 1992. 31
- [ZS91] Y. Zhang and E.M. Stolper. Nature, **305**, p.306, 1991. 90
- [ZSI95] Y. Zhang, E.M. Stolper, and P.D. Ihinger. Am. Mineral., **80**, p.593, 1995. 8
- [ZVEK92] N. Zotov, Y. Vanev, M. Epelbaum, and L. Konstantinov. J. Non-Cryst. Solid, **142**, p.234, 1992. 8

Declaration of authorship

Herewith I certify that I am the author of this thesis and that any assistance I received in its preparation is fully acknowledged and disclosed in the paper. I have also cited any sources from which I used data, ideas or words, either quoted directly or paraphrased.

Garching, January 29, 2009

Fan Yang